Copyright

by

Dipanjan Basu

2010

The Dissertation Committee for Dipanjan Basu Certifies that this is the approved version of the following dissertation:

Quantum Transport and Bulk Calculations for Graphene-Based Devices

Committee:

Leonard F. Register, Supervisor

Sanjay K. Banerjee, Co-Supervisor

Emanuel Tutuc

Allan H. MacDonald

Jack Lee

Swaroop Ganguly

Quantum Transport and Bulk Calculations for Graphene-Based Devices

by

Dipanjan Basu, B.E., M. Tech.

Dissertation

Presented to the Faculty of the Graduate School of
The University of Texas at Austin
in Partial Fulfillment
of the Requirements
for the Degree of

Doctor of Philosophy

The University of Texas at Austin
December, 2010

Dedication

To my parents

Acknowledgements

It gives me immense pleasure to express my heartfelt gratitude to my advisors Dr. Leonard Franklin Register and Dr. Sanjay K. Banerjee. Their able guidance, encouraging words, and constant support in all forms have always been directed to the best of my interest. They are so responsive, patient and understanding— I find it difficult to express in words their contribution, this work would not be possible without them.

My sincere thanks to Dr. Allan H. MacDonald, whose help, especially to this work, especially the final parts has been invaluable. He has been very kind to my queries, giving me time whenever I wanted. I am grateful to Dr. Emanuel Tutuc, Dr.Swaroop Ganguly and Dr. Jack Lee for serving in my committee, and thank them sincerely. I also want to thank Dr. Chandra Mouli for the opportunity of the interesting research internship with Micron Technologies, Inc. at Boise in summer 2008.

I have been helped in my work by many colleagues and friends whose contribution I greatly appreciate, Dr. Matthew Gilbert with whom I collaborated in the initial years, and my group mates over the years; Swaroop, Xiaofeng, Xin, Bahniman, Ken-Ming, Mehedi, Hui, John, Ningyu and Dharmendar. Special thanks to Dharmendar for his help with understanding the mean-field theory and related work.

I am deeply indebted to my dear parents, whose encouragement and support have nourished me and have made me who I am, and to my darling wife Antara whose presence here has in so many ways improved my experience outside work. I have many happy memories with friends here at Austin, I thank them, especially to Sagnik, Shovan, Swaroop, Samaresh, Debarshi, Samarjit, Praveen and their families. Special thanks to my friends Dipankar and Mosin. Thanks to Jeannie for support, to Joe, Joy, Jason and Emmanuel for their company. Finally I thank the Almighty for everything.

Quantum Transport and Bulk Calculations for Graphene-based Devices

Publication No._____________

Dipanjan Basu, Ph.D.
The University of Texas at Austin, 2010

Supervisor: Leonard F. Register
Co-supervisor: Sanjay K. Banerjee

As devise sizes approach the nanoscale, novel device geometries and materials are considered, and new types of essential physics becomes important and new physical switching mechanism are considered, and as our intuitive understanding of device behavior is stretched accordingly, increasing first-principles simulation is required to understand and predict device behavior.

To this end, initially I worked to capture the richness of the confinement and transport physics in quantum-wire devices. I developed an efficient fully three dimensional atomistic quantum transport simulator within a nearest-neighbor atomistic tight-binding framework.

However, I soon adapted this work to the study of transport in graphene monolayer and bilayer nano-ribbons. Motivated by proposals for use of nano-ribbons to create band gaps in otherwise gapless graphene monolayers, I studied the effects of edge disorder in such graphene nano-ribbon FETs. I found that ribbon widths sufficiently

narrow to produce useful bandgaps, would also lead to an extreme sensitivity to ribbon-edge roughness and associated performance degradation and device-to-device variability.

Going beyond conventional switching but staying with the graphene material system, to model electron-hole condensation in two graphene monolayers separated by a tunnel dielectric potentially beyond room temperature, I developed a self-consistent atomistic tight-binding treatment of the required interlayer exchange interaction within non-local Hartree-Fock mean-field theory. Such condensation, associated many-body enhanced interlayer current flow, and gate-control thereof is the basis for the beyond-CMOS Bilayer-pseudoSpin Field Effect Transistor (BiSFET) proposed by colleagues. I studied the effect of various system parameters and on interlayer charge imbalance on the strength of the condensate state. I also modeled the critical current, the maximum interlayer current that can be supported by the condensate, its detailed dependence on the nature and strength of the required interlayer bare tunneling and on charge imbalance. The results presented here are expected to be used to refine devices models of the BiSFET, and may serve as guides to experiments to observe such a condensate state.

Table of Contents

List of Figures x

Chapter 1: Introduction 1

1.1 Background for the dissertation 1

1.2 Outline 3

Chapter 2: Atomistic full-band quantum simulator 4

2.1 Necessity of 3D, full band, atomistic quantum simulators 4

2.2 Numerical method 5

2.3 Results of band-to-band tunneling in III-V nanowire FETs 12

2.4 Applications to other devices 15

2.5 Conclusion 16

Chapter 3: Effect of edge roughness in graphene nanoribbons channel MOSFETs17

3.1 Background for studying the effect of edge roughness 17

3.2 Modeling edge roughness 20

3.3 Results 21

3.4 Applications of the Program to Other Graphene-based Devices 24

3.5 Conclusion 27

Chapter 4: Tight-binding study of spontaneous electron-hole condensation in graphene bilayers 29

4.1 Motivation for the present work 29

4.2 Modeling interlayer exchange interactions in graphene bilayers using tight-binding π-orbital basis 32

4.3 Results of spontaneous exchange interactions in graphene bilayers ...37

4.4 Conclusion 53

Chapter 5: Effect of interlayer bare tunneling on electron-hole coherence in graphene bilayers 54

5.1 Interlayer bare tunneling as a tight-binding parameter 54

5.2 Self-consistent results and Discussion 55

5.3 Conclusion 65

Chapter 6: Conclusion....70
    6.1 Summary....70
    6.2 Future Work....74

References....77

Vita....83

List of Figures

Figure 3.1. Eight fcc lattice planes, stacked along (100) direction, to form a square nanowire 2 atoms wide, showing the individual atomic locations in the plane. For zinc blende structures such as InSb, the layers are alternately anions and cations. For a diamond crystal structure such as Si or Ge, all the atoms are identical. 8

Figure 3.2. Schematic of the transport calculation showing the break-up of the simulation region into a device region that includes source, channel and drain regions (green shade), and semi-infinite source and drain contacts at the two ends. The layer to layer interaction matrix is shown for only one interaction in the schematic (H_{12}). In practice, there are a large number of slices in the device region, depending on the length of the device simulated...9

Figure 3.3. Schematic of the device simulated: (left) the cross-section of the channel region, perpendicular to the transport direction and (right) the view from the top showing the source and drain contact at the ends, and the gate oxide in the middle, surrounding the channel. 11

Figure 3.4. Energy dispersion relationship of the multiple quantum confined subbands of a square (100) InSb nanowire of width 26.92 Å.....13

Figure 3.5. I_D-V_G for two square (100) InSb nanowire MOSFETs in a gate-all-around architecture, having identical channel length of L_{ch} = 5.2 nm. Inset: I_D-V_G in linear scale. Lower BTBT in narrow nanowires reduces I_{OFF}, but peak I_D is also slightly reduced for narrow nanowires. 14

Figure 3.6. I_D-V_G for two square (100) InSb nanowire MOSFETs, having same W_{ch} = 3.24 nm, and different L_{ch}. Longer L_{ch} has lower minimum I_{OFF} due to reduced BTBT. In absence of scattering, peak I_D is unchanged with L_{ch}, as the inset (linear plot of I_D-V_G) confirms. 15

Figure 3.7. Transmission as a function of injection energy in InSb for a barrier of height 1.1 eV when injected from InSb nanowire, as a function of the barrier length (top-down increases by one monolayer, starting from 1. W_{ch} = 3.24 nm. The symbols are from the full band simulator, and solid line from Franz two band model, with effective mass adjusted to fit the full band result. 16

Figure 3.1. Armchair (horizontal ribbon) and zigzag (vertical ribbon) nanoribbon edge configurations and associated primitive unit cells along the ribbon. The green rhombus shows the primitive cell for bulk monolayer graphene containing one each of A and B sublattice C atoms (white and blue circles). 18

Figure 3.2. First three dispersion relations from left to right: conduction band subbands for graphene nanoribbons having armchair edges of 1.6, 1.8 and 2.0 nm widths, or 7, 8 and 9 atoms along a line. Extreme right dispersion relation: zigzag nanoribbon of 1.14 nm width corresponding to 7 atoms along a line. Energy is reference to the nominal Dirac point energy. All zigzag nanoribbons, and armchair nanoribbons having $3p+1$ atomic width, where p is an integer, have states at $E = 0$. a is the C-C bond length (1.42 Å). 19

Figure 3.3. Left: (a) Top view of an armchair graphene nanoribbon channel, showing vacant sites along the edges where C atoms (black dots) are missing. Right: (b) Schematic of the double gate MOSFET simulated (side view). For clarity, the nanoribbon of (a) is shorter (10.5 nm) than that used in the simulated MOSFET. 21

Figure 3.4. Left: (a). Transmission $T(E)$ as a function of incident energy E across graphene channels having identically rough edges. Right (b) $T(E)$ vs. E for a 7.63 nm wide graphene channel having different roughness at the edges. r = 0.5 has edge sites randomly vacant and r=1.0 has a perfect armchair edge. Steps show perfect transmission for ideal armchair edges of corresponding width. 22

Figure 3.5. I_D–V_G characteristics on Left (a) log-linear and Right (b) linear-linear scale for the MOSFET structure of Fig. 1, for three different channel widths, showing performance degradation for channels with rough edges (dashed lines, solid symbols) from the ideal ballistic devices (solid lines, open symbols). V_D = 0.2 V...23

Figure 3.6. Left (a) I_D–V_G in linear scale for the dual gate MOSFET with W_{ch} = 4.18 nm and L_{ch} = 16.75 nm, using different values of edge roughness parameter r. Right (b) I_D–V_G for W_{ch} = 4.67 nm, for two different L_{ch}, using same r (=0.9). For both figures, error bars plotted indicate standard deviation in I_D across ten randomly different edges having macroscopically same values of r. V_D = 0.3 V for these simulations. 24

Figure 3.7. I_D-V_D characteristics for single layer armchair graphene nanoribbon having 42.46 nm device length, L_{ch} = 16.76 nm, T_{ox} = 2.5 nm, N_{DS} = 5×10^{12} cm^{-2} and V_G = -0.1 V The tunneling current and over the top current are visual aids to understand the components that make up the total I_D. 26

Figure 3.8. Resonant interlayer tunneling current (I_{il}) for a graphene bilayer as a function of the interlayer potential (V_{il}) that serves to align the bands at V_{il} =0, or destroy the resonance at $V_{il} \neq 0$, for three different channel lengths L_{ch} = 31.48 nm. Left (a) I_{il} normalized to the channel width (20 nm for all the three curves), and on right (b) normalized to maximum I_{il} 27

Figure 4.1. Top (a) Device schematic of BiSFET showing uncoupled graphene contacts, and coupled channel. Δ creates asymmetry between the top (hole) and bottom (electron) layers. Direction of wave function propagation and corresponding electrical currents are also shown. Bottom (b) I-V characteristics of BiSFET for three different gate voltages $V_{G,n}$ with $V_{G,p}$ = -25 mV consistent with Eqn. (4.1) and (4.2) and 20 nm gate width. Note that while the region of condensate formation is indicated schematically in (a) by reduced spacing between layers here, there are others ways to localize the condensate including changes in dielectrics, charge densities, and/or initial degree of charge balance. 32

Figure 4.2. Left (a) Schematic of the two oppositely charged graphene monolayers, separated by a dielectric. Right (b) Arrangement of C atoms showing the primitive cell (green rhombus) containing four atoms — A_T (dotted circle) and B_T (blue circle) for the top layer C atoms, and A_B (red solid circle) and B_B (blue solid circle) for the bottom layer. This figure is for the Bernal stacking arrangement in which B_T lies directly above A_B. Also shown are the real space lattice vectors $\vec{a}_1$ and $\vec{a}_2$, and the vectors from A_T to the nearest neighbor B_T atoms, $\vec{n}_1$, $\vec{n}_2$ and $\vec{n}_3$ 33

Figure 4.3. Energy bands of two graphene layers separated by 1.0 nm of SiO_2 (ε_r = 3.9), having layer potentials of $-\Delta/2$ (top layer – blue) and $+\Delta/2$ (bottom layer – red) in the uncoupled state (solid lines) along the high symmetry directions in the Brillouin zone (shown above). $\Delta = 0.5$ eV. Phase coherence between layers creates a correlated, lower energy state (black dash-dotted lines). The inset magnifies the low energy spectrum, revealing a band gap E_g of 74 meV at 0 K for balanced top and bottom layer charge distributions, i.e., E_F is located within the band gap in this case..37

Figure 4.4. Left (a) The real-space variation of the exchange potential $V_{HF}(R_T,R_B)$ for coupling between atoms of the A sublattices of top and bottom layers, as a function of $R_B - R_T$. $\Delta = 0.5$ eV, $d = 1$ nm, $\varepsilon_r = 3.9$, and balanced charge distributions at 0 K are assumed. Here and subsequent such plots, the color of the marker spheres indicate the value of the interaction, and the sizes of the spheres indicate the magnitude of this value. Right (b) Top view of the potential showing rapidly oscillating nature of $V_{HF}(R_T,R_B)$ 40

Figure 4.5. $V'_{HF}(R_T,R_B)$ for (left) A_T-A_B coupling and (right) B_T-B_B coupling, obtained by dividing $V_{HF}(R_T,R_B)$ by $\exp[i\mathbf{k}_D \cdot (\mathbf{R}_B - \mathbf{R}_B)]$, as a function of $R_B - R_T$. The imaginary components vanish. $\Delta = 0.5$ eV, $d = 1$ nm, $\varepsilon_r = 3.9$, and balanced charge distributions at 0 K are assumed. 41

Figure 4.6. (Left) Real and (right) imaginary parts of $V'_{HF}(R_T,R_B)$ for A_T-B_B coupling as a function of $R_B - R_T$. $\Delta = 0.5$ eV, $d = 1$ nm, $\varepsilon_r = 3.9$, and balanced charge distributions at 0 K are assumed. 41

Figure 4.7. (Left) (Left) Real and (right) imaginary parts of $V'_{HF}(R_T,R_B)$ for B_T-A_B coupling as a function of $R_B - R_T$. $\Delta = 0.5$ eV, $d = 1$ nm, $\varepsilon_r = 3.9$ and balanced charge distributions at 0 K are assumed. 42

Figure 4.8. Band gap as a function of potential difference Δ for three different dielectrics, with $d = 1$ nm and balanced charge distributions at 0 K. 43

Figure 4.9. Left (a). Low-energy dispersion of the graphene bilayer system with $\Delta = 0.5$ eV and $\varepsilon_r = 2.2$ at 0 K, and balanced charge distributions, as a function of layer separation d (legend entries are in nm). The labeled solid lines (black and red online, respectively) are the band structures of the top and bottom graphene layers in absence of an exchange coupling between the layers. Right (b) Band gap E_g in the correlated condensate state for three different dielectrics, showing exponential scaling of the band gap with layer separation, at 0 K with $\Delta = 0.5$ eV and balanced charge distributions. 44

Figure 4.10. Band gap for two graphene layers with $\Delta = 0.5$ eV, $d = 1$ nm, and balanced charged distributions at 0 K and 300 K, as a function of the dielectric constant. The minimum values are limited by the accuracy of the calculation. 44

Figure 4.11. Band gap E_g for the bilayer condensate with $\Delta = 0.5$ eV and balanced charged distributions at 0 K, as a function of the interlayer dielectric constant ε_r and layer separation d. 45

Figure 4.12. Temperature dependence of the band gap for three different dielectric constants with $\Delta = 0.5$ eV, $d = 1$ nm and balanced charge distributions. Lower ε_r result in larger coupling strength and therefore larger 0 K band gaps that are, therefore, also more robust at higher temperatures. The top right insert shows the same data scaled by 0 K band gap (E_{g0}), to illustrate the similarity of the T dependence of band gap for different ε_r. 46

Figure 4.13. Energy band edges and Fermi level as a function of carrier imbalance between top layer electron density and bottom layer hole density for graphene bilayers separated by 1 nm at 25 K and 300 K with $\varepsilon_r = 3$ and $\Delta = 0.5$ eV. 48

Figure 4.14. Energy band edges and Fermi level as a function of carrier imbalance between top layer electron density and bottom layer hole density for graphene bilayers separated by 1.3 nm at 25 K and 300 K with $\varepsilon_r = 3$ and $\Delta = 0.5$ eV. 49

Figure 4.15. Expectation value of the interlayer tunneling $<V_{bare}>$ expressed in terms of the assumed bare interlayer tunneling $t_\perp$, as a function of the interlayer phase difference ω (left axis, blue solid curve). Right axis (green dotted curve) shows the critical current. Both results are for interlayer bare tunneling between only A_T and A_B carbon atoms. $<V_{bare}>$ as well as the critical current approaches zero for Bernal-like or hexagonal-like perturbative coupling 52

Figure 5.1. Surface plots showing on left the band gap (in meV) and on right the critical current density (I_c) variation for a graphene bilayer with weak coupling between A_T-A_B and B_T-B_B carbon atoms. For a given magnitude of bare tunneling, the maximum band gap (and I_c) occur when $t_{\perp BB} = -t_{\perp AA}$, since that is the phase relationship established between the graphene sublattices to maximize the exchange interaction in the limit of the "spontaneous condensate" ($t_{\perp BB} =-t_{\perp AA} =0$). .57

Figure 5.2. Self consistent band gap vs bare tunneling (both in meV) for two different cases of bare tunneling (A_T-A_B only and B_T-A_B only). Band gap for single particle bare tunneling only is shown in pink, scaled by the spontaneously formed (no tunneling) coherent state band gap, E_{g0} for comparison. $\Delta = 0.5$ eV, $d = 1$ nm, $\varepsilon_r = 3.0$, and balanced charge distributions at 0 K are assumed. 60

Figure 5.3. Critical current as a function of bare tunneling for A_T-A_B and B_T-A_B coupling. The dependence becomes identical for large $t_\perp$ (inset). $\Delta = 0.5$ eV, $d = 1$ nm, $\varepsilon_r = 3.0$, and balanced charge distributions at 0 K are assumed. 60

Figure 5.4. Self-consistent Fock exchange potentials $V'_{HF}(R_T,R_B)$ for graphene bilayers with a $t_\perp$bare tunneling between C atoms in Bernal (B_T-A_B) stacking for three different sublattice pair interactions, as a function of $R_B - R_T$. $\Delta = 0.5$ eV, $d = 1$ nm, $\varepsilon_r = 3.0$, and balanced charge distributions at 0 K are assumed. 61

Figure 5.5. Critical current supported by the excitonic condensate scaled by the bare hopping potential strength $t_\perp$ as a function of $t_\perp$ for the hexagonal-like (A_T-A_B only) and bernal (B_T-A_B only) bare tunneling. For perturbative calculation, the critical current is directly proportional to $t_\perp$ for A_T-A_B tunneling, and is zero for B_T-A_B tunneling 62

Figure 5.6. Temperature dependence of the band gap for three different bare tunneling values, zero, 1.0 meV and 2.5 meV, all having A_T-A_B tunneling only. $\varepsilon_r = 3.0$ with $\Delta = 0.5$ eV, $d = 1$ nm and balanced charge distributions. Top right insert shows the same data scaled by 0 K band gap (E_{g0}). 63

Figure 5.7. Temperature dependence of the band gap for three different bare tunneling values, zero, 1.0 meV and 2.5 meV, all having B_T-A_B tunneling only. $\varepsilon_r = 3.0$ with $\Delta = 0.5$ eV, $d = 1$ nm and balanced charge distributions. Top right insert shows the same data scaled by 0 K band gap (E_{g0}). 63

Figure 5.8. Self-consistent band gap as a function of imbalance for several different bare tunneling values for A_T-A_B coupling at T= 25 K (left) and 300 K (right). $\Delta = 0.5$ eV, $d = 1$ nm and $\varepsilon_r = 3.0$. The strength of the bare tunneling in meV is shown on the right. For comparison, the spontaneous condensate behavior ($t_\perp = 0$) is also shown............66

Figure 5.9. Self-consistently calculated critical current for graphene bilayers having an A_T-A_B bare coupling as a function of carrier imbalance between the layers for increasing values of bare tunneling, at T= 25 K (left) and 300 K (right). The current density is shown in linear scale in the bottom row and in logarithmic scale in the top row. $\Delta = 0.5$ eV, $d = 1$ nm, $\varepsilon_r = 3.0$. 67

Figure 5.10. Self-consistent band gap as a function of imbalance for several different bare tunneling values for B_T-A_B coupling at T= 25 K (left) and 300 K (right). $\Delta = 0.5$ eV, $d = 1$ nm and $\varepsilon_r = 3.0$. The strength of the bare tunneling in meV is shown on the right. For comparison, the spontaneous condensate behavior ($t_\perp = 0$) is also shown. The arrows in the left figure (T=25 K) denote the cases, for which the exchange potentials have been drawn in Fig. 5.13 to explore the reason behind the variation obtained here...67

Figure 5.11. Self-consistently calculated critical current for graphene bilayers having a B_T-A_B bare coupling as a function of carrier imbalance between the layers for increasing values of bare tunneling, at T= 25 K (left) and 300 K (right). The current density is shown in logarithmic scale in the top row and in linear scale in the bottom row. $\Delta = 0.5$ eV, $d = 1$ nm, $\varepsilon_r = 3.0$. 68

Figure 5.12. Self-consistent band gap as a function of imbalance for several different bare tunneling values for A_T-A_B coupling at T= 25 K (left) and 300 K (right). $\Delta = 0.5$ eV, $d = 1$ nm and $\varepsilon_r = 3.0$. The strength of the bare tunneling in meV is shown on the right. For comparison, the spontaneous condensate behavior ($t_\perp$=0) is also shown.............68

Figure 5.13. Self-consistent Fock exchange potentials $V'_{HF}(R_T,R_B)$ for graphene bilayers showing the loss of symmetry due to carrier imbalance. $\Delta = 0.5$ eV, $d = 1$ nm, $\varepsilon_r = 3.0$, and T= 25 K for these simulations..........69

Chapter 1: Introduction

1.1 BACKGROUND FOR THE DISSERTATION

As devise sizes approach the nanoscale, novel device geometries and materials are considered, and new types of essential physics becomes important and new physical switching mechanism are considered, and as our intuitive understanding of device behavior is stretched accordingly, increasing first-principles simulation is required to understand and predict device behavior.

Scaling of the Complementary Metal-Oxide Semiconductor (CMOS) logic technology into and beyond the 16 nm node is a difficult challenge that lies ahead in the semiconductor technology roadmap [1] Owing in part to these CMOS scaling issues, there is an increased emphasis on emerging materials and devices that may provide a solution beyond the 22nm node. In the short run, alternate channel materials such as Germanium, III-V compound semiconductors and graphene can be substituted in place of bulk and strained Si to achieve performance gains, provided the replacement channel material is able to overcome the technological problems of fabricating high-quality, defect-free channel matched to underlying Si substrate. These state-of-the-art metal-oxide-semiconductor field-effect transistors (MOSFETs) have common traits—use of novel materials (e.g., strained materials, III-Vs,), strong geometrical confinement (e.g., strong gate fields, silicon on insulator devices, FinFETs, nanowire devices) and current paths comparable to or less to their mean-free path between scattering events. This scaling invalidates treatment of the carriers as localized particles, and drift-diffusion or even hydrodynamic models of transport. Semiclassical Monte Carlo methods can frequently be used to address the transport issues, and even the quantum confinement issues within useful approximations via quantum corrected potentials [2-7]. For more rigorous simulation fully quantum methods are required in principle. In practice, however, increased rigor leads to increased computational demand and the search for computational efficiency and rigor continues. To date a variety of methods have been pursued including methods that seek solution analytically [2-4] or numerically [5-10] in one or more dimensions using Green's function approaches [5-11].

Recently, there has been tremendous enthusiasm in the semiconductor community since the isolation of single layers of graphite or graphene by Novoselov and Geim in 2004 [12]. Single and few layers of carbon sheets (graphene) and ensuing field effect devices have been demonstrated. Much like carbon nanotubes, graphene layers exhibit very high room temperature mobilities, up to μ=10,000 cm^2/Vs, corresponding to a long, ~400nm mean free path and Fermi velocity of 1/300 the speed of light (10^8 cm/s) which ise ten times that in Si, and can 'in principle' lead to very high ON-state Field-Effect-Transistor (FET) currents [13]. But since graphene is a gapless semiconductor, it also leads to high OFF-state leakage and non-saturating drive currents which are problematic for digital logic, as will be discussed in more detail later.

The ITRS also identifies that, in the long run, there is a need for the development of a new manufacturable information processing primitive that may augment the CMOS logic gate by being able to perform specific tasks more efficiently as a primitive unit, or even ultimately replacing CMOS. Graphene, also has a unique linear band structure, unlike the parabolic $E(\mathbf{k})$ relation in most semiconductors, leading to what are known as Dirac massless fermions. And it seems possible that some of the remarkable physics of graphene will lead to novel beyond-CMOS logic devices as well, such as gated tunneling-devices [citation needed] or the recently proposed "pseudospin" devices [14], which operates on entirely different switching materials.

1.2 OUTLINE

The outline of this dissertation is as follows: In Chapter 2, I will delineate the development of our atomistic full-band simulator and apply it to demonstrate band-to-band tunneling in nanowire MOSFETs with low-band gap III-V semiconductor channels. In Chapter 3, I move on to graphene-based devices and illustrate the difficulty in using extremely narrow width nanoribbons of graphene, a proposed means of achieving significant band gaps, as channel material for MOSFETs due to an extreme sensitivity of transport to edge roughness. In Chapter 4, I briefly review a novel device proposal based on possible room-temperature electron hole condensation in graphene bilayers. I then present our tight-binding calculations of the spontaneous (i.e., without single-particle tunneling) exchange interaction in such a system and investigate the role of various parameters on the excitonic condensation. In Chapter 5, I present self-consistent exchange interactions in the graphene bilayer in the presence of weak bare interlayer tunneling, and explore the dependency of the condensate state and exchange potential on the nature and strength of the bare tunneling. We also present the critical interlayer tunneling current between the graphene bilayers, the maximum interlayer current that the condensate can support, in presence of this bare tunneling and its dependence on various system parameters. Finally, in Chapter 6 I propose future directions to work on and provide concluding remarks.

Chapter 2: Atomistic full-band quantum simulator

2.1 NECESSITY OF 3D, FULL BAND, ATOMISTIC QUANTUM SIMULATORS

Phase coherent ballistic transport effects become important for many semiconductor devices as channel lengths scale to few tens of nm [15], necessitating full quantum transport simulation. FETs using nanowires as the semiconducting channel have high confinement in the channel region in not only the vertical, but also the lateral direction. Furthermore, the source (S) and drain (D) regions may be comparatively large compared to channel cross-section and defects such as surface roughness or charge impurities may be present within the channel. As a result, nominally discrete propagating modes can mix and a quasi one-dimensional (1D) model of quantum transport with discrete transverse modes within the channel cross-section can be insufficient. Fully three-dimensional (3D) quantum transport simulation becomes necessary.

Moreover, in present nanoscale devices, the energy bands are significantly altered from their bulk values, particularly for hole transport and very strongly confined electron systems, so that instead of the simpler and computationally easier effective mass approach, a full band structure treatment within a full quantum framework becomes a necessary refinement. Several III-V materials such as InAs, InSb, InGaAs and group IV material like Ge have been identified as possible candidates for replacing Si channel [1]. InSb with its very high electron mobility is particularly suitable for high-speed logic [16, 17]. The attendant low band-gap, however, makes it difficult to shut off the InSb based transistors, necessitating more complex architectures like quantum well FETs [18, 19]. Simple effective-mass based quantum transport simulation also fail to address the band-to-band tunneling in InSb nanowire transistors under high OFF-state gate bias, as well as the proper dependence of the band gap on the degree of confinement.

For simulation of transport in these novel materials, a full band, full quantum mechanical transport model is often required, to probe the properties of the device/material for different atomic configurations or atomic-level disorders. The recursive scattering matrix variant of the non-equilibrium Green's function (NEGF) based quantum transport simulator that we developed uses an atomistic, tight-binding basis, where it becomes relatively easy to simulate *ab initio* not only different materials, but also look at the effect of atomic scale disorders, such as effect of non-ideal edges in armchair graphene nanoribbon channel MOSFETs. Here, we will briefly sketch the development of this simulator, and use it to demonstrate how band-to-band tunneling increases the leakage current in OFF state in field-effect transistors with low band gap semiconductors such as InSb as channel material.

2.2 NUMERICAL METHOD

Here we have adapted an efficient transmission matrix based approach to quantum transport calculation previously implemented within an effective mass approximation [20] for full 3D, atomistic, nearest-neighbor tight-binding (TB) based simulations. These transport calculations represent an alternative numerical implementation for such systems of the widely accepted non-equilibrium Green's function [NEGF] approach [21].

2.2.1 Crystal structure and basis set

We incorporate each atom in the device explicitly in the Hamiltonian, and represent each atom by its orthogonal (Löwdin) orbitals, where the on-site energies and hopping potentials are obtained from empirical TB theory [22]. The atomistic Hamiltonian changes for different materials, orbital bases and crystal orientations; however, the general method remains the same. For an optimum balance of accuracy and computational cost in the simulations of this work, we have restricted ourselves to the sp^3s^* basis with nearest neighbor interactions, as the energy bands are well modeled close to the Γ point [22]. Also, we have used the original empirical TB parameters given in [22] instead of the parameters optimized to obtain best fit of just the low lying conduction and valence bands [23]. Here we demonstrate the capability of our atomistic simulator in a qualitative rather than quantitative fashion, and therefore we will restrict our concentration to [100] transport in III-V semiconductors that exhibit a zinc-blende crystal structure.

For [100] transport in a square III-V nanowire, we can visualize the nanowire as successive face-centered cubic (fcc) planes that are displaced from the previous plane along the body diagonal by ($a/4$, $\pm a/4$, $\pm a/4$) where a is the material lattice constant. The atomistic view of eight successive fcc planes along the transport direction is shown in Fig. 1. The atomic structure repeats itself every fourth layer along the transport direction, and therefore, these four layers constitute the primitive cell.

2.2.2 Band structure calculation for the leads

The time-independent Schrödinger equation for a tight-binding Hamiltonian can be written in a layer-to-layer coupled form as:

$$\mathbf{H}_{l,l-1}\boldsymbol{\psi}_{l-1} + \mathbf{H}_{l,l}\boldsymbol{\psi}_{l} + \mathbf{H}_{l,l+1}\boldsymbol{\psi}_{l+1} = E\boldsymbol{\psi}_{l} \tag{2.1}$$

Here $\boldsymbol{\psi}_l$ is the wavefunction (column matrix) where each row corresponds to a particular orbital of a particular atom in the l-th layer, $\mathbf{H}_{l,l\pm1}$ is the coupling (square matrix) from layer l to layer $l\pm1$, E is the eigenenergy and the $\mathbf{H}_{l,l}$ are populated with on-site energies including applied potential energy contributions, and transfer matrix elements between atoms in same layer, and $\mathbf{H}_{l,l\pm1}$ are populated with transfer matrix elements between atoms in neighboring layers. The entire device from source (S) to drain (D) can be broken up into N layers perpendicular to the transport direction. Fig. 2 shows these layers schematically. Within the leads the applied potential energy contributions are determined by the source and drain biases and the injected charge densities; within the simulation region, by self-consistent electrostatics.

The S/D contacts/leads can be assumed to be semi-infinite wires that are in thermal equilibrium with the applied bias, and are therefore equipotential. Denoting the four layers of the fcc lattice repeat unit from left to right as –2 to 1 (see Fig. 3.2) and assuming constant potential, which is adjusted consistent with source and drain biases and charge densities, (1) can be written explicitly for the left lead as:

$$\begin{matrix} \mathbf{H}_{-4,-3}\boldsymbol{\psi}_{-3} + \ \mathbf{H}_{-2,-2} - E \ \ \boldsymbol{\psi}_{-2} + \mathbf{H}_{-2,-1}\boldsymbol{\psi}_{-1} = 0 \\ \mathbf{H}_{-3,-2}\boldsymbol{\psi}_{-2} + \ \mathbf{H}_{-1,-1} - E \ \ \boldsymbol{\psi}_{-1} + \mathbf{H}_{-1,0}\boldsymbol{\psi}_{0} = 0 \\ \mathbf{H}_{-2,-1}\boldsymbol{\psi}_{-1} + \ \mathbf{H}_{0,0} - E \ \ \boldsymbol{\psi}_{0} + \mathbf{H}_{0,1}\boldsymbol{\psi}_{1} = 0 \\ \mathbf{H}_{-1,0}\boldsymbol{\psi}_{0} + \ \mathbf{H}_{1,1} - E \ \ \boldsymbol{\psi}_{1} + \mathbf{H}_{1,2}\boldsymbol{\psi}_{2} = 0 \end{matrix} . \qquad 2.2$$

where for Bloch states and also evanescent states within the leads we may write $\lambda\boldsymbol{\psi}_{-3} = \boldsymbol{\psi}_1, \boldsymbol{\psi}_2 = \lambda\boldsymbol{\psi}_{-2}$, with Bloch factor $\lambda = \exp \ \mp ik_x a$ for the set of four layers each space by a/4 from the previous.

After some algebraic manipulation we can reduce the eigensystem to a basis set consisting of $\boldsymbol{\psi}_2$ and $\boldsymbol{\psi}_3$ as follows:

$$\begin{bmatrix} -\mathbf{H}_{0,1}^{-1}\mathbf{H}_{0,-1} & -\mathbf{H}_{0,1}^{-1} \ \mathbf{H}_{0,0} - E \\ -\mathbf{H}_{1,2}^{-1} \ \mathbf{H}_{1,1} - E \ \mathbf{H}_{0,1}^{-1}\mathbf{H}_{0,-1} & \mathbf{H}_{1,2}^{-1}\mathbf{H}_{1,0} - \mathbf{H}_{1,2}^{-1} \ \mathbf{H}_{1,1} - E \ \mathbf{H}_{0,1}^{-1} \ \mathbf{H}_{0,0} - E \end{bmatrix} \begin{pmatrix} \boldsymbol{\psi}_{-1} \\ \boldsymbol{\psi}_{0} \end{pmatrix} =$$

$$\lambda \left[\begin{matrix} \mathbf{H}_{-2,-3}^{-1} \ \mathbf{H}_{-2,-2} - E \ \mathbf{H}_{-1,-2}^{-1} \ \mathbf{H}_{-1,-1} - E \ - \mathbf{H}_{-2,-3}^{-1}\mathbf{H}_{-2,-1} & \mathbf{H}_{-2,-3}^{-1} \ \mathbf{H}_{-2,-2} - E \ \mathbf{H}_{-1,-2}^{-1}\mathbf{H}_{-1,0} \\ -\mathbf{H}_{-1,-2}^{-1} \ \mathbf{H}_{-1,-1} - E & \mathbf{H}_{-1,-2}^{-1}\mathbf{H}_{-1,0} \end{matrix} \right. \qquad 2.3$$

Equation (2.3) is a generalized eigenvalue system whose dimension depends on the size of the system modeled and the tight-binding basis set used. We solve Eqn. (2.3) using standard commercially available math libraries such as IMSL [24].

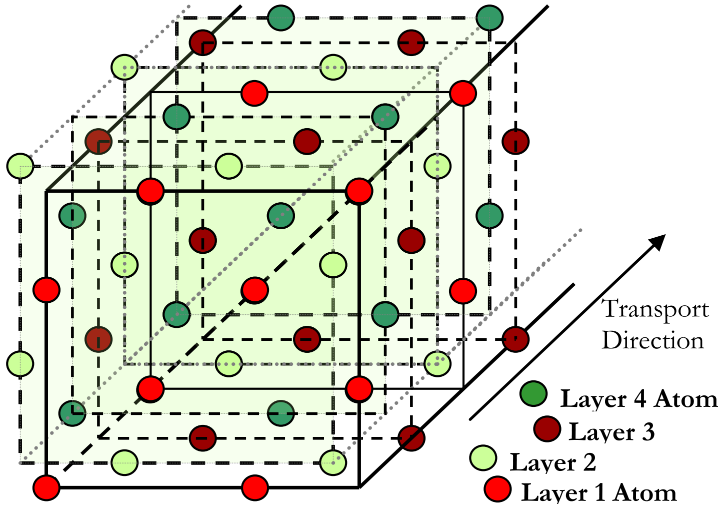

Figure 2.1. Eight fcc lattice planes, stacked along (100) direction, to form a square nanowire 2 atoms wide, showing the individual atomic locations in the plane. For zinc blende structures such as InSb, the layers are alternately anions and cations. For a diamond crystal structure such as Si or Ge, all the atoms are identical.

The eigenfunctions of Eqn. (2.3) can be identified as propagating modes if $|\lambda|=1$. A plot of the corresponding real values of k_x vs. the eigenenergy E provides the real band structure for the quantum wire leads. A similar procedure also allows calculation of the imaginary band structure for the evanescent states $|\lambda|\neq 1$ which is relevant to understanding tunneling.

The probability current flow j for any wavefunction $\boldsymbol{\psi}_l$ is:

$$j = \frac{2}{\hbar}\mathrm{Im}\left[\boldsymbol{\psi}_l^{\dagger}\mathbf{H}_{l,l+1}\boldsymbol{\psi}_{l+1}\right]. \qquad 2.4$$

The probability current carried per mode per unit energy by these occupied Bloch states should always be precisely equal to $2/h$ counting both spin states, where h is the Planck's constant. This relation is used to normalize the amplitude of the incident wavefunctions. The solutions to Eqn. (2.3) with $|\lambda|=1$ and $j>0$ (although not necessarily $k_x>0$) for the left lead represent the right-going incident propagating waves.

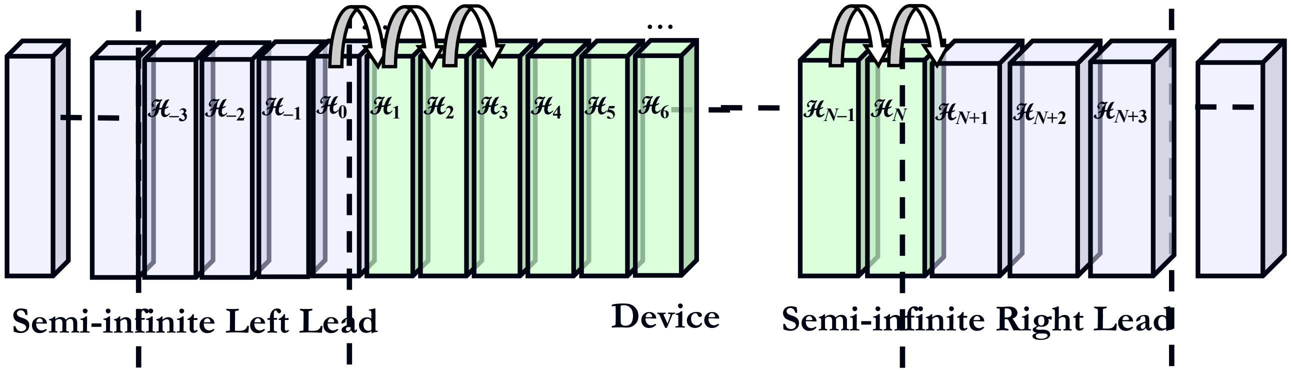
$\mathcal{H}_{-3}$
$\mathcal{H}_{-2}$
$\mathcal{H}_{-1}$
$\mathcal{H}_{0}$
$\mathcal{H}_{1}$
$\mathcal{H}_{2}$
$\mathcal{H}_{3}$
$\mathcal{H}_{4}$
$\mathcal{H}_{5}$
$\mathcal{H}_{6}$
…
$\mathcal{H}_{N-1}$
$\mathcal{H}_{N}$
$\mathcal{H}_{N+1}$
$\mathcal{H}_{N+2}$
$\mathcal{H}_{N+3}$
Semi-infinite Left Lead
Device
Semi-infinite Right Lead

Figure 2.2. Schematic of the transport calculation showing the break-up of the simulation region into a device region that includes source, channel and drain regions (green shade), and semi-infinite source and drain contacts at the two ends. The layer to layer interaction matrix is shown for only one interaction in the schematic (H_{12}). In practice, there are a large number of slices in the device region, depending on the length of the device simulated.

2.2.3 Transport Calculation

The eigenfunctions of the leads form a complete basis that is used for injecting probability density into and extracting probability density from the device region. For the two central layers in the left lead, and for each energy, the eigenfunctions can be arranged into a basis matrix $\mathbf{B}_{\mathrm{L}}$, as [20]:

$$\mathbf{B}_{\mathrm{L}} = \begin{bmatrix} \boldsymbol{\psi}_{-1}(\rightarrow) & \boldsymbol{\psi}_{-1}(\leftarrow) \\ \boldsymbol{\psi}_{0}(\rightarrow) & \boldsymbol{\psi}_{0}(\leftarrow) \end{bmatrix}, \qquad 2.5$$

Here $\boldsymbol{\psi}_0$ is now a square matrix where each row represents a particular orbital of a particular atom as before, and each column represents a particular transverse mode in the left lead (source side). And → (←) indicate the basis functions that either propagate or decay towards right (left). Similarly the basis function $\mathbf{B}_{\mathrm{R}}$ can be constructed for the two central layers, N+1 and N+2, in the right lead (drain side).

Within the simulation region, $\mathbf{B_0}$ can then be propagated to the right one layer at a time via transfer matrices $\mathbf{T}_l$

$$\mathbf{T}_l = \begin{bmatrix} \mathbf{0} & \mathbf{1} \\ -\mathbf{H}_{l,l+1}^{-1}\mathbf{H}_{l,l\text{-}1} & -\mathbf{H}_{l,l+1}^{-1}\; E - \mathbf{H}_{l,l} \end{bmatrix}, \qquad 2.6$$

such that

$$\begin{bmatrix} \boldsymbol{\Psi}_l \rightarrow & \boldsymbol{\Psi}_l \leftarrow \\ \boldsymbol{\Psi}_{l+1} \rightarrow & \boldsymbol{\Psi}_{l+1} \leftarrow \end{bmatrix} = \mathbf{T}_l \begin{bmatrix} \boldsymbol{\Psi}_{l-1} \rightarrow & \boldsymbol{\Psi}_{l-1} \leftarrow \\ \boldsymbol{\Psi}_l \rightarrow & \boldsymbol{\Psi}_l \leftarrow \end{bmatrix}, \qquad 2.7$$

Here the Hamiltonians **H** are adjusted for changing coupling potentials, and onsite potentials including the self-consistent changes to the electrostatic potential.

In principle at least, by cascading the transfer matrices and imposing appropriate boundary conditions, the complex transmission and reflection matrices **t** and **r** coupling each incoming mode to each outgoing mode, — one column and one row for each mode in the respective leads — for the entire device can then be calculated:

$$\begin{bmatrix} \mathbf{t} \\ \mathbf{0} \end{bmatrix} = \mathbf{B}_R^{-1} \mathbf{T}_{N+1} \mathbf{T}_N \ldots \mathbf{T}_2 \mathbf{T}_1 \mathbf{B}_L \begin{bmatrix} \mathbf{1} \\ \mathbf{r} \end{bmatrix}, \qquad 2.8$$

Propagation from the drain can be handled similarly.

In practice however Eqn. (2.8) is extremely unstable. We have followed the stabilization method developed by Usuki *et al.* [20] to solve for the **t** and **r** matrices, but the wave-functions are obtained using a simpler, equivalent method given in [25].

Carrier density n is obtained from the probability density associated with the wave functions injected from source (left), $n(\rightarrow)$, as well as drain (right), $n(\leftarrow)$. $n(\rightarrow)$ is calculated for each atom α in the device by summing over the probability density in each orbital β in each incident propagating mode χ:

$$n_\alpha \rightarrow = \int dE \sum_\beta \sum_\chi \left| \psi_{\alpha,\beta,\chi}(E) \right|^2 f_s(E), \qquad 2.9$$

Then n is fed into Poisson's equation to solve for the electrostatic potential which, in turn, is self-consistently fed back into Eqn. (2.1).

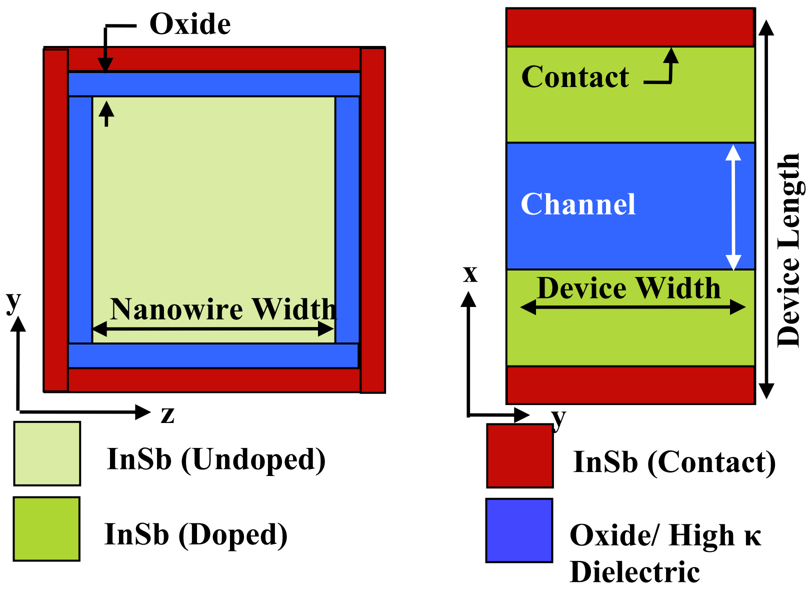
Oxide
Nanowire Width
y
z
Contact
Channel
Device Width
Device Length
x
y
InSb (Undoped)
InSb (Doped)
InSb (Contact)
Oxide/ High κ Dielectric

Figure 2.3. Schematic of the device simulated: (left) the cross-section of the channel region, perpendicular to the transport direction and (right) the view from the top showing the source and drain contact at the ends, and the gate oxide in the middle, surrounding the channel.

y semiconductor devices as channel lengths scale to few tens of nm [15], necessitating full quantum transport simulation

Once a self-consistent solution is obtained, the total charge current due to injection from the source side (I) can be calculated from the normalized wavefunctions $\boldsymbol{\psi}_{l,\chi}(E)$ for arbitrary temperature and bias from

$$I \rightarrow = q\sum_{\chi} \int dE \frac{2}{\hbar} \mathrm{Im}\left[\boldsymbol{\psi}^{\dagger}_{l,\chi}(E)\mathbf{H}_{l,l+1}\boldsymbol{\psi}_{l+1,\chi}(E) \right] f_S(E), \qquad 2.10$$

at any point within the simulation region, where q is the electronic charge, and χ labels the mode and l the layer. Here f_S is the Fermi function at the source contact, and the integration is performed over the range of applied bias plus or minus a few k_BT/q to account for non-zero temperature effects, where k_B is Boltzmann's constant and T is the temperature.

The method of calculating transmission probabilities that we follow [20] is similar to Ando's formalism [26], and Khomyakov *et al.* [27] have discussed the equivalence of this approach with that of the Green's function techniques [21, 28]. Gilbert and Ferry adapted this method to calculate 3D quantum transport in Si-on-insulator metal-oxide-semiconductor FET devices within an effective mass approach [8]. We note that the numerical approach used here is, beyond being an atomistic tight-binding approach, quite different than that used in [29].

2.3 RESULTS OF BAND-TO-BAND TUNNELING IN III-V NANOWIRE FETS

The schematic of a gate-all-around InSb nanowire FET is shown in Fig. 3. For computational ease, we have restricted the nanowire widths to 26.92, 32.40 and 38.88 Å, corresponding to 4, 5 and 6 atoms along the width, respectively. The device has an alumina (Al_2O_3) high-κ gate dielectric, with an effective oxide thickness of 6.48 Å, where the high-κ dielectric material is modeled pseudo-atomistically by taking appropriate empirical obtained TB parameters to produce a band gap corresponding to Al_2O_3, with band offset to InSb as reported in [30] with a type I interface.

2.3.1 Band Structure of [100] square InSb nanowire

The band-structure of an ultrascaled square (100) InSb nanowire of width 26.92 Å is shown in Fig. 2.4. The conduction and valence band edges shift to -0.28 eV and 0.78 eV, respectively, from the bulk values being 0 and 0.23 eV for the set of TB parameters used [22] illustrating the considerable increase of band gap induced by very strong confinement.

In Fig. 2.5, the self-consistent I_D-V_G characteristics are shown for ballistic transport in square (100) InSb nanowires of widths 26.92 and 32.40 Å. While these extremely narrow cross-sections (corresponding to 4 and 5 atoms wide) may not be realized in practice, the simulations serve to illustrate the band-to-band tunneling (BTBT) that ails any low band gap semiconductor.

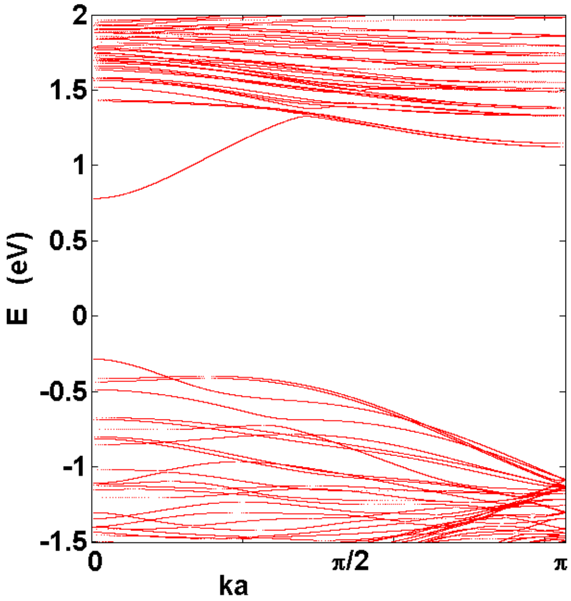

Figure 2.4. Energy dispersion relationship of the multiple quantum confined subbands of a square (100) InSb nanowire of width 26.92 Å.

For large negative V_G, the valence band is pulled up under the gate, allowing electrons injected from the conduction band of source to tunnel into the valence band in the channel, giving rise to OFF state BTBT leakage current. This leakage current decreases with decreasing nanowire width, since wires with smaller cross-section have higher confinement-induced band gap, which reduces the overlap of bands, thereby reducing the current. The peak drain current, however also decreases slightly on reducing the cross-section (see the linear I_D-V_G in the inset of Fig. 2.5) likely due to an overall reduction in injected carrier velocities resulting from strong confinement combined with non-parabolicity.

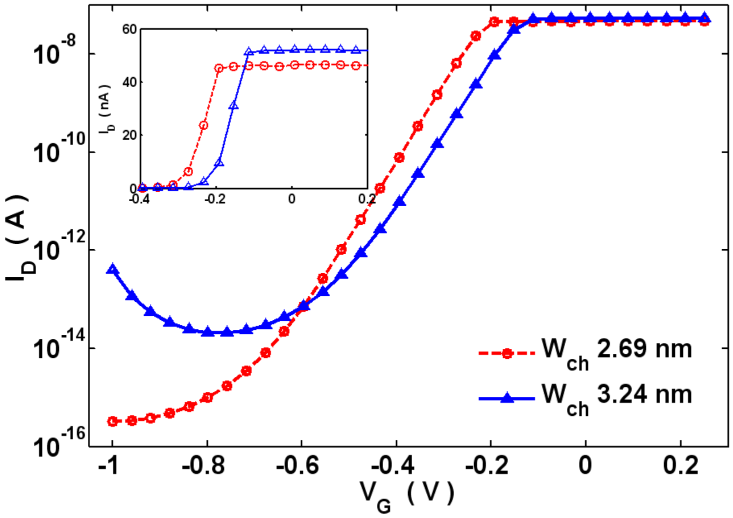

Figure 2.5. I_D-V_G for two square (100) InSb nanowire MOSFETs in a gate-all-around architecture, having identical channel length of L_{ch} = 5.2 nm. Inset: I_D-V_G in linear scale. Lower BTBT in narrow nanowires reduces I_{OFF}, but peak I_D is also slightly reduced for narrow nanowires.

In the OFF state, band-to-band leakage, and thus I_D is also be reduced by increasing the channel length (L_{ch}) due to an increase in the barrier thickness and an associated decrease in tunneling probability. This reduction can be seen in Fig. 2.6 for two devices with different L_{ch} (5.4 and 10.2 nm) but same nanowire width (W_{ch} = 3.24 nm) where the minimum subthreshold current decreases by ~ 3 orders of magnitude. In the ballistic limit, I_{ON} remains unaffected by the increase of L_{ch} (inset of Fig. 2.6) although gate capacitance and required drive current would increase. And with some diffusive transport, however, I_{ON} would also be expected to decrease with the increase of L_{ch}. As a consequence, L_{ch} would have to be optimized to achieve the best combination of I_{ON} and low I_{OFF}.The band-structure of an ultrascaled square (100) InSb nanowire of width 26.92 Å is shown in Fig. 2.4. The conduction and valence band edges shift to -0.28 eV and 0.78 eV, respectively, from the bulk values being 0 and 0.23 eV for the set of TB parameters used [22] illustrating the considerable increase of band gap induced by very strong confinement.

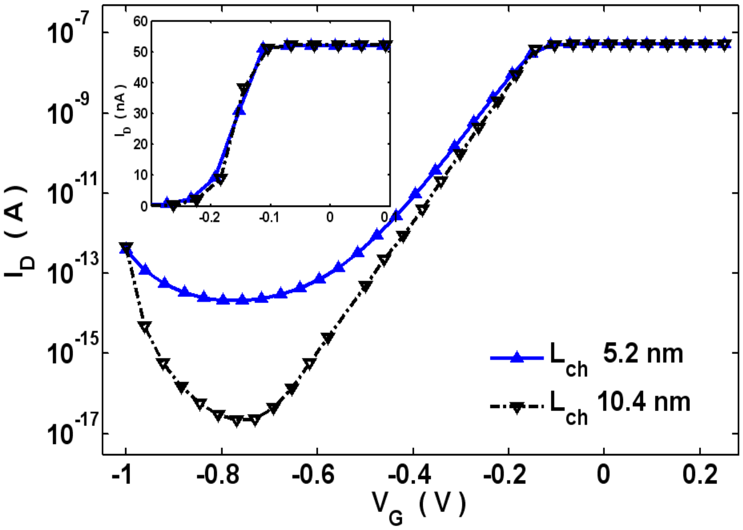

Figure 2.6. I_D-V_G for two square (100) InSb nanowire MOSFETs, having same W_{ch} = 3.24 nm, and different L_{ch}. Longer L_{ch} has lower minimum I_{OFF} due to reduced BTBT. In absence of scattering, peak I_D is unchanged with L_{ch}, as the inset (linear plot of I_D-V_G) confirms.

2.4 APPLICATIONS TO OTHER DEVICES

Before moving on to the conclusion, we would like to mention that we have been able to use this program for a variety of other applications. For example, Hui Chen in our group, while looking at the heterojunction field-effect devices had been using Franz two band model based on corrected WKB method [31], for calculating tunneling transmission in InSb across a barrier of height 1.13 eV for a band overlap of 100 meV. Since confinement induced band structure changes are not automatically modeled in such a formulation, he used this full band treatment to compare results, which show a fair match (Fig. 2.7) after the effective band mass in the two band model was adjusted.

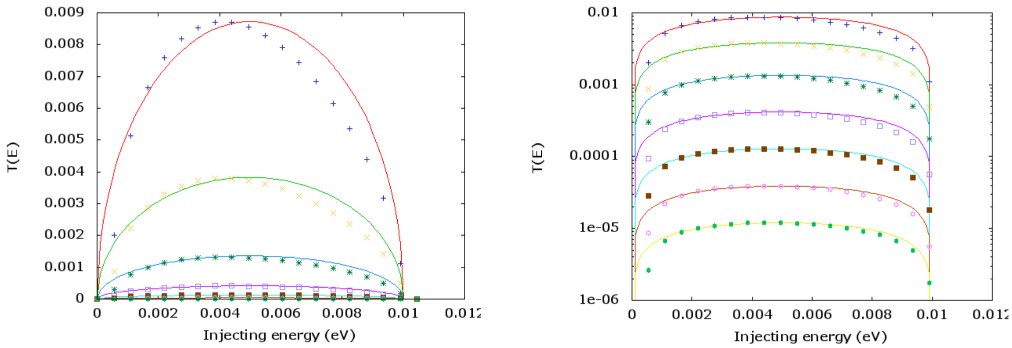

Figure 2.7. Transmission as a function of injection energy in InSb for a barrier of height 1.1 eV when injected from InSb nanowire, as a function of the barrier length (top-down increases by one monolayer, starting from 1. W_{ch} = 3.24 nm. The symbols are from the full band simulator, and solid line from Franz two band model, with effective mass adjusted to fit the full band result.

2.5 CONCLUSION

Here we present our transmission matrix based approach to ballistic quantum transport calculation for full three-dimensional, atomistic simulations using a tight-binding basis with nearest-neighbor interactions. The method is a variant of the more commonly used non-equilibrium Green's function and is versatile enough to be applied to a variety of applications due to its atomistic nature. In the following chapter we will apply this method to graphene nanoribbon channel MOSFETs, in particular to the effect of edge roughness in such devices, and very briefly, to resonant tunneling between electrons in two monolayers of graphene.

Chapter 3: Effect of edge roughness in graphene nanoribbons channel MOSFETs

As mentioned in the first chapter, ever since the isolation of graphene in 2004 [12], there has been a tremendous effort not only in understanding and experimentally realizing the unique physics offered by this inherently 2D electron system, but also to harness the excellent electrical properties that can be realized from pristine, defect-free samples of graphene. Because of this tremendous interest, the field of graphene research remains a very fast paced one. An excellent overview of the potential use and the physics of graphene can be found in recent review articles like [13, 32, 33].

3.1 BACKGROUND FOR STUDYING THE EFFECT OF EDGE ROUGHNESS

The first field-effect device using graphene as the channel material was demonstrated experimentally by Max Lemme in 2004 (the channel width was ~ 265 nm) [34]. Theoretical calculations focusing on narrow, perfect armchair nanoribbons as channel material for MOSFETs predicted high performance [35-37]. It has been possible to pattern graphene into ribbons of widths in the order of tens of nanometers [38]. However, narrow samples of graphene with perfect edges have been difficult to fabricate [39], and even though significant progress has been made in recent times to grow smooth narrow ribbons by chemical and self-assembly methods [40], lithographically the task remain very challenging. This prompted us to investigate the effect of these edge imperfections on transport in graphene nanoribbons.

3.1.1 Band structure of monolayer graphene

Bulk graphene has a two-dimensional hexagonal lattice with a two atom basis. Since only the electrons in the p_z (π) orbital participate in transport, it suffices to represent graphene by its π orbital [41, 42]:

$$H_{ij} = tN_{ij} - q\phi_i\delta_{ij}, \tag{3.1}$$

Here N_{ij} is 1 for the honeycomb lattice nearest neighbors, and is zero otherwise, and t is the nearest neighbor C-C hopping energy and is taken commonly as –2.7 eV for symmetric conduction and bands [42]. φ is the self-consistent electrostatic potential that we will consider only in the context of device simulation. The bulk band structure of graphene is metallic, and the conduction and valence bands touch one another at E=0, with the dispersion nearly linear for low energies.

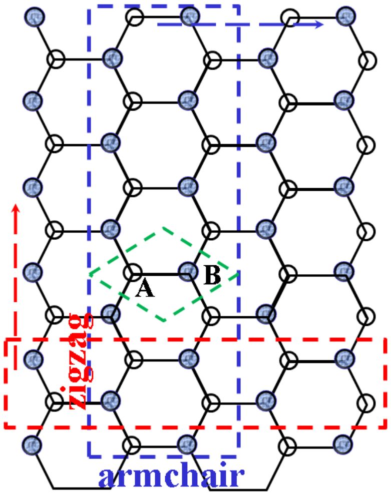

Figure 3.1. Armchair (horizontal ribbon) and zigzag (vertical ribbon) nanoribbon edge configurations and associated primitive unit cells along the ribbon. The green rhombus shows the primitive cell for bulk monolayer graphene containing one each of A and B sublattice C atoms (white and blue circles).

Ribbons of graphene come in two basic edge configurations, armchair and zigzag. (See Fig. 3.1). The primitive cell in the 1D ribbon is a rectangle spanning the entire width of the ribbon, and four layers along the length. The repeat unit of four layers allows us to use the same relations as were developed in Chapter 2. Tight-binding theory predicts that zigzag nanoribbons have localized edge states near the Fermi level, making them less attractive for channel material [43], although consideration of finer details, e.g. spin degree of freedom for the zigzag ribbon edges, or passivation of dangling bonds at the edges by different functional groups resulting possibly in different bonding strengths at the edge atoms may lead to the appearance of nonzero band gaps [44, 45]. Armchair nanoribbons, on the other hand, have a linear conduction and valence subband touching at E=0 as in bulk graphene, making it a gapless semiconductor if the number of atoms along the width is $3p+1$, otherwise, there is a band gap, the gap being inversely proportional to the ribbon width (p is an integer) [43].

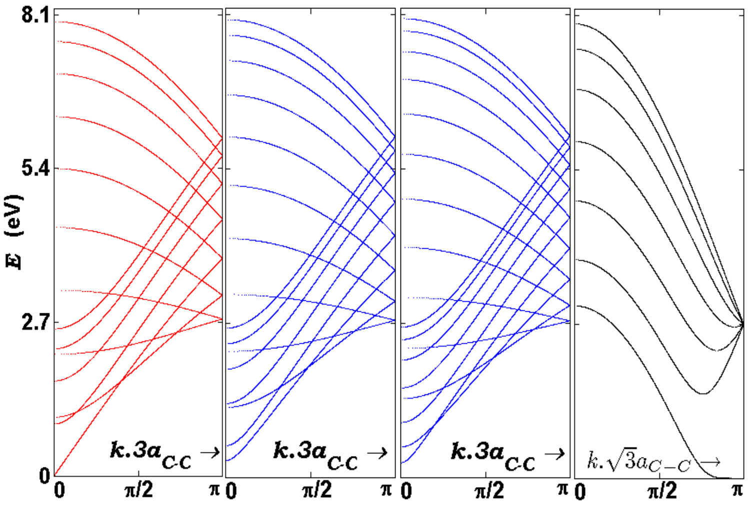

Figure 3.2. First three dispersion relations from left to right: conduction band subbands for graphene nanoribbons having armchair edges of 1.6, 1.8 and 2.0 nm widths, or 7, 8 and 9 atoms along a line. Extreme right dispersion relation: zigzag nanoribbon of 1.14 nm width corresponding to 7 atoms along a line. Energy is reference to the nominal Dirac point energy. All zigzag nanoribbons, and armchair nanoribbons having $3p+1$ atomic width, where p is an integer, have states at $E = 0$. a is the C-C bond length (1.42 Å).

The band structure for armchair graphene nanoribbons having 7, 8 and 9 atoms along the width of the armchair edge (armchair width of 1.6, 1.8 and 2.0 nm respectively) is shown in Fig. 3.2. The pattern of zero gap for $3p+1$ atoms and semiconductor otherwise makes the energy dispersion near E=0 extremely sensitive to the width of the nanoribbons, prompting us to investigate the effect of irregular edges on the transport characteristics of armchair nanoribbons.

3.2 MODELING EDGE ROUGHNESS

At the edges of graphene ribbons, C atom vacancies with respect to what would be a perfect armchair edge, give rise to steps [39]. We have modeled these edges by defining a correlation number *r* as the fraction of times the state of an edge site is identical to the corresponding site in the preceding slice, the 2D graphene nanoribbon being conjured up as a series of single atom thick slices along the transport direction. For *r* = 0.9, steps in the edge occur 10% of the time, either from a series of C atoms to vacant sites or vice versa. Edge sites are randomly vacant for *r* = 0.5. And with *r* = 1.0, a perfect armchair edge is achieved. A graphene sheet 10.5 nm long and 4.18 nm wide with *r* = 0.9 is shown in Figure 3.3(a).

At the edges of graphene ribbons, C atom vacancies with respect to what would be a perfect armchair edge, give rise to steps [39]. We have modeled these edges by defining a correlation number *r* as the fraction of times the state of an edge site is identical to the corresponding site in the preceding slice, the 2D graphene nanoribbon being conjured up as a series of single atom thick slices along the transport direction. For *r* = 0.9, steps in the edge occur 10% of the time, either from a series of C atoms to vacant sites or vice versa. Edge sites are randomly vacant for *r* = 0.5. And with *r* = 1.0, a perfect armchair edge is achieved. A graphene sheet 10.5 nm long and 4.18 nm wide with *r* = 0.9 is shown in Figure 3.3(a).

3.2.1 Device Schematic

For the sake of investigation into device characteristics, following [35], we consider a dual gate MOSFET structure where conduction occurs in the graphene layer sandwiched between top and bottom SiO_2 layers. Source and drain regions are n+ doped to a concentration of 10^{13} cm^{-2}, and are contacted by perfectly matched semi-infinite graphene leads. The channel region is nominally undoped. Fig. 3.3(b) shows a schematic of the graphene nanoribbon dual gate MOSFETs.

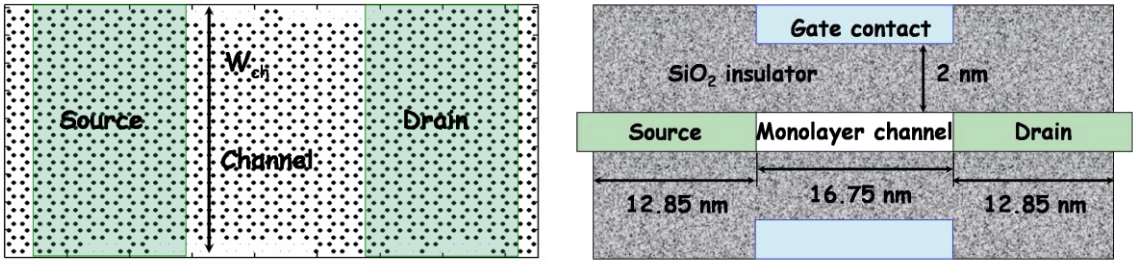

Figure 3.3. Left: (a) Top view of an armchair graphene nanoribbon channel, showing vacant sites along the edges where C atoms (black dots) are missing. Right: (b) Schematic of the double gate MOSFET simulated (side view). For clarity, the nanoribbon of (a) is shorter (10.5 nm) than that used in the simulated MOSFET.

3.3 RESULTS

3.3.1. Effect of edge roughness and width on transmission

The transmission characteristics for imperfect nanoribbon channels of varying nominal widths (W_{ch}) are shown in Fig. 3.4(a) under flatband conditions ($\varphi = 0$). In each case, atomically identical edges with edge roughness characterized by $r = 0.90$ were used. Results with perfect edges ($r = 1$) are shown for comparison. Disorder introduces scattering. As the width is scaled down the impact of the edge disorder increases and transmission goes down, with very poor transmission in the narrow ribbons. Fig. 3.4(b) shows the transmission characteristics for 7.63 nm wide graphene channel with five different values of the edge roughness parameter r. It is evident that transmission falls drastically as the correlation r falls below 0.99.

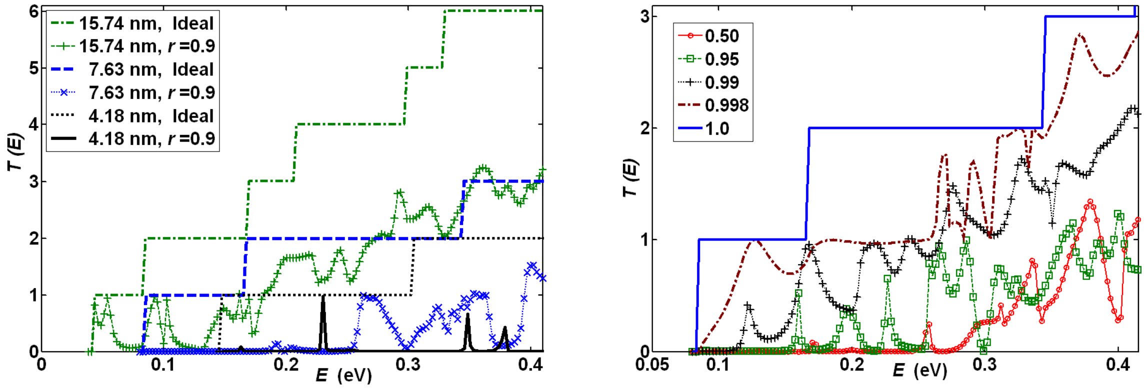

Figure 3.4. Left: (a). Transmission *T(E)* as a function of incident energy *E* across graphene channels having identically rough edges. Right (b) *T(E)* vs. *E* for a 7.63 nm wide graphene channel having different roughness at the edges. r = 0.5 has edge sites randomly vacant and r=1.0 has a perfect armchair edge. Steps show perfect transmission for ideal armchair edges of corresponding width.

3.3.2. Double gate MOSFET $I_D - V_G$ in presence of edge roughness

The drain current per unit width, I_D/W_{ch} for dual gate graphene channel MOSFETs with atomically identical edges characterized by r = 0.9 (we use the same edge configuration here as for the simulations of Fig. 3.4(a)) but different widths, are shown in Fig. 3.5(a) as a function of V_G. In these electrostatically self-consistent simulations, charge accumulates on the C atoms in the vicinity of the steps, resulting in variations in the potential and, this introduces additional scattering on top of scattering introduced by disorder. The degradation of I_D is large above threshold. As expected, I_D is relatively less affected for the widest device, i.e., having W_{ch} = 15.74 nm. However, only for the narrowest ribbon (W_{ch} = 4.18 nm) is the subthreshold behavior marginally acceptable for a MOSFET even with atomically smooth nanoribbon edges, a consequence of band-to-band tunneling mediated leakage currents. Also, Fig. 3.5(a) reveals that leakage in the nominally OFF state increases in the presence of edge roughness. The graphene nanoribbons considered here are nominally semiconducting, i.e., they are so in the limit of no edge roughness. From Fig. 3.2, a metallic or semiconducting energy dispersion relation emerges if the number of C atoms along the width is $3p+1$, or otherwise. With some of the edge sites vacant, one gets an admixture of different widths, resulting in quasi-localized defect states within the band gap, which contributes to the OFF state leakage.

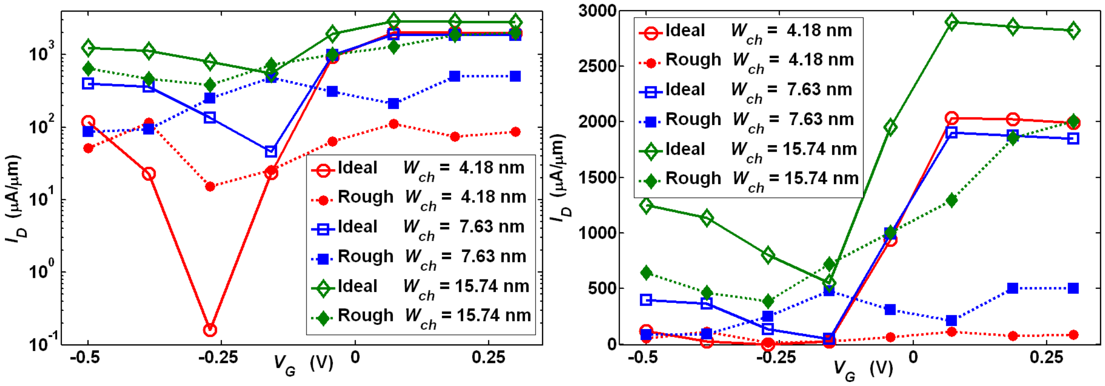

Figure 3.5. I_D–V_G characteristics on Left (a) log-linear and Right (b) linear-linear scale for the MOSFET structure of Fig. 1, for three different channel widths, showing performance degradation for channels with rough edges (dashed lines, solid symbols) from the ideal ballistic devices (solid lines, open symbols). $V_D = 0.2$ V.

3.3.3. Variability and performance issues due to edge roughness

Edge roughness leads to significant variability among devices with different atomic edge configurations for the same correlation parameter r and channel width. This variability can be seen in Fig. 3.6(a) in I_D/W_{ch} for two set of devices with $W_{ch} = 4.18$ nm, one set with $r = 0.99$ and one set with $r = 0.5$ values. The error bars represent plus or minus the standard deviation for a set of ten different random edge configurations with identical r. Even with $r = 0.99$ there is a large variability.

The performance penalty incurred for reducing BTBT leakage current by increasing L_{ch} is small for graphene channel MOSFETs because of the high mobility of carriers in graphene. In a perfectly smooth edge graphene nanoribbon MOSFET, the leakage current would decrease with increase of L_{ch}, as can be seen in Fig. 3.6(b) (circles). However, for rough channel devices, the defects and associated localized states increase with increase of L_{ch}, thereby increasing the defect-induced OFF state leakage current. This is corroborated from the I_D of the rough devices in Fig. 3.6(b) (square symbols), where the leakage current of the longer channel MOSFET (L_{ch} = 32 nm) is not necessarily less than that of the shorter channel device (L_{ch} = 21 nm).

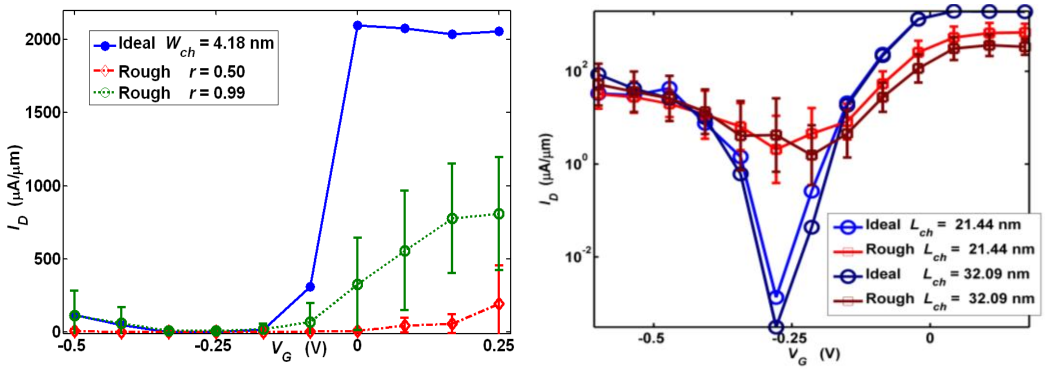

Figure 3.6. Left (a) I_D–V_G in linear scale for the dual gate MOSFET with W_{ch} = 4.18 nm and L_{ch} = 16.75 nm, using different values of edge roughness parameter r. Right (b) I_D–V_G for W_{ch} = 4.67 nm, for two different L_{ch}, using same r (=0.9). For both figures, error bars plotted indicate standard deviation in I_D across ten randomly different edges having macroscopically same values of r. V_D = 0.3 V for these simulations.

3.4 APPLICATIONS OF THE PROGRAM TO OTHER GRAPHENE-BASED DEVICES

In addition to looking at edge effects, we have applied the program to simulate several other cases, of which we will show two here.

3.4.1. On drain current saturation effects in graphene transistors

The I_D-V_D characteristics for low band gap semiconductors show an ambipolar characteristic that is obtained in some experimental reports on graphene field-effect transistors as well [46, 47]. To explore this behavior, we simulated the I_D-V_D characteristics for an armchair graphene nanoribbon in two limiting cases, having a metallic band structure, and that for a semiconducting one, and for two different widths, for the same device schematic as that of the previous study. The results are given in Fig. 3.7. Comparing the I_D for the narrow ribbons, we find that for the semiconducting one, I_D initially tends to saturate with V_D. This is the electron current that comes from the source injection, which sees a barrier. As V_D increases further, increasing overlap in energy between the drain conduction band with source valence bands sets in, leading to an increase in source-to-drain electron tunneling, or equivalently, hole transport from source to drain, so that I_D starts to increase again. For normal incidence (k_y=0 for transport along x), due to the Klein tunneling phenomenon [48], electrons do not see any barrier (same for the linear band in the metallic nanoribbon), and that gives the linear I_D-V_D for the narrow metallic channel device. For bulk graphene, where transport occurs in both linear as well parabolic bands, or equivalently, for off-angle incidence (k_y≠0) at the barrier, one can expect I_D in between these extremes.

For the larger channel width, we indeed find the I_D of these types coming together. Here transport occurs in more subbands, so that for the metallic armchair ribbons, the linear band does not dominate I_D. On the other hand, for the semiconducting ribbon, the band gap decreases, so that there is more tunneling current for larger V_D. The onset of tunneling can be postponed in these cases, by pushing E_F to a higher value by achieving a higher dopant density in the source drain region to reduce the ambipolar transport otherwise.

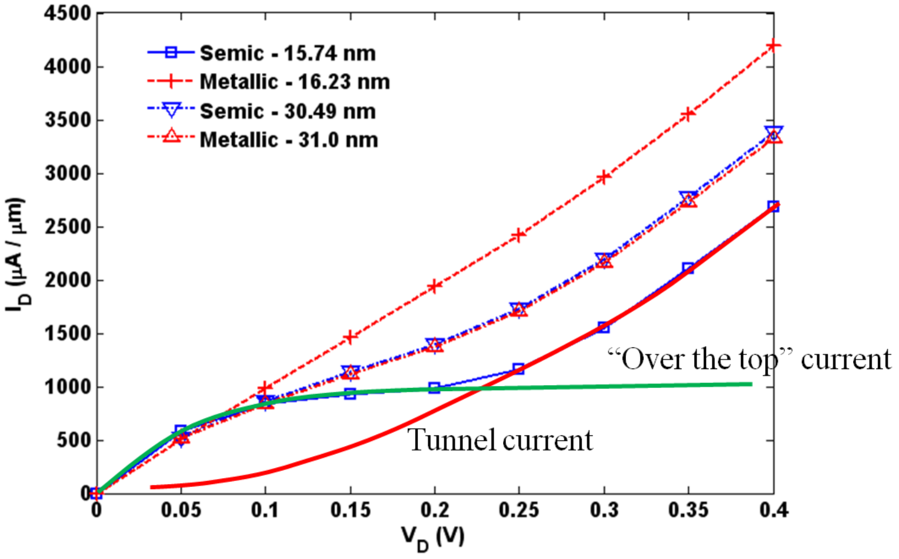

Figure 3.7. I_D-V_D characteristics for single layer armchair graphene nanoribbon having 42.46 nm device length, L_{ch} = 16.76 nm, T_{ox} = 2.5 nm, $N_{DS} = 5\times10^{12}$ cm^{-2} and V_G = -0.1 V The tunneling current and over the top current are visual aids to understand the components that make up the total I_D.

3.4.2. Resonant tunneling between electrons in two graphene bilayers

A variety of negative differential resistance (NDR) devices that operate on resonant tunneling phenomenon have been studied, why?. These devices are based on single particle tunneling unlike the possible coherent many body enhanced tunneling that is proposed in the next chapter [14], and therefore operate at a higher bias, in order to get a comparable tunneling [14]. We have utilized this NEGF-based single-particle simulator to study these devices and help understand the design issues of these devices. For example, to get a qualitative understanding of the broadening of the density of states in these system, we simulated the tunneling from the electron Fermi surface of top graphene layer (E_F at 150 meV from Dirac point) to bottom (E_F at 140 meV) for a normal graphene bilayer with a weak bare coupling (5 meV) between the layers. For this source-drain bias of 10 meV, we calculate the interlayer tunneling current (I_{il}) between the layers as a function of the interlayer potential (V_{il}), which serves to align the bands (at V_{il} =0) or otherwise destroy the resonance. The resulting I_{il} (shown in Fig. 3.8) as a function of V_{il}, which when normalized to the peak current, gives us the expected lorentzian distribution, from which the broadening of density of states with decrease of channel of length can be estimated (I_{il} increases with L_{ch} in Fig 3.8 due to the small coupling value chosen here).

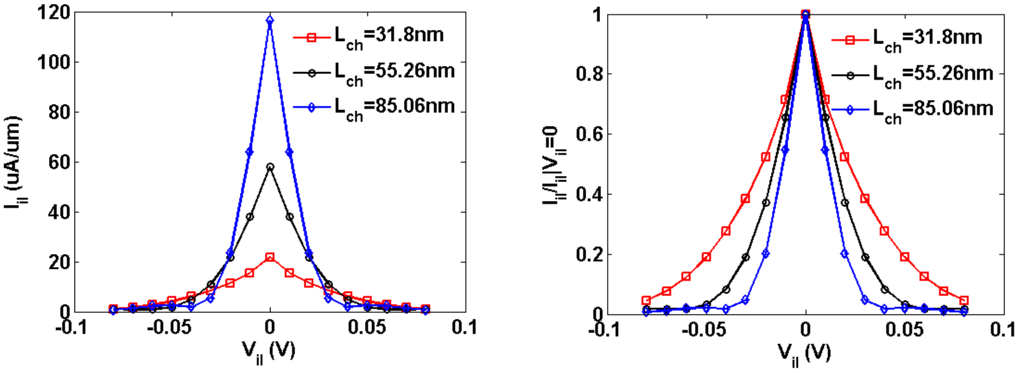

Figure 3.8. Resonant interlayer tunneling current (I_{il}) for a graphene bilayer as a function of the interlayer potential (V_{il}) that serves to align the bands at V_{il} =0, or destroy the resonance at $V_{il} \neq 0$, for three different channel lengths L_{ch} = 31.48 nm. Left (a) I_{il} normalized to the channel width (20 nm for all the three curves), and on right (b) normalized to maximum I_{il}

3.5 CONCLUSION

We found that monolayer-graphene-based logic devices that rely on the band gap of narrow ribbons to turn the devices OFF, suffer from the extreme sensitivity of the narrow ribbons to the edge disorder [49]. Similar conclusions were reached at elsewhere [50]. The variability is too high, I_{ON} low, and leakage in OFF-state high. For digital logic applications, where high I_{ON}/I_{OFF} ratio is a necessity, bilayer graphene offers a better prospect, since it is possible to create an electrically tunable gap in bilayers [51-53]. On the other hand, the high mobility of carriers in monolayer graphene makes it suitable for a plethora of applications, e.g., graphene FETs are potentially useful for low noise amplifiers (LNA) operating at tens of GHz [33]. LNA FETs do not require a high ON/OFF ratio as digital logic; a ratio of 3-10 is sufficient. This makes graphene FETs, which have low band gap at large graphene nanoribbon (GNR) widths, suitable for such applications, even if they might be inadequate for digital logic. We have also looked at other aspects of field-effect as well as tunneling-based graphene devices using the simulator discussed here.

However, graphene may serve not only a replacement channel material offering high carrier velocity; its novel properties may allow for fundamentally different mechanisms of switching, some of which has been reviewed in [32, 33]. In subsequent chapters, we will concentrate on one of these ideas and explore the physical conditions required for realization of the novel device based on electron-hole pair condensation in bilayer graphene.

Chapter 4: Tight-binding study of spontaneous electron-hole condensation in graphene bilayers

The electronic properties of bilayer graphene are quite different from monolayer graphene. The low-energy band structure of bilayer graphene reveals a parabolic dispersion unlike the linear bands of monolayer graphene, and an asymmetry in the potential of the two layers induces a band gap as predicted by phenomenological tight-binding models [51] as well as *ab initio* density functional calculations [53]. However, the band gap is limited to a value of about 0.3 eV because of the strong screening of the external potential in the graphene layers, and even that may be difficult to achieve [54], resulting in limited improvement of ON/OFF ratio in bilayer compared with monolayer graphene channel MOSFETs. Here however, we will focus on a novel phenomenon involving *collective* behavior of electrons and holes in two layers of graphene separated by a thin dielectric.

4.1 MOTIVATION FOR THE PRESENT WORK

4.1.1 Electron-hole coherence in bilayer graphene: background physics

In early 2008, researchers at Maryland and the University of Texas independently predicted that spontaneous coherence can occur in a bilayer graphene separated by a thin dielectric tunnel barrier, with electrons in one layer pairing up with holes in the other layer, to form a spontaneously coherent bilayer state that can be viewed as a Bose condensate of electron-hole pairs [55, 56]. Such a system supports persistent supercurrents in which electrons and holes flow in the same direction. Experimentally so far such coherent behavior has been realized only for semiconductor bilayer systems, and then only at extremely low temperatures and when the system is placed in a strong magnetic field which further enhances the tendency toward this type of collective behavior [57]. However, a synergy of the properties of graphene may make it possible for the condensate to manifest itself in graphene bilayers at much higher temperatures and zero magnetic fields—the ability to use closely-spaced atomically thin layers to maximize the interlayer Coulomb interaction; symmetric electron and hole band structures over the energy ranges of interest that allow accurate nesting between the electron and hole (2D) Fermi surfaces, a zero band gap (for bulk monolayer graphene) which allows all of any interlayer electrostatic potential difference to be used to induce electrons and holes, and a low density of states that leads to the desired high Fermi energies at relatively low carrier densities [55, 56, 58].

4.1.2 Device proposal utilizing the coherent state in bilayer graphene: the BiSFET

The possibility of room temperature exciton condensation, the enhanced low-bias tunneling expected in the many-body ordered state, and the possible gate control thereof prompted the design of an extremely low power logic device by researchers at the University of Texas, which could advance the international technology roadmap for semiconductors [14]. The device, which goes by the acronym BiSFET (**Bi**-layer pseudo**S**pin **F**ield-**E**ffect **T**ransistor), is not a simple drop-in replacement for MOSFETs. However, SPICE-based circuit modeling has demonstrated the possibility of creating a variety of logic elements with such devices with switching energies per device on the order of 0.01 aJ—i.e, 10 zepto-Joules (zJ)—discounting parasitics if such condensates can be formed and controlled [14, 59, 60]. By comparison, “end of the roadmap” CMOS is expected to have switching energies of roughly 5 aJ [1]. The qualitative advantages of this collective device concept flow from its use of gates to control *collective* rather than *individual* electron transport.

4.1.3 Physical assumptions behind the BiSFET *I-V*

Guided by experimental results in analogous low-temperature systems [57, 61-67] as well as theory [68, 69], researchers expect a negative differential resistance as the condensate collapses with increasing interlayer voltage (Fermi level splitting), perhaps beginning with voltages small compared to k_BT. A weakening of the condensate was also expected by relatively small charge imbalances (of perhaps 10%) which could be created by gating of the layers, as conceptually illustrated in Fig. 4.1(a), where it was assumed that the initial charge concentrations ($\sim 5\times 10^{12}/\mathrm{cm}^2$) could be induced under zero gate bias via differences in gate work functions or other means. If correct, the result would be low-voltage device characteristics qualitatively like those of Fig. 4.1(b). The functional form used for the BiSFET circuit simulations is of the form [14]:

$$I = G_o (V_p - V_n)\left[1 + \left(\frac{(V_p - V_n)/V_{\max}}{\exp(1 - |V_p - V_n|/V_{\max})}\right)^4\right]^{-1/4}, \tag{4.1}$$

with

$$V_{\max} = V_{\max,o}\exp(-10\,|\Delta p - \Delta n|/n + p) \tag{4.2}$$

where Δp and Δn are the variations in charge densities with all four terminal voltages and G_o is the Landauer-Büttiker conductance per unit gate width. While such device characteristics do not make for simple low-voltage drop-in replacements for MOSFETs, it was found to be possible to produce all basic logic functions within SPICE-based circuit simulations [14, 70]. Still, the BiSFET currently remains as only a concept based on novel physics predicted in a novel materials system. If such a device and/or other devices based on such a condensate are to be realized, the conditions under which this condensate can be created and controlled needs to be better understood, as well as experimentally realized.

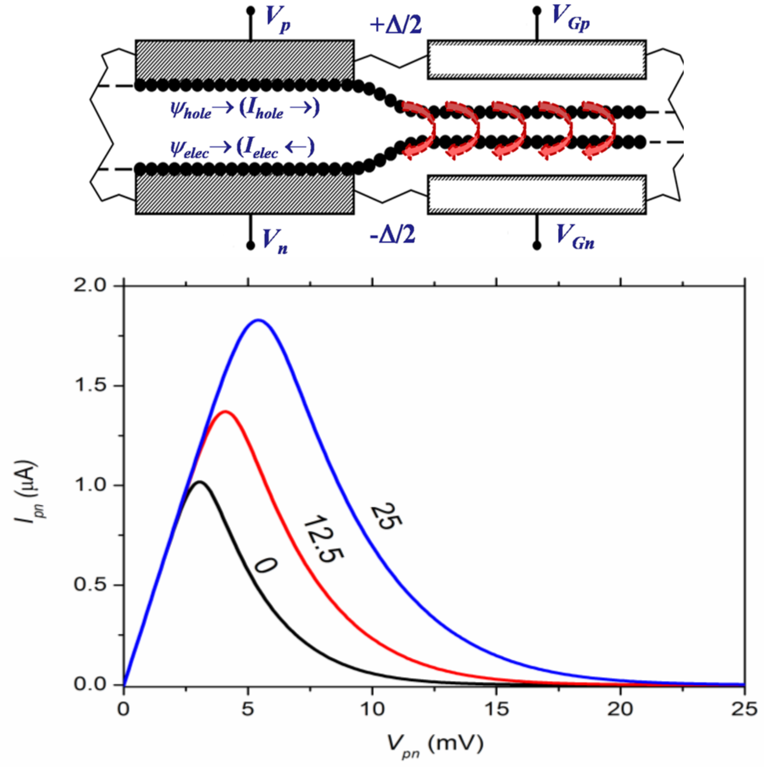

Figure 4.1. Top (a) Device schematic of BiSFET showing uncoupled graphene contacts, and coupled channel. Δ creates asymmetry between the top (hole) and bottom (electron) layers. Direction of wave function propagation and corresponding electrical currents are also shown. Bottom (b) *I-V* characteristics of BiSFET for three different gate voltages $V_{G,n}$ with $V_{G,p}$ = -25 mV consistent with Eqn. (4.1) and (4.2) and 20 nm gate width. Note that while the region of condensate formation is indicated schematically in (a) by reduced spacing between layers here, there are others ways to localize the condensate including changes in dielectrics, charge densities, and/or initial degree of charge balance.

4.2 MODELING INTERLAYER EXCHANGE INTERACTIONS IN GRAPHENE BILAYERS USING TIGHT-BINDING π-ORBITAL BASIS

The bilayer graphene model we study for this work is shown schematically in Fig. 4.2(a). The arrangement of the carbon (C) atoms in the primitive cell of the two coupled graphene layers is shown in Fig. 4.2(b). A uniform relative dielectric constant ε_r is assumed as a simple first-order approximation to the net effect of interlayer and gate dielectrics and gate-induced screening. *We start by neglecting the role of direct/bare single-particle hopping between layers. The only interaction between the two layers at this stage is the Coulomb attraction between electrons in one layer and holes in its neighbor.* The solutions thus obtained may only be applicable in the weak direct-coupling limit of course. For the purpose of definiteness, Fig. 4.2(b) shows a Bernal alignment between the two layers in the relative spatial arrangement of the atoms in most cases (A sublattice atom in top layer (A_T) located above B sublattice atom in the bottom layer (B_B)). However, our results do not change significantly—quantitatively or qualitatively—if the two layers are aligned hexagonally (A_T above A_B, and B_T on top of B_B).

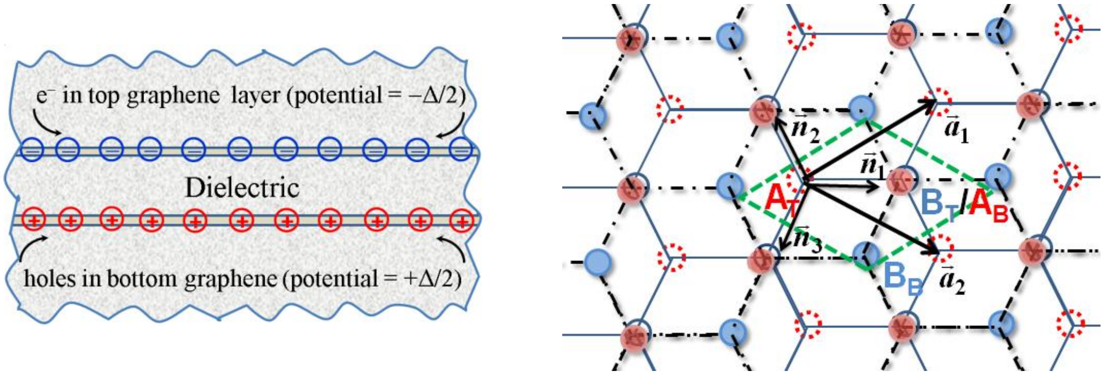
e⁻ in top graphene layer (potential = −Δ/2)
Dielectric
holes in bottom graphene (potential = +Δ/2)
$\vec{n}_2$
$\vec{a}_1$
$\vec{n}_1$
A_T
B_T/A_B
$\vec{n}_3$
B_B
$\vec{a}_2$

Figure 4.2. Left (a) Schematic of the two oppositely charged graphene monolayers, separated by a dielectric. Right (b) Arrangement of C atoms showing the primitive cell (green rhombus) containing four atoms — A_T (dotted circle) and B_T (blue circle) for the top layer C atoms, and A_B (red solid circle) and B_B (blue solid circle) for the bottom layer. This figure is for the Bernal stacking arrangement in which B_T lies directly above A_B. Also shown are the real space lattice vectors $\vec{a}_1$ and $\vec{a}_2$, and the vectors from A_T to the nearest neighbor B_T atoms, $\vec{n}_1$, $\vec{n}_2$ and $\vec{n}_3$

4.2.1 Modeling bilayer graphene to simulate BiSFET

Within Hartree-Fock (HF) theory many-body interactions are approximated by a non-local mean field potential $V_{\mathrm{HF}}(\mathbf{R_1},\mathbf{R_2})$ for the electrons. This potential can be written as the sum of three distinct potentials [71]which are:

$$\begin{aligned} V_{\mathrm{HF}}\ \mathbf{R}_1,\mathbf{R}_2\ &= \delta\ \mathbf{R}_1,\mathbf{R}_2\ V_{ext}\ \mathbf{R}_1\ + \delta\ \mathbf{R}_1,\mathbf{R}_2\ \sum_{\mathbf{R}_3} \frac{e^2}{4\pi\varepsilon_0\varepsilon_r\left|\mathbf{R}_1-\mathbf{R}_3\right|} \sum_{\beta} n_\beta \left|\varphi_\beta\ \mathbf{R}_3\ \right|^2 \\ &- \frac{e^2}{4\pi\varepsilon_0\varepsilon_r\left|\mathbf{R}_1-\mathbf{R}_2\right|} \sum_{\beta} n_\beta \varphi_\beta\ \mathbf{R}_1\ \varphi_\beta^*\ \mathbf{R}_2 \end{aligned}, \qquad 4.3$$

on our tight binding lattice, where **R** are the positions of the atoms, φ_β are the tight-binding electron energy eigenfunctions, and n_β are the occupancy factors, and the $\delta(\mathbf{R_1},\mathbf{R_2})$ are Kronecker delta functions in the discrete coordinates **R**. The first two terms are local, arising from the external field and the local charge density (Hartree potential) respectively, and the last term is the non-local exchange potential (Fock potential).

For this study of excitonic condensation in graphene bilayers, we are primarily interested in the *inter*layer exchange interactions,

$$V_{\mathrm{HF}}(\mathbf{R}_{\mathrm{T}},\mathbf{R}_{\mathrm{B}}) = \frac{-e^2}{4\pi\varepsilon_0\varepsilon_{\mathrm{r}}\sqrt{\ \Delta R\ ^2 + d^2}} \sum_{\alpha,\mathbf{k},s} n_{\alpha,\mathbf{k},s}\varphi_{\alpha,\mathbf{k},s}(\mathbf{R}_{\mathrm{T}})\varphi_{\alpha,\mathbf{k},s}^*(\mathbf{R}_{\mathrm{B}}), \qquad 4.4$$

Here $\mathbf{R_T}$ and $\mathbf{R_B}$ are the 2D in-plane vectors for the atoms in the top and bottom graphene layers, respectively. $\Delta R = |\mathbf{R_T} - \mathbf{R_B}|$ is the magnitude of the in-plane component of the separation between the atoms, and d is the separation between the two layers. And the eigenstates label β has been expanded in terms of the band index α, wave-vector **k**, and spin state s. The remaining potential, the Hartree terms and the *intra*layer Fock terms, serve to self-consistently determine the gate potentials which would be required to introduce a specific potential difference between the top and bottom layers. In this work we represent these latter contributions simply assuming a potential difference Δ, such that a $\mp\Delta/2$ potential is added to the top (electron) and bottom (hole) layers, respectively.

A self-consistent solution for $V_{\mathrm{HF}}(\mathbf{R}_{\mathrm{T}},\mathbf{R}_{\mathrm{B}})$ within an effective single-particle tight-binding Schrodinger equation is sought to approximate the true many-body ground state. For each value of α, $\mathbf{k}$, s, this Schrodinger equation can be written as:

$$H_{\mathrm{TB}}\varphi_{\alpha,\mathbf{k},s}(\mathbf{R}_{\mathrm{T}}) - \Delta/2\ \ \varphi_{\alpha,\mathbf{k},s}(\mathbf{R}_{\mathrm{T}}) + \sum_{\mathbf{R}_{\mathrm{B}}} V_{\mathrm{HF}}(\mathbf{R}_{\mathrm{T}},\mathbf{R}_{\mathrm{B}})\varphi_{\alpha,\mathbf{k},s}(\mathbf{R}_{\mathrm{B}}) = \varepsilon_{\alpha,\bar{k},s}\varphi_{\alpha,\mathbf{k},s}(\mathbf{R}_{\mathrm{T}}), \qquad 4.5$$

and

$$H_{\mathrm{TB}}\varphi_{\alpha,\mathbf{k},s}(\mathbf{R}_{\mathrm{B}}) + \Delta/2\ \ \varphi_{\alpha,\mathbf{k},s}(\mathbf{R}_{\mathrm{B}}) + \sum_{\mathbf{R}_{\mathrm{T}}} V_{\mathrm{HF}}(\mathbf{R}_{\mathrm{B}},\mathbf{R}_{\mathrm{T}})\varphi_{\alpha,\mathbf{k},s}(\mathbf{R}_{\mathrm{T}}) = \varepsilon_{\alpha,\bar{k},s}\varphi_{\alpha,\mathbf{k},s}(\mathbf{R}_{\mathrm{B}}) \qquad 4.6$$

for the top and bottom layers, respectively. Here, ε are the eigenenergies and H_{TB} is the nearest neighbor π-orbital (p_z-orbital for the assumed x-y oriented graphene planes) tight-binding Hamiltonian from which the single particle band structure is obtained using this Schrodinger equation, which can be written as:

$$H_{\mathrm{TB}}\varphi_{\alpha,\mathbf{k},s}(\mathbf{R}) = t\sum_{j}\varphi_{\alpha,\mathbf{k},s}(\mathbf{R}_j), \qquad 4.7$$

where $t = -2.7$ eV[42]. Note that $\varphi_{\alpha,\mathbf{k},s}(\mathbf{R})$ for any atom located at $\mathbf{R}''$ outside the four-atom primitive unit cell of the bilayer graphene system, can be obtained from the value for the corresponding atom with the primitive unit cell $\mathbf{R}'$ by using the Bloch condition $\varphi_{\alpha,\mathbf{k},s}(\mathbf{R}'') = e^{i\mathbf{k}\cdot(\mathbf{R}''-\mathbf{R}')}\varphi_{\alpha,\mathbf{k},s}(\mathbf{R}')$.

Self-consistent solutions to Eqs. (4.4)-(4.7) can be obtained simply by setting the interlayer exchange interaction of Eq. (4.4) to zero. This solution corresponds to an uncorrelated state with electrons isolated in one layer or the other, and bands in the two layers simply shifted by $\mp\Delta/2$. A self-consistent solution of Eqs. (4.4)-(4.7) that yields a non-zero value of the inter-layer exchange potential and eigenfunctions that are coherent sums of orbital amplitudes on both layers captures the condensate state [69]. As usual these solutions of the Hartree-Fock equations minimize the total energy subject to the Slater determinant wave-function approximation. When bare inter-layer tunneling terms are absent in the Hamiltonian, the state with inter-layer coherence, and therefore interaction terms in the mean-field Hamiltonian that act like inter-layer hopping/tunneling potentials for the Hartree-Fock quasi-particle, breaks the Hamiltonian symmetry which conserves particle number separately in each layer. The broken symmetry state has lower inter-layer Coulomb interaction energy because the anti-symmetry of the many-electron wave-function reduces the spatial overlap probability between electrons in different layers only when coherence is present. In terms of the quasi-particle energy spectrum, a gap is formed in the band structure of the two-layer system about the points at which the conduction band of the top layer and the valence band of the lower layer would otherwise cross. With the Fermi level in the vicinity of this anti-crossing, the energy reduction for the condensed state can be seen in the reduction of the energies of the occupied Hartree-Fock quasi-particle states in the vicinity of the anti-crossing.

For illustration, this gap formation for the correlated state at 0 K temperature with balanced charge distributions of 6×10^{12} cm^{-2} corresponding to an interlayer potential splitting Δ of 0.5 eV, with an interlayer spacing of 1 nm, and with a dielectric permittivity $\varepsilon_r = 3.9$ of SiO_2 is shown in Fig. 4.3 where the quasi-particle energy bands are plotted along the high-symmetry directions. The size of the gap in this case is ~30% of the isolated layer Fermi energies relative to their respective Dirac points.

To obtain this and subsequent correlated state solutions numerically, we used an iterative procedure and "seeded" the calculations for the first iteration only either by replacing the tight-binding wave-function correlation product $\varphi_{\alpha,\mathbf{k},s}(\mathbf{R}_\mathrm{T})\varphi^*_{\alpha,\mathbf{k},s}(\mathbf{R}_\mathrm{B})$ in Eq. (4.4) by $c\exp[i\mathbf{k}(\mathbf{R}_\mathrm{T}-\mathbf{R}_\mathrm{B})$ where c a small dimensionless constant; by replacing the exchange interaction of Eq. (4.4) with a Bernal-like or hexagonal-like but weaker bare interlayer coupling; or by starting from a self-consistent condensed state obtained previously under different conditions. In any case, for subsequent iterations the seed was removed and the Fock potential of Eq. (4.4) was obtained from the wave-functions of the previous iteration, and the calculation was iterated until convergence was achieved. We emphasize that we have confirmed through multiple tests that the final self-consistent solutions are not dependent on this initial seeding method or value.

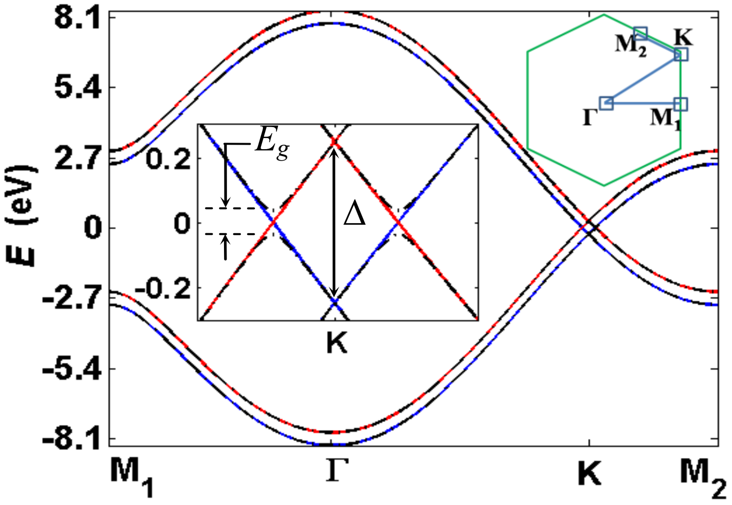

Figure 4.3. Energy bands of two graphene layers separated by 1.0 nm of SiO$_2$ ($\varepsilon_r = 3.9$), having layer potentials of $-\Delta/2$ (top layer – blue) and $+\Delta/2$ (bottom layer – red) in the uncoupled state (solid lines) along the high symmetry directions in the Brillouin zone (shown above). $\Delta = 0.5$ eV. Phase coherence between layers creates a correlated, lower energy state (black dash-dotted lines). The inset magnifies the low energy spectrum, revealing a band gap E_g of 74 meV at 0 K for balanced top and bottom layer charge distributions, i.e., E_F is located within the band gap in this case

4.3 RESULTS OF SPONTANEOUS EXCHANGE INTERACTIONS IN GRAPHENE BILAYERS

4.3.1 Characteristics of the real-space non-local exchange potential

The non-local mean-field exchange interaction appears as an effective inter-layer hopping term in the tight-binding Hamiltonian. For conceptual understanding, it is convenient to subdivide inter-layer exchange into four contributions distinguished by sublattice indices for both top and bottom layers. Coupling between an A sublattice atom in the top layer and an A sublattice atom in the bottom layer can be identified as an A_T-A_B interaction. Similarly A_T-B_B, B_T-A_B and B_T-B_B interactions can be identified.

The non-local nature of the exchange interaction is evident from the self-consistently calculated A_T-A_B exchange potential shown in Fig. 4.4, obtained under the same conditions as given above for Fig. 4.3. The rapidly oscillating dependence of this nonlocal potential on $\mathbf{R_B} - \mathbf{R_T}$ is apparent from the positive and negative excursions of the potential in Fig. 4.4. The picture becomes simpler if the contributions to $V_{\mathrm{HF}}(\mathbf{R_T},\mathbf{R_B})$ from states near the two Dirac points $\mathbf{k_D}$ are considered separately. (We have confirmed that the exchange potential contribution from near one Dirac point has little effect on quasi-particles near the other Dirac point, as assumed from the beginning in continuum model theories.) When we divide out the phase factor $\exp[i\mathbf{k}_{\mathrm{D}} \cdot (\mathbf{R}_{\mathrm{B}} - \mathbf{R}_{\mathrm{T}})]$ from the $V_{\mathrm{HF}}(\mathbf{R_T},\mathbf{R_B})$ contribution from near one or the other Dirac point $\mathbf{k_D}$ we obtain the potential $V'_{\mathrm{HF}}(\mathbf{R_T},\mathbf{R_B})$, illustrated in Fig. 4.5 for A_T-A_B and B_T-B_B interactions. To within the arbitrary constant phase factor for $V'_{\mathrm{HF}}(\mathbf{R_T},\mathbf{R_B})$ as a whole discussed above, the resulting functions A_T-A_B and B_T-B_B can be taken as purely real. Furthermore, the eigenstates of the coupled system $\varphi_{\alpha,\mathbf{k},s}$ that contribute most to the exchange interaction are necessarily those that significantly overlap both layers, those near the band anti-crossing centered about the nominal Fermi surface $k_{\mathrm{F}} = |\mathbf{k_F} - \mathbf{k_D}|$ location for the uncoupled system for these balanced charge distributions. The calculated exchange interaction decays not only with the large characteristic Coulomb decay of $(\Delta R^2 + d^2)^{-1/2}$, but also with spatial correlation of the condensate which, for typical gaps in these calculations for coupled graphene layers, has a characteristic scale of $\Delta R \sim k_{\mathrm{F}}^{-1}$.

The functions $V'_{\mathrm{HF}}(\mathbf{R_T},\mathbf{R_B})$ for A_T-A_B and B_T-B_B, while of identical magnitude, are of opposite sign. This result is expected because conduction and valence band (pseudo-)spinors at a given wave-vector differ only by the relative sign of their projections onto individual sublattices. This self-consistent coupling we obtain is of the form required to maximize the interaction between conduction band states in one layer and valence band states in the other layer. However, as evident from Figs. 4.6 and 4.7, $V'_{\mathrm{HF}}(\mathbf{R_T},\mathbf{R_B})$ for $\mathrm{A_T}$-$\mathrm{B_B}$ and $\mathrm{B_T}$-$\mathrm{A_B}$ coupling are complex functions of $\mathrm{R_B} - \mathrm{R_T}$ and have peak values that are quite a bit smaller than the $\mathrm{A_T}$-$\mathrm{A_B}$ and $\mathrm{B_T}$-$\mathrm{B_B}$ couplings, having only about one-fifth of the peak magnitude. Due to the chiral nature of graphene, the relative phases of the wave-functions on the A and B sublattices of each layer also vary rapidly with k around the Fermi surface. As a result, even for small ΔR, the mostly constructive phase interference among contributions of individual states $\varphi_{\alpha,\mathbf{k},s}$ to $V'_{\mathrm{HF}}(\mathbf{R_T},\mathbf{R_B})$ between A sublattice sites and between B sublattice sites, implies substantial destructive interference between the contributions to both $\mathrm{A_T}$-$\mathrm{B_B}$ and $\mathrm{B_T}$-$\mathrm{A_B}$ exchange potentials. We note that the mean-field interlayer coupling $V'_{\mathrm{HF}}(\mathbf{R_T},\mathbf{R_B})$ is quite distinct in character from any familiar single-particle interlayer coupling, whether Bernal-like or hexagonal-like. This observation will play a key role in the consideration of critical currents later.

There are also separate solutions of the mean-field equations with mostly constructive interference among the contributions for *either* $\mathrm{A_T}$-$\mathrm{B_B}$ *or* $\mathrm{B_T}$-$\mathrm{A_B}$ exchange potentials, but at a cost of substantial destructive interference for all three other combinations, and a corresponding weaker less energetically favorable total coupling, at least in the absence of bare coupling. As a result, in our self-consistent calculations of the spontaneous condensate, these solutions are unstable, as also to be expected physically.

Finally we note that shifting the bottom layer lattice slightly in real space to obtain a hexagonal spatial overlap ($\mathrm{A_T}$ above $\mathrm{A_B}$, $\mathrm{B_T}$ above $\mathrm{B_B}$) has essentially no effect on the exchange potentials and band structure. The spatial structure of the inter-layer hopping mean-field is determined almost exclusively by the sublattice structures of the wave-functions at the Fermi level in the separate layers, and hardly at all by the influence of relative atomic positions on interlayer Coulomb interactions because of the large interlayer separations d as compared to inter-atomic distances within the layers. Even in a strongly coupled bilayer (low temperature T, low ε_r, small d) the band gaps for real-space hexagonal and Bernal atomic arrangements are equal to within fractions of meVs of one another.

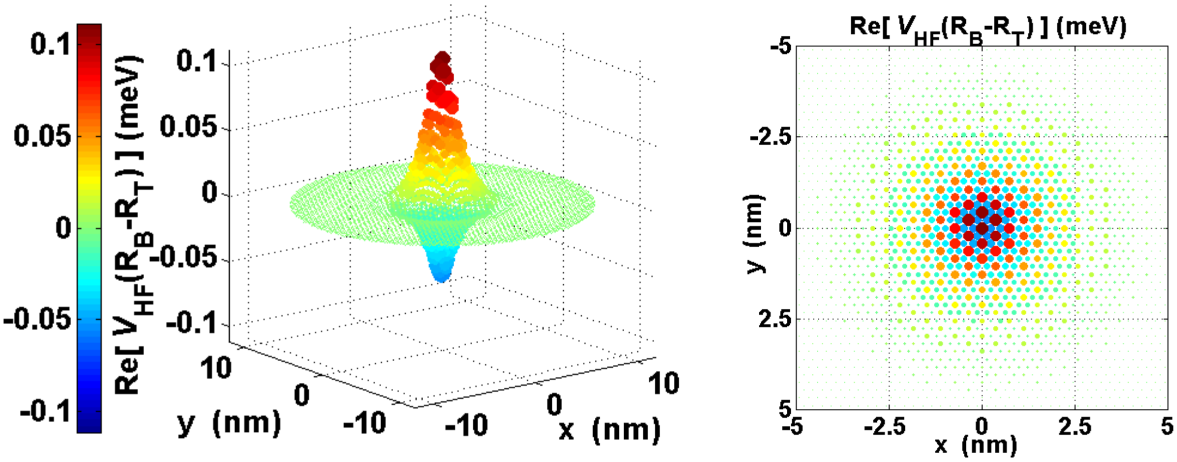

Figure 4.4. Left (a) The real-space variation of the exchange potential $V_{\mathrm{HF}}(\mathrm{R_T},\mathrm{R_B})$ for coupling between atoms of the A sublattices of top and bottom layers, as a function of $\mathbf{R_B} - \mathbf{R_T}$. $\Delta = 0.5$ eV, $d = 1$ nm, $\varepsilon_r = 3.9$, and balanced charge distributions at 0 K are assumed. Here and subsequent such plots, the color of the marker spheres indicate the value of the interaction, and the sizes of the spheres indicate the magnitude of this value. Right (b) Top view of the potential showing rapidly oscillating nature of $V_{\mathrm{HF}}(\mathbf{R_T},\mathbf{R_B})$

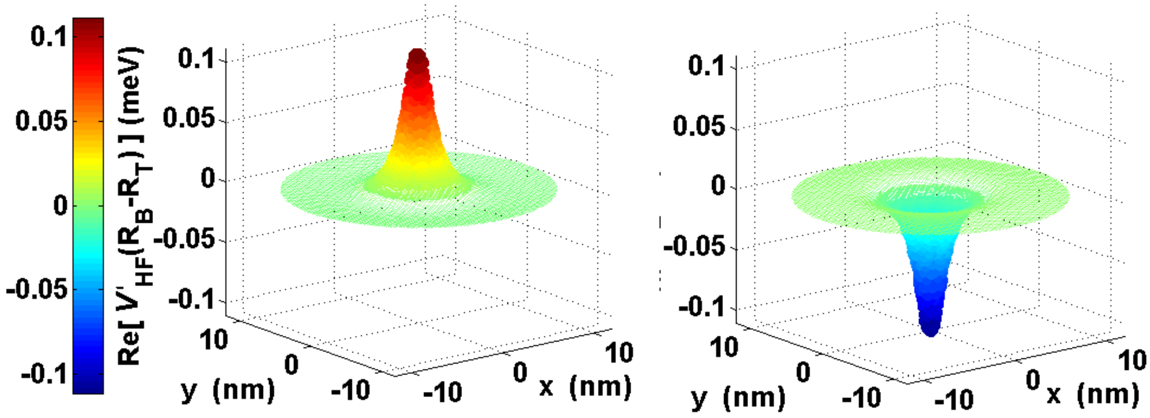

Figure 4.5. $V'_{\mathrm{HF}}(\mathbf{R}_{\mathrm{T}},\mathbf{R}_{\mathrm{B}})$ for (left) A_{T}-A_{B} coupling and (right) B_{T}-B_{B} coupling, obtained by dividing $V_{\mathrm{HF}}(\mathbf{R}_{\mathrm{T}},\mathbf{R}_{\mathrm{B}})$ by $\exp[i\mathbf{k}_D\cdot(\mathbf{R}_{\mathrm{B}}-\mathbf{R}_{\mathrm{B}})]$, as a function of $\mathbf{R}_{\mathrm{B}}-\mathbf{R}_{\mathrm{T}}$. The imaginary components vanish. $\Delta = 0.5$ eV, $d = 1$ nm, $\varepsilon_{\mathrm{r}} = 3.9$, and balanced charge distributions at 0 K are assumed.

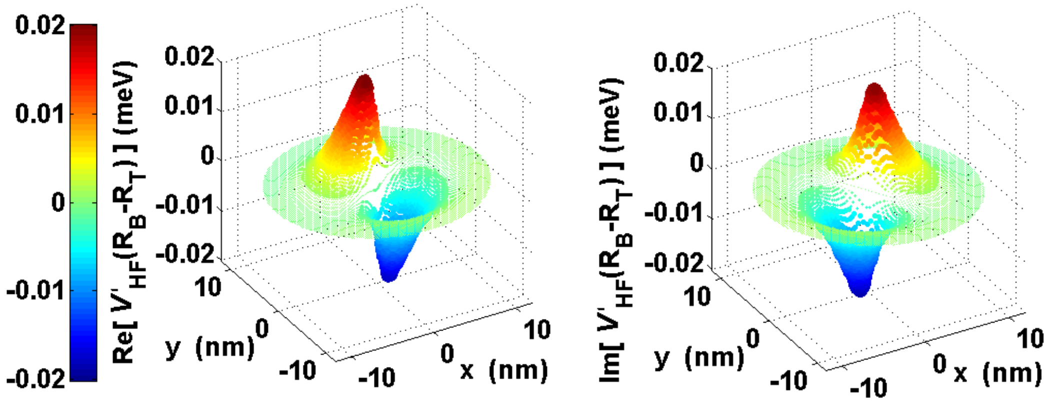

Figure 4.6. (Left) Real and (right) imaginary parts of $V'_{\mathrm{HF}}(\mathbf{R}_{\mathrm{T}},\mathbf{R}_{\mathrm{B}})$ for A_{T}-B_{B} coupling as a function of $\mathbf{R}_{\mathrm{B}}-\mathbf{R}_{\mathrm{T}}$. $\Delta = 0.5$ eV, $d = 1$ nm, $\varepsilon_{\mathrm{r}} = 3.9$, and balanced charge distributions at 0 K are assumed.

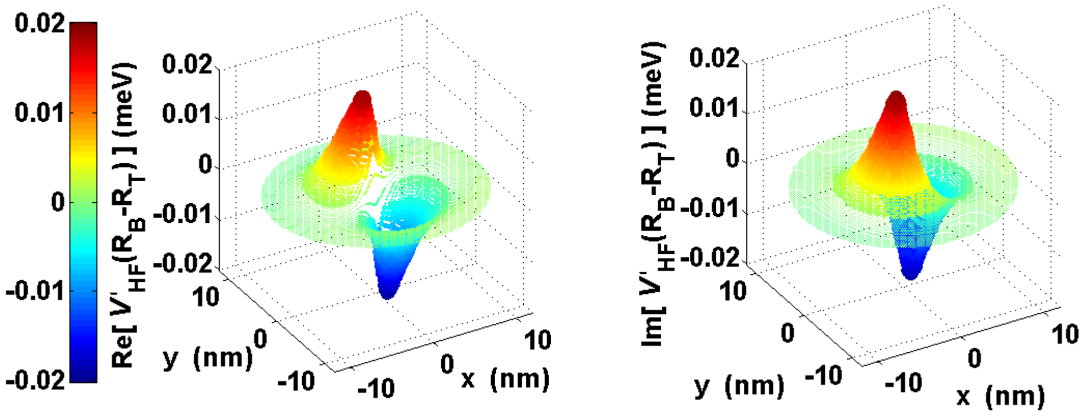

Figure 4.7. (Left) (Left) Real and (right) imaginary parts of $V'_{\mathrm{HF}}(\mathbf{R}_{\mathrm{T}},\mathbf{R}_{\mathrm{B}})$ for B_{T}-A_{B} coupling as a function of $\mathbf{R}_{\mathrm{B}} - \mathbf{R}_{\mathrm{T}}$. $\Delta = 0.5$ eV, $d = 1$ nm, $\varepsilon_{\mathrm{r}} = 3.9$ and balanced charge distributions at 0 K are assumed.

4.3.2 System parameter dependence

In bilayer systems an electric potential difference between layers is necessary to induce carriers and open up the opportunity for condensation. The dependence of the coherence-induced band gap, a measure of the condensate strength, on the electric potential difference Δ is shown in Fig. 4.8 for three different dielectric constants and a fixed interlayer spacing d of 1 nm. Note that there is continuous strengthening of the condensate with increasing Δ. However the rate of increase is smaller at large values of Δ. This diminishing *rate of return* is even more pronounced when viewed as a function of electron and hole densities, which scale as Δ^2 because of the linear band structure in contrast to the Fermi energy which is equal to Δ/2. On the other hand, $\Delta/2 = E_F$ should remain above roughly $8k_{\mathrm{B}}T$ where k_{B} is Boltzmann's constant, which is approximately 200 mV at room temperature.

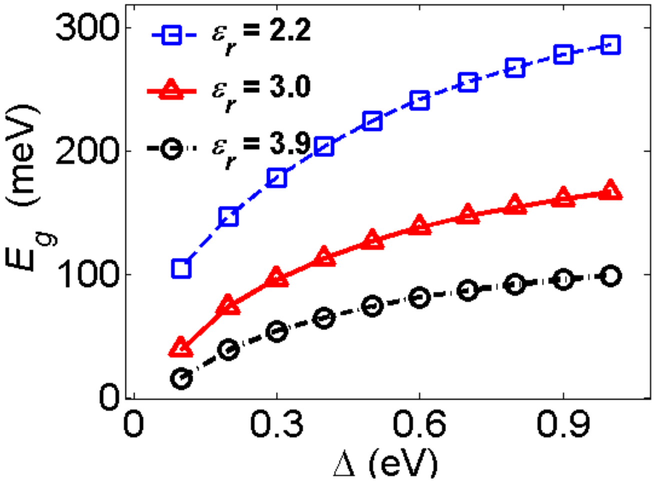

Figure 4.8. Band gap as a function of potential difference Δ for three different dielectrics, with $d = 1$ nm and balanced charge distributions at 0 K.

The low-energy quasiparticle band dispersion of the two-layer graphene system is plotted in Fig. 4.9(a) as a function of interlayer separation d, for effective dielectric constant $\varepsilon_r = 2.2$ and $\Delta = 0.5$ eV. As d increases, the exchange interaction becomes weak and the band-structure approaches that of the uncoupled system. The nearly exponential dependence of band gap, a measure of the strength of the condensate, on layer separation is evident from the semilog plot in Fig. 4.9(b), where we plot the band gap at $T = 0$ K and $\Delta = 0.5$ eV for two additional dielectric constant values. This strong dependence on the interaction strength, controlled by d, has the same origin as the familiar strong dependence on weak interactions in the qualitative McMillan formula for the critical temperatures of superconductors.

In Figs 4.8, 4.9(b) and 4.10 we plot the condensate band gap as a function of ε_r for graphene layers separated by 1 nm, at $\Delta = 0.5$ eV and $T = 0$ K and $T = 300$ K. These figures exhibit the weakening of the condensate with increasing ε_r and the corresponding decrease in the Coulomb interaction between the two layers. Here we note that ε_r of 2.2 is essentially that used in original work of Ref. [56] and is close to that speculated for graphene on SiO_2 in air [72], or it can be thought of as that of a low-κ material like BN [73]. ε_r=3.0 corresponds to a low-κ dielectric like C-doped SiO_2 [74], $\varepsilon_r = 3.9$ corresponds to SiO_2 and $\varepsilon_r = 9.1$ to a high-κ dielectric like Al_2O_3.

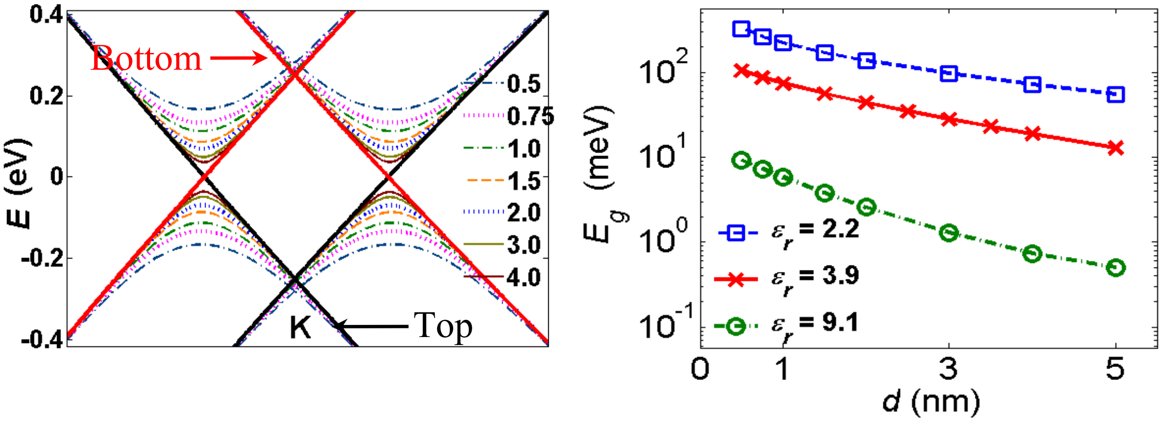

Figure 4.9. Left (a). Low-energy dispersion of the graphene bilayer system with $\Delta = 0.5$ eV and $\varepsilon_r = 2.2$ at 0 K, and balanced charge distributions, as a function of layer separation d (legend entries are in nm). The labeled solid lines (black and red online, respectively) are the band structures of the top and bottom graphene layers in absence of an exchange coupling between the layers. Right (b) Band gap E_g in the correlated condensate state for three different dielectrics, showing exponential scaling of the band gap with layer separation, at 0 K with $\Delta = 0.5$ eV and balanced charge distributions.

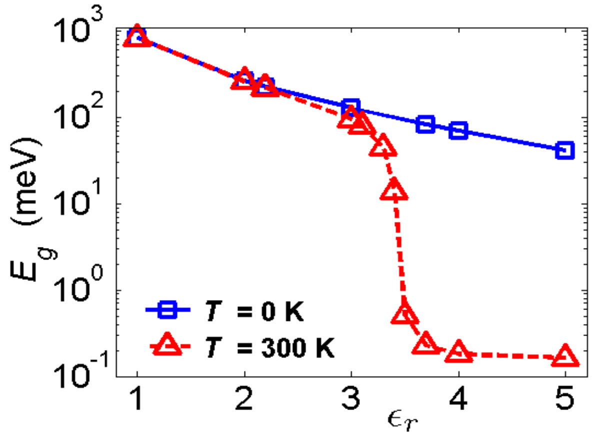

Figure 4.10. Band gap for two graphene layers with $\Delta = 0.5$ eV, $d = 1$ nm, and balanced charged distributions at 0 K and 300 K, as a function of the dielectric constant. The minimum values are limited by the accuracy of the calculation.

We note that the overall strength of the condensate is more sensitive to changes in ε_r than d, as further exhibited in Fig. 4.11 where the band gap is plotted vs. both ε_r and d. For example, the gap widens by a factor of about 3.9 when ε_r decreases from 4 to 2, but only by a factor of about 1.6 when d decreases from 2 nm to 1 nm. For the non-local exchange potential $V_{\mathrm{HF}}(\mathbf{R_T},\mathbf{R_B})$ defined in Eq. 4.4, the underlying Coulomb interaction varies with $\varepsilon_{\mathrm{r}}^{-1}$ for all values of ΔR, but as d^{-1} only for $\Delta R = 0$.

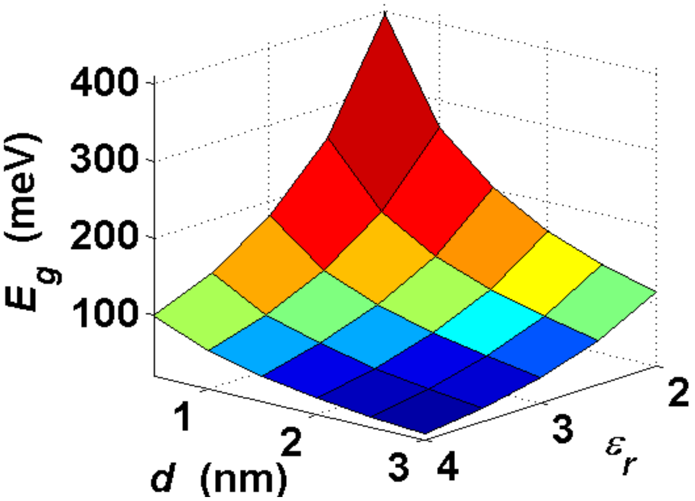

Figure 4.11. Band gap E_{g} for the bilayer condensate with $\Delta = 0.5$ eV and balanced charged distributions at 0 K, as a function of the interlayer dielectric constant ε_{r} and layer separation d.

As in the theory of superconductivity, the mean-field theory condensate is destroyed by thermal energies k_BT on the order of the 0 K energy gap, E_{g0}. Specifically, for these otherwise decoupled graphene bilayers, the occupation probabilities $n_{\alpha,\mathbf{k},s}$ of the electronic states $\varphi_{\alpha,\mathbf{k},s}$ below the band gap that contribute most to $V_{\mathrm{HF}}(\mathbf{R_T},\mathbf{R_B})$ decrease with increasing temperature. In addition, the occupation of the states above the band gap increase in the same way, but the contributions to $V_{\mathrm{HF}}(\mathbf{R_T},\mathbf{R_B})$ for any occupied states $\varphi_{\alpha,\mathbf{k},s}$ above the band gap are precisely opposite that for the corresponding state $\varphi_{\alpha,\mathbf{k},s}$ below the band gap. Both contributions, thus, weaken $V_{\mathrm{HF}}(\mathbf{R_T},\mathbf{R_B})$ with increasing temperature. Furthermore, as the condensate weakens, the band gap shrinks producing a positive feedback and a rapid collapse in the self-consistently calculated condensate with increasing temperature. Fig. 4.12 shows the temperature dependence of the band gap for three different effective dielectric constants. The layer separation $d = 1$ nm and the potential difference $\Delta = 0.5$ eV in all cases. As expected, the lower the permittivity, the stronger the 0 K condensate, and the higher the temperature that can be tolerated. The insert in Fig. 4.12, where the data is scaled by E_{g0}, illustrates that the condensate decay is close to a universal function of $k_B T/E_{g0}$ as expected for these balanced charge distributions, with collapse with temperature by $k_B T/E_{g0} \approx 0.25$, or $E_{g0} \approx 4k_B T$. Any parameter change that alters the $E_{g0}/k_B T$ ratio is expected to produce a similar effect, as per the collapse of the condensate shown in Fig. 4.10 at a fixed temperature of 300 K as a function of dielectric permittivity when as E_{g0} approaches 100 mV ($k_B \cdot 300$ K = 25.9 mV).

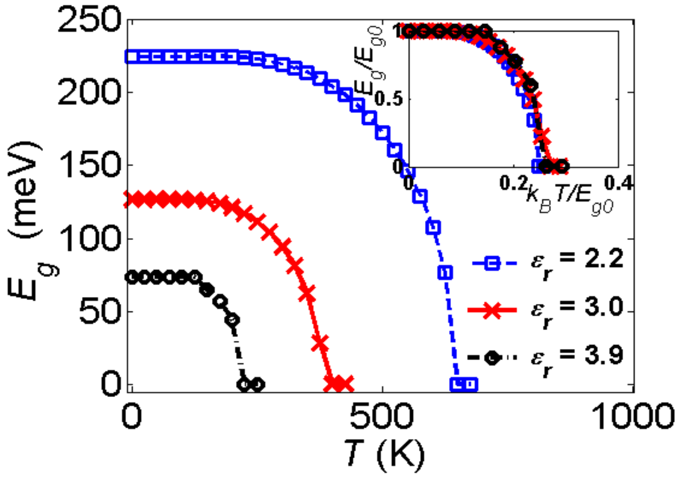

Figure 4.12. Temperature dependence of the band gap for three different dielectric constants with $\Delta = 0.5$ eV, $d = 1$ nm and balanced charge distributions. Lower ε_r result in larger coupling strength and therefore larger 0 K band gaps that are, therefore, also more robust at higher temperatures. The top right insert shows the same data scaled by 0 K band gap (E_{g0}), to illustrate the similarity of the T dependence of band gap for different ε_r.

Mean-field theory accounts for condensate suppression due to fermionic entropy at finite temperatures, but does not account for thermal fluctuations of the condensate spatial distribution. The latter effect dominates at very large values of E_{g0}, as explained in [56], but because of the condensate's substantial phase stiffness, is expected to produce relatively small changes in critical temperature T_c at the coupling strengths that can be reached experimentally.

4.3.3 Gate control: effect of charge imbalance

Understanding the sensitivity of the condensate to charge imbalance may be critical to designing and interpreting experiments to observe the condensate. And gate control of the condensate through its dependence on electron-hole charge imbalance provides the switching mechanism imagined in the proposed BiSFET device. Under equilibrium conditions, a charge imbalance corresponds to a shift in the Fermi energy either up or down away from the middle of the condensate's band gap. In particular, lowering the Fermi level corresponds to decreasing the electron concentration in the upper graphene layer and increasing the hole concentration in the lower layer in these simulations. The associated reduction in occupation probabilities $n_{\alpha,\mathbf{k},s}$ of the states $\varphi_{\alpha,\mathbf{k},s}$ is most pronounced for those states of the correlated system nearest to the band edge, which again are those which contribute most strongly to $V_{\mathrm{HF}}(\mathbf{R_T},\mathbf{R_B})$. Thus, the condensate is weakened and the band gap shrinks. For these unbalanced cases, the location of the Fermi level must be self-consistently calculated, along with changes in $V_{\mathrm{HF}}(\mathbf{R_T},\mathbf{R_B})$, to maintain a fixed degree of charge imbalance as would be imposed by external gating. We note that shifting the Fermi level up, corresponding to increasing the electron concentration and reducing the hole concentration, has an identical effect since the contributions of occupied states $\varphi_{\alpha,\mathbf{k},s}$ above the band gap to $V_{\mathrm{HF}}(\mathbf{R_T},\mathbf{R_B})$ precisely cancel out the contributions of those of their counterparts $\varphi_{\alpha,\mathbf{k},s}$ below the band gap, as previously noted.

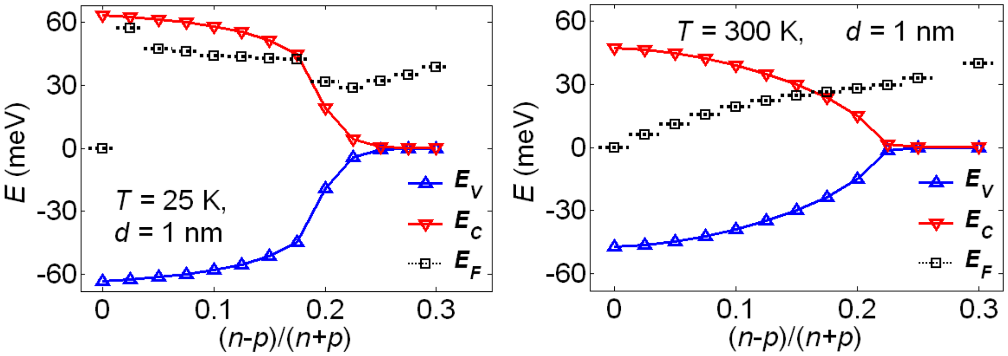

Figure 4.13. Energy band edges and Fermi level as a function of carrier imbalance between top layer electron density and bottom layer hole density for graphene bilayers separated by 1 nm at 25 K and 300 K with $\varepsilon_r = 3$ and Δ = 0.5 eV.

Self-consistently calculated band edges and relative E_F positions as a function of the charge imbalance between the top electron (n) layer and bottom hole (p) layer, here defined as $(n–p)/(n+p)$, for the graphene bilayers separated by 1 nm of ε_r = 3 low-κ material at 25 K and 300 K are shown in Fig 4.13. The same is shown for bilayers separated by 1.3 nm under otherwise identical conditions in Fig. 4.14. (We use 25 K here because, with the Fermi level now varying self-consistently with the band gap, the solutions become increasingly difficult to converge with decreasing temperatures.) We find that the condensate can be eliminated by charge balances of 25% or less in these simulations. And it can be substantially weakened at 300 K with charge variations of around 10%, which is all that would be required for the proposed BiSFET. Furthermore, though we have considered only a small region of the design space here, it appears that the weaker the initial condensate, the more sensitive it is to charge imbalance. Thus, from an applications point of view, the strongest condensate is not necessarily the best condensate.

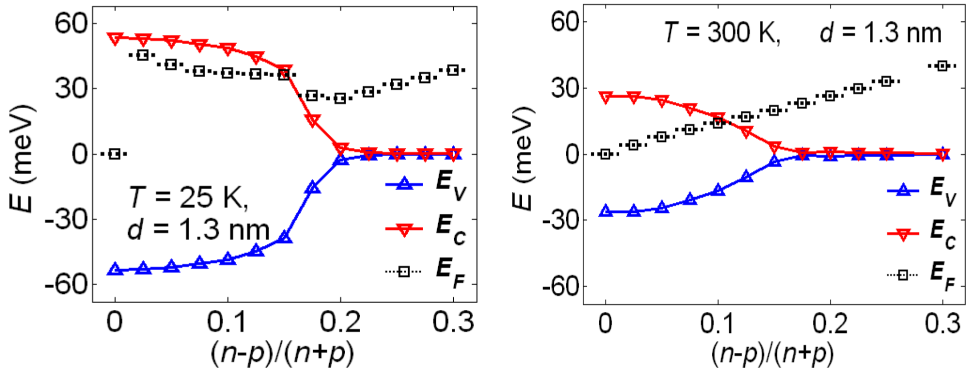

Figure 4.14. Energy band edges and Fermi level as a function of carrier imbalance between top layer electron density and bottom layer hole density for graphene bilayers separated by 1.3 nm at 25 K and 300 K with $\varepsilon_r = 3$ and $\Delta = 0.5$ eV.

4.3.4 Critical current

When single-particle interlayer coupling is neglected entirely, the total electronic energy E_{tot} in the presence of the nearly “spontaneously formed” condensate remains independent of the global interlayer phase difference between the layers, ω. However, interlayer coherence is never truly spontaneous, but rather is influenced by other processes such as single-particle tunneling between layers which introduce an ω-dependence to E_{tot}. This feature of bilayer exciton condensate physics plays an essential role because it leads to dramatically enhanced inter-layer currents up to a critical value [65, 66, 69]. When the interlayer phase stiffness is large, the critical current is given by the maximum value of the collective interlayer current [75]:

$$I_c = e/2\hbar \quad \partial E_{\text{tot}}/\partial\omega \;, \tag{4.8}$$

When the layer degree-of-freedom in a bilayer is viewed as a pseudospin, Eqn. (4.8) can be viewed as a Landau-Liftshitz equation for the time-derivative of the pseudospin component which measures layer polarization. An interesting aspect of graphene bilayer condensate physics is that the collective current is sensitive to the details of the single particle interlayer coupling. In this section we illustrate this dependence by performing perturbative calculations for the weak Bernal-like and hexagonal-like bare interlayer coupling arrangements. In the next chapter we will explore in detail how the form of the exchange potential gets altered due to the nature and strength of the bare tunneling.

To estimate the critical current here, we treat the bare interlayer coupling as a weak perturbation. The principal contribution to the total electronic energy E_{tot} is that due to the interlayer mean-field exchange interaction. However, as noted before, this exchange interaction does not actually establish a preferred value for the phase difference ω between the layers, i.e., the condensate properties of the otherwise uncoupled layers remain the same if the phases of the self-consistent wave-functions are uniformly modified by a phase factor $e^{i\omega}$ in one layer. Therefore, the global interlayer phase (ω) dependence of the total electronic energy E_{tot} (Eqn. (4.8)) reduces to the ω-dependence of the expectation value of the corresponding single-particle coupling Hamiltonian contribution, V_{bare}, here calculated to first order in terms of the wave-functions of the unperturbed condensate state. This expectation value is,

$$\left\langle V_{\text{bare}} \right\rangle = \sum_{\alpha,\mathbf{k},s} \Delta_{\mathbf{k}} / A_{BZ} \; n_{\alpha,\mathbf{k},s} \left\langle \varphi_{a,\mathbf{k},s} \,|\, V_{\text{bare}} \,|\, \varphi_{a,\mathbf{k},s} \right\rangle, \qquad 4.9$$

where $\Delta_{\mathbf{k}}$ is the $\mathbf{k}$-space area associated with each $\mathbf{k}$-point, and A_{BZ} is the Brillouin zone (BZ) area. The wave-functions have been normalized so that $\sum_{\alpha,\mathbf{k},s} \Delta_{\mathbf{k}} / A_{BZ} \; n_{\alpha,\mathbf{k},s} \left\langle \varphi_{a,\mathbf{k},s} \,|\, \varphi_{a,\mathbf{k},s} \right\rangle = 4$ per primitive unit cell, consistent with filling the band structure up to the Dirac point on average. The critical current, I_c, the maximum steady-state current that can flow between the two condensates, can then be estimated from the maximum value of Eqn. (4.8), which now takes the form $I_c = e/2\hbar \;\; \partial E_{\text{tot}}/\partial\omega = e/2\hbar \;\; \partial\langle V_{\text{bare}}\rangle/\partial\omega$ here (where both spin and valley degeneracy have already been accounted for in the summations above).

In the geometry that is most commonly considered, the interlayer hopping would occur across a possibly amorphous dielectric. Epitaxial tunnel barriers, such as BN for example, could offer important advantages if the relative orientations of the graphene and BN layers could be controlled [76] as will become clear from the following discussion. Both the typical size of tunneling matrix elements and the degree to which they satisfy momentum conservation could vary widely. Here, for the purpose of illustration, we treat the bare tunneling as simply a parameter. Consider first bare interlayer coupling to be $V_{\text{bare}} = t_{\perp}$ for A_T and A_B atoms within the same bilayer primitive unit cell, and to be zero otherwise. For the condensate corresponding to 1 nm layer separation, a low-κ dielectric of $\varepsilon_r = 3.0$ and an interlayer potential of $\Delta = 0.5$ eV at 0 K, which produced a 127 meV band gap, we find (see Fig. 4.15) that the critical current is approximately ($t_{\perp}$/eV) × (1.8×10^{-3}) × $e/\hbar$ per primitive cell, or $t_{\perp}$ × 8.4 nA nm^{-2} meV^{-1}. (Expressed per nominal charge carrier per layer, electron or hole, the critical current is ($t_{\perp}$/meV) × 0.58 × $e/\hbar$.) For a $t_{\perp}$ of approximately 1 meV, this result is essentially that employed for modeling purposes for the BiSFET [14], although even 1.2 meV is beyond the perturbative limit for these calculations. However, if under the same conditions otherwise, we take $V_{\text{bare}} = t_{\perp}$ for a B_T-A_B Bernal-like coupling within the same primitive unit cell, the critical current essentially vanishes (drops by roughly two orders of magnitude or more depending on precise details of the layer alignments). The reason for these stark differences becomes clear upon noting that the values of Fock potentials $V'_{\text{HF}}(\mathbf{R_T},\mathbf{R_B})$ of Eqs. (4.4)—as illustrated by Figs. 4.5-4.6—at (or at least very close to) the origin, $R_B - R_T = 0$ are the values of the corresponding expectation values of V_{bare} of Eq. 4.9, to within a factor of $-t_{\perp}4\pi\varepsilon_0\varepsilon_r d/e^2$ and the phase factor ω. As can be seen from these figures, in this way, bare A_T-A_B coupling or bare B_T-B_B will couple strongly to the condensate. In contrast bare B_T-A_B or bare A_T-B_B coupling to the condensate essentially. And the hexagonal-like in-phase sum of equal A_T-A_B and B_T-B_B coupling, which is essentially orthogonal to the condensate that is self-optimized in an "anti-hexagonal" manner to maximize the exchange coupling between the conduction band of one layer and the valence band of the other as discussed previously, suffers the same fate. These stark differences demonstrate that, in this perturbative limit at least, critical currents will be sensitive not only to the thickness of the tunnel barrier but also to its detailed atomic structure and coupling to the graphene.

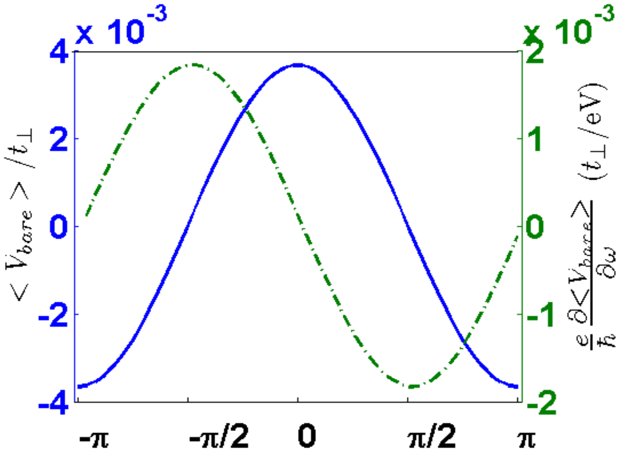

Figure 4.15. Expectation value of the interlayer tunneling $<V_{bare}>$ expressed in terms of the assumed bare interlayer tunneling $t_{\perp}$, as a function of the interlayer phase difference ω (left axis, blue solid curve). Right axis (green dotted curve) shows the critical current. Both results are for interlayer bare tunneling between only A_T and A_B carbon atoms. $<V_{bare}>$ as well as the critical current approaches zero for Bernal-like or hexagonal-like perturbative coupling

We emphasize that the above results were obtained in the perturbative limit when the bare coupling is quite weak and has little or no effect on the condensate itself, such as might occur in initial efforts to experimentally observe such a condensate. However, in the presence of more significant if still moderate bare A_T-B_B or B_T-A_B coupling for example, the energetically favorable solutions for the combined Hamiltonian could take on this latter character, which would have a profound effect on the corresponding critical currents.

4.4 CONCLUSION

The prediction of the possibility of spontaneous excitonic condensation in two oppositely charged graphene monolayers separated by a thin dielectric layer up to and above room temperature under suitable conditions [55, 56] prompted us to study the dependence of the strength of such condensates on various system parameters [77]. While we were mostly interested in the property of the "spontaneously formed" condensate, we report here on the critical current that can flow between the graphene layers as a function of the bare coupling, treating the bare tunneling as a perturbation. Even within such approach, the sensitivity of the critical current to the detailed nature of the interlayer coupling was apparent, leading us to explore its effect in greater detail in the following chapter.

Chapter 5: Effect of interlayer bare tunneling on electron-hole coherence in graphene bilayers

In the previous chapter, we attempted to throw light on the nature of the spontaneous excitonic condensation in the limit of weak interlayer bare tunneling such that it can be treated as a perturbation. However, such perturbative treatment holds for only extremely small values of bare tunneling, and typically for critical currents below what would be required for, e.g., effective BiSFET operation. Moreover, interlayer coherence, is never truly spontaneous, but rather is influenced by other processes such as single-particle tunneling between layers. To extend the knowledge of the behavior of the condensate in the presence of substantial bare single-particle tunneling, in this chapter we present self-consistent solutions of the condensate state in the presence of bare tunneling of varying strength and pattern of interlayer coupling among the atomic sublattices of the two graphene layers.

5.1 INTERLAYER BARE TUNNELING AS A TIGHT-BINDING PARAMETER

The model of the system essentially remains unchanged [Fig. 4.2] and as before, we consider here both the Bernal as well as hexagonal layer overlap [A_T above A_B, and B_T on top of B_B, see Fig. 4.2 (b)], as will be evident later. We modify the Schrodinger's equation, given in Eqn. (4.5) and (4.6) to include the bare tunneling as:

$$H_{\mathrm{TB}}\varphi_{\alpha,\mathbf{k},s}(\mathbf{R}_{\mathrm{T}}) - \Delta/2 \quad \varphi_{\alpha,\mathbf{k},s}(\mathbf{R}_{\mathrm{T}}) + \left[H_{\mathrm{tnnl},\mathbf{T}\to\mathbf{B}} + \sum_{\mathbf{R}_{\mathrm{B}}} V_{\mathrm{HF}}(\mathbf{R}_{\mathrm{T}},\mathbf{R}_{\mathrm{B}}) \right] \varphi_{\alpha,\mathbf{k},s}(\mathbf{R}_{\mathrm{B}}) = \varepsilon_{\alpha,\mathbf{k},s}\varphi_{\alpha,\mathbf{k},s}(\mathbf{R}_{\mathrm{T}}), \qquad 5.1$$

and

$$H_{\mathrm{TB}}\varphi_{\alpha,\mathbf{k},s}(\mathbf{R}_{\mathrm{B}}) + \Delta/2 \quad \varphi_{\alpha,\mathbf{k},s}(\mathbf{R}_{\mathrm{B}}) + \left[H^{\dagger}_{\mathrm{tnnl},\mathbf{T}\to\mathbf{B}} + \sum_{\mathbf{R}_{\mathrm{T}}} V_{\mathrm{HF}}(\mathbf{R}_{\mathrm{B}},\mathbf{R}_{\mathrm{T}}) \right] \varphi_{\alpha,\mathbf{k},s}(\mathbf{R}_{\mathrm{T}}) = \varepsilon_{\alpha,\vec{k},s}\varphi_{\alpha,\mathbf{k},s}(\mathbf{R}_{\mathrm{B}}) \qquad 5.2$$

for the top and bottom layers, respectively. Here, ε are the eigenenergies and H_{TB} is the nearest neighbor π-orbital (p_z-orbital for the assumed x-y oriented graphene planes) used before in Eqn. (4.6).

$H_{\mathrm{tnnl,T\to B}}$ is the top-to-bottom (signified by "T→B", not, to be confused with "TB" signifying "tight-binding") part of the bare single-particle tunneling Hamiltonian, and was not considered self-consistently earlier, though treated perturbatively (equivalent to V_{bare} in previous chapter). For bare interlayer coupling from $\mathrm{B_T}$ to $\mathrm{A_B}$ carbon atoms with Bernal-like stacking, e.g., $H_{\mathrm{tnnl,T\to B}}$ takes the form $H_{\mathrm{tnnl,T\to B}} = t_{\perp}\delta(\mathbf{R}_{\mathbf{A}_{\mathrm{B}}}, \mathbf{R}_{\mathrm{B_T}})$, where $\delta(\mathbf{R}_{\mathrm{A_B}}, \mathbf{R}_{\mathrm{B_T}})$ is the Kronecker delta functions in the discrete 2D coordinates **R,** and $t_{\perp}$ is the tunneling amplitude considered earlier. The bottom-to-top (B→T) part of the single-particle tunneling Hamiltonian would then be just the Hermitian adjoint/conjugate, $H_{\mathrm{tnnl,B\to T}} = t_{\perp}^{\dagger}\delta(\mathbf{R}_{\mathrm{B_T}}, \mathbf{R}_{\mathrm{A_B}}) = H_{\mathrm{tnnl,T\to B}}^{\dagger}$, although here we generally take $t_{\perp}$ as purely real.

5.2 SELF-CONSISTENT RESULTS AND DISCUSSION

In the geometry that is most commonly considered [14, 56], the interlayer hopping would occur across a dielectric, possibly amorphous. In general, the nature and type of the tunneling matrix elements could vary widely from system-to-system or even in the same system for amorphous dielectrics. We will consider a number of limiting cases here to tease out possible behaviors.

5.2.1 Quasi-Hexagonal Bare Coupling, $\mathrm{A_T}$-$\mathrm{A_B}$ and $\mathrm{B_T}$-$\mathrm{B_B}$

Here, for illustration we first consider real quasi-hexagonal single-particle bare coupling between the graphene layers, such that single-particle bare tunneling occurs between $\mathrm{A_T}$-$\mathrm{A_B}$ and $\mathrm{B_T}$-$\mathrm{B_B}$ atoms only. However, we vary the bare hopping parameter $t_{\perp}$ for each of these two interactions separately. Unless otherwise mentioned, for all calculations in this chapter we will consider the bilayer system separated by a low-κ dielectric of permittivity ε_r=3.0, and thickness d = 1nm, having a potential asymmetry of $\mp\Delta/2$, where Δ=0.5 eV. For reference, under balanced charge distribution, the band gap for this system at T=0 K, is 127 meV.

As shown in Fig. 5.1(a), for $t_{\perp,\mathrm{B_T}\text{-}\mathrm{B_B}} = t_{\perp,\mathrm{A_T}\text{-}\mathrm{A_B}} \neq 0$, the band gap of the system remains 127 meV, that of the condensate in the absence of coupling. In addition, as shown in Fig. 5.1(b), even with the coupling, the critical current remains essentially zero. It should be noted that such hexagonal-like bare coupling also would not provide conduction-band to valence-band coupling between the two graphene layers in the absence of the condensate; the overlap between conduction and valence band states of the same wavevector **k** with respect to such in-phase hexagonal coupling would be identically zero.

In contrast, along the perpendicular "direction" to the above in $t_{\perp,\mathrm{B_T}\text{-}\mathrm{B_B}} - t_{\perp,\mathrm{A_T}\text{-}\mathrm{A_B}}$ space, i.e., $t_{\perp,\mathrm{B_T}\text{-}\mathrm{B_B}} = -t_{\perp,\mathrm{A_T}\text{-}\mathrm{A_B}} \neq 0$, there is a substantial increase of band-gap with the magnitude of $t_\perp$, with the band gap reaching 163 meV for $t_{\perp,\mathrm{B_T}\text{-}\mathrm{B_B}} = -t_{\perp,\mathrm{A_T}\text{-}\mathrm{A_B}} = 7.5\,\mathrm{meV}$. Along this direction, the phase-correlation relationship established among the sublattices of the two graphene layers by the bare tunneling alone is precisely the anti-hexagonal phase relation between the wavefunctions on A and B sublattices that maximizes the exchange interaction for the spontaneous condensate. Indeed, when considering all possible combinations of $t_{\perp,\mathrm{A_T}\text{-}\mathrm{A_B}}$ and $t_{\perp,\mathrm{B_T}\text{-}\mathrm{B_B}}$ coupling, it is only variations in the interlayer coupling in this $t_{\perp,\mathrm{B_T}\text{-}\mathrm{B_B}} = -t_{\perp,\mathrm{A_T}\text{-}\mathrm{A_B}}$ direction that substantially affects the band gap, as also seen in Fig. 5.1(a). Furthermore, the interaction between the condensate and the bare tunneling is synergistic. The 36 meV increase of self-consistently obtained band gap for $t_{\perp,\mathrm{B_T}\text{-}\mathrm{B_B}} = -t_{\perp,\mathrm{A_T}\text{-}\mathrm{A_B}} = 7.5$ meV substantially exceeding the band gap produced by the bare tunneling alone (neglecting the exchange interaction), which is nearly equal to $\left|t_{\perp,\mathrm{B_T}\text{-}\mathrm{B_B}} - t_{\perp,\mathrm{A_T}\text{-}\mathrm{A_B}}\right|$, or 15 meV in this case. The coupling of the bare tunneling to the condensate is also evident from the substantial critical current I_c reaching approximately 193 nA/nm^2 in these calculations for $t_{\perp,\mathrm{B_T\text{-}B_B}} = -t_{\perp,\mathrm{A_T\text{-}A_B}} = 7.5$ meV. Another way of viewing these results is that the band gap and critical current are an approximately uniform function of the band gap produced by the bare coupling alone, even if the latter depends critically on the relative values of $t_{\perp,\mathrm{A_T\text{-}A_B}}$ and $t_{\perp,\mathrm{B_T\text{-}B_B}}$.

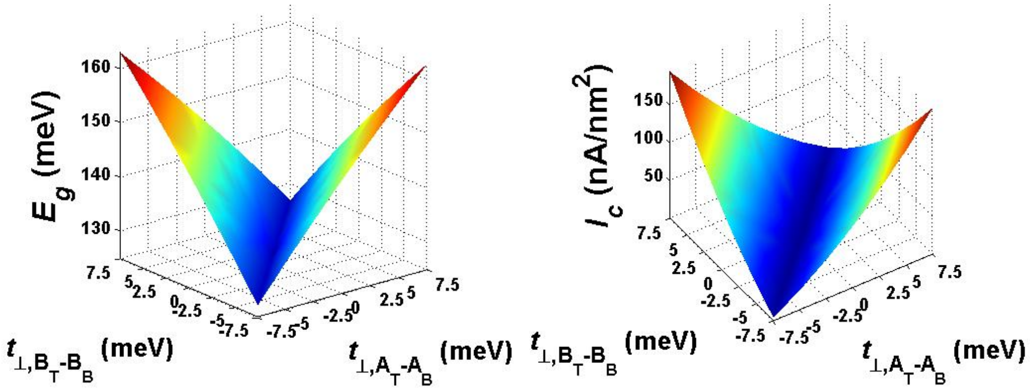

Figure 5.1. Surface plots showing on left the band gap (in meV) and on right the critical current density (I_c) variation for a graphene bilayer with weak coupling between $\mathrm{A_T}$-$\mathrm{A_B}$ and $\mathrm{B_T}$-$\mathrm{B_B}$ carbon atoms. For a given magnitude of bare tunneling, the maximum band gap (and I_c) occur when $t_{\perp\mathrm{BB}} = -t_{\perp\mathrm{AA}}$, since that is the phase relationship established between the graphene sublattices to maximize the exchange interaction in the limit of the "spontaneous condensate" ($t_{\perp\mathrm{BB}} = -t_{\perp\mathrm{AA}} = 0$).

5.2.2 Bernal-like, Hexagonal and "Half-Hexagonal" Coupling

Considering for example, with a Boron Nitride (BN) interlayer dielectric [76], crystalographically aligned for the sake of argument, with differing layer thickness and differing surface atoms types, one could imagine a qualitatively Bernal-like $\mathrm{A_T}$-$\mathrm{B_B}$ or $\mathrm{B_T}$-$\mathrm{A_B}$ coupling, or a "half-hexagonal" $\mathrm{A_T}$-$\mathrm{A_B}$ *or* $\mathrm{B_T}$-$\mathrm{B_T}$ coupling (in addition to effectively non-local bare coupling that we shall not explicitly consider here). The latter also represents an intermediate sub-case of the coupling considered in subsection (A) above, but we shall expand on it here.

The self-consistently calculated band gap and critical currents are shown in Figs. 5.2 and 5.3 respectively, for both for A_T-A_B bare coupling only and for B_T-A_B bare coupling only. The sum of the band gap of the spontaneous condensate produced by the exchange interaction alone and that of the band gap produced by bare-coupling alone, where the latter is again approximately equal to the bare coupling potential $t_\perp$ in both cases, is also shown in Fig. 5.2 for reference. Note that the bare local B_T-A_B coupling is orthogonal to exchange interaction of the spontaneous condensate which essentially vanishes at $\mathbf{R}_T = \mathbf{R}_B$ (The latter is also asymmetric and, thus, would still be orthogonal to any non-local A_T-A_B coupling that is symmetric in $\mathbf{R}_T - \mathbf{R}_B$). Accordingly, for smaller values of $t_\perp$, the critical current I_c is relatively very limited for B_T-A_B bare coupling. However, in the approximately 5 to 7.5 meV range, a transition occurs, above which the I_c approaches if not quite reaches that for A_T-A_B bare coupling of the same strength. As the gap produced by bare B_T-A_B coupling is again approximately equal to the bare coupling potential itself, this result means that above this transition the critical current approaches if not quite reaches the same functional dependence on the gap produced by bare coupling alone here as for anti-hexagonal coupling. At the same time, the self-consistently calculated band gap actually decreases, initially falling below that of the spontaneous condensate alone, although it then begins to increase again, eventually exceeding the result for sum of the exchange only and bare coupling only results. As can be seen in Fig. 5.4, this transition is associated with a significant change in the nature of the condensate itself. Comparing the exchange potentials of Fig. 5.4 for $t_\perp$=0 to the result for B_T-A_B coupling, with $t_\perp$=5.0 meV one can see that the bare coupling has established a definite phase relation ω between the layers as the first required step to allow a critical current, as evident in shifts between the real and imaginary components of the exchange interactions. In addition, there are quantitative changes apparent in the size and shape of the A_T-B_B and B_T-A_B exchange potentials. However, the exchange interactions still remain nearly orthogonal to the B_T-A_B interaction. By the time $t_\perp$ reaches 7.5 meV, however, the exchange potential has taken on the pattern and phase of the bare potential, being dominated by a strong B_T-A_B exchange interaction and a corresponding interlayer correlation in the wavefunctions. The chiral nature of graphene then forces destructive interference for the remaining exchange terms, reducing their contributions, much as discussed in Section 4.3.1for the spontaneous condensate.

From Fig. 5.5, we find that the critical current varies as the square of the bare tunneling amplitude $t_\perp$. This is true for the A_T-A_B hexagonal-like as well as for the Bernal tunneling at high enough values, such that it is well coupled to the condensate. Indeed, for the A_T-A_B critical current, we find that for $t_\perp$ ranging up to 25 meV, the critical current follows the empirical relation, $0.3t_\perp + 8.58t_\perp^2$ for the system studied here. For comparison, the BiSFET design employs a maximum current in the range of 10 nA/nm^2. The bare tunneling value required to get such a critical current is nearly 2.5 meV. For larger $t_\perp$, significantly larger I_c is possible, though we realize that even in the ideal device, current will be limited by factors such as injection, finite-size effects and bias conditions.

Note that the effects of precisely hexagonal-like bare coupling with A_T-A_B and B_T-B_B coupling of equal strength and phase are not shown in Figs. 5.2 and 5.3. While Bernal-like B_T-A_B or A_T-B_B bare and/or exchange coupling can produce a strong conduction-to-valence band coupling, such hexagonal coupling produces no coupling between the conduction and valence bands. Therefore even large precisely hexagonal bare coupling cannot couple to the condensate which inherently requires a strong conduction-to-valence band interaction. Only to the extent that bare coupling is orthogonal to this hexagonal limit, will significant critical currents be possible, consistent with the results of Fig. 5.1 and confirmed for higher coupling strengths up to 100 meV.

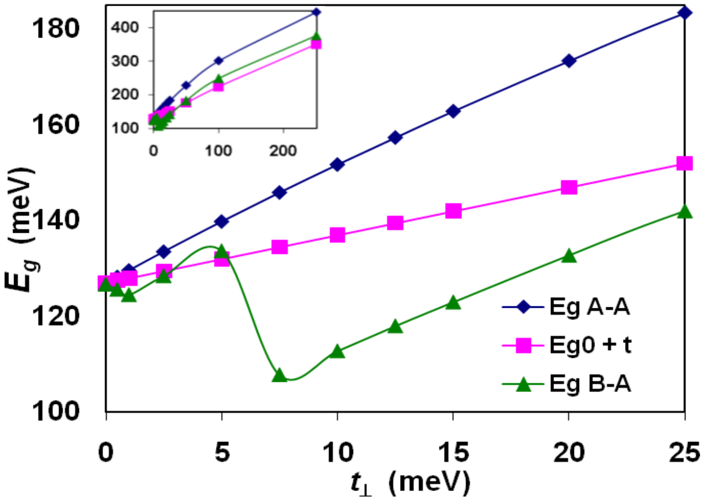

Figure 5.2. Self consistent band gap vs bare tunneling (both in meV) for two different cases of bare tunneling (A_T-A_B only and B_T-A_B only). Band gap for single particle bare tunneling only is shown in pink, scaled by the spontaneously formed (no tunneling) coherent state band gap, E_{g0} for comparison. Δ = 0.5 eV, d = 1 nm, ε_r = 3.0, and balanced charge distributions at 0 K are assumed.

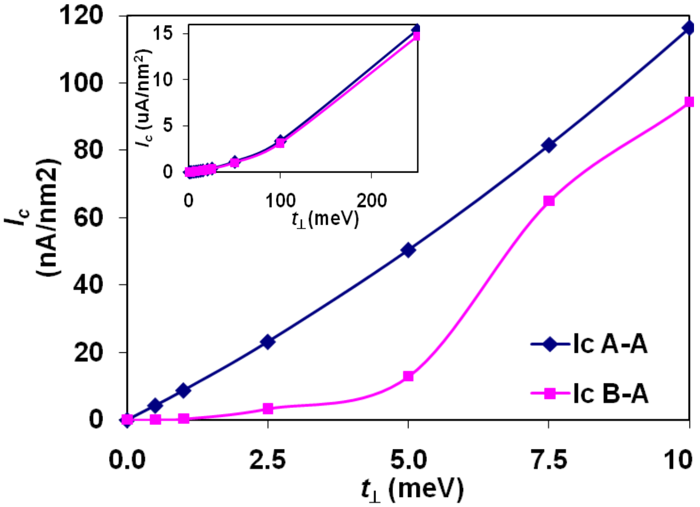

Figure 5.3. Critical current as a function of bare tunneling for A_T-A_B and B_T-A_B coupling. The dependence becomes identical for large $t_\perp$ (inset). Δ = 0.5 eV, d = 1 nm, ε_r = 3.0, and balanced charge distributions at 0 K are assumed.

B_T-A_B strength	$V'_{HF}(\mathbf{R}_T,\mathbf{R}_B)$ for A_T-A_B interaction	$V'_{HF}(\mathbf{R}_T,\mathbf{R}_B)$ for A_T-B_B interaction	$V'_{HF}(\mathbf{R}_T,\mathbf{R}_B)$ for B_T-A_B interaction
$t_\perp = 0.0$ meV	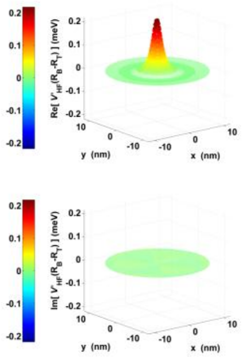	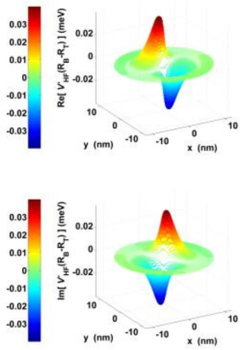	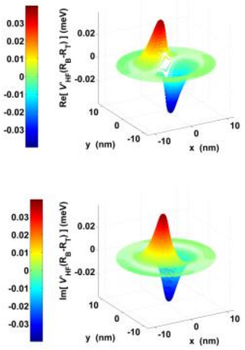
$t_\perp = 5.0$ meV	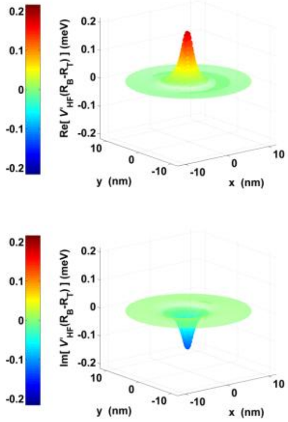	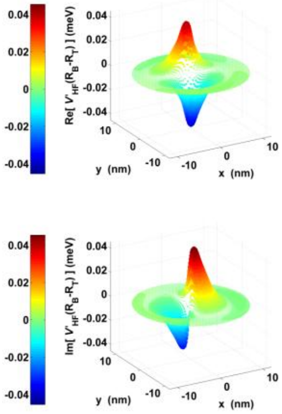	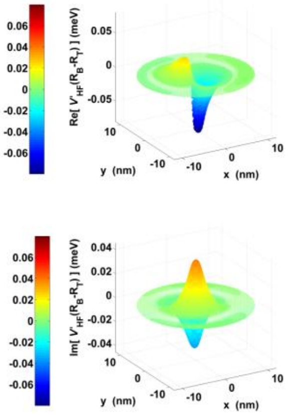
$t_\perp = 7.5$ meV	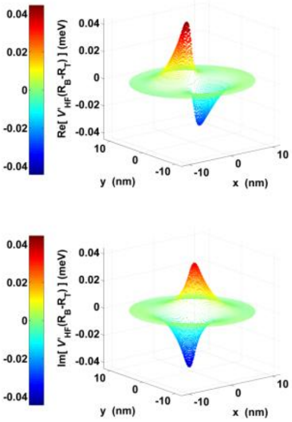	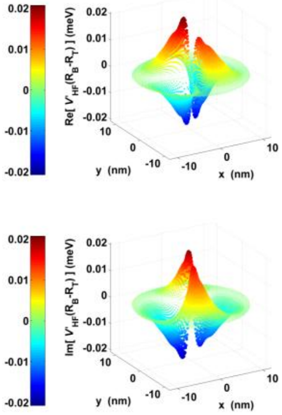	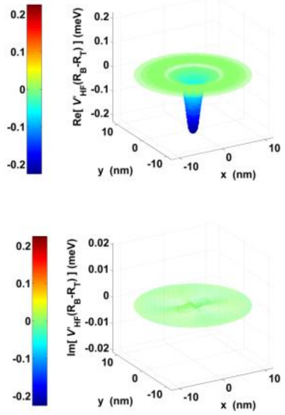

Figure 5.4. Self-consistent Fock exchange potentials $V'_{HF}(\mathbf{R}_T,\mathbf{R}_B)$ for graphene bilayers with a $t_\perp$bare tunneling between C atoms in Bernal (B_T-A_B) stacking for three different sublattice pair interactions, as a function of $\mathbf{R}_B - \mathbf{R}_T$. $\Delta = 0.5$ eV, $d = 1$ nm, $\varepsilon_r = 3.0$, and balanced charge distributions at 0 K are assumed.

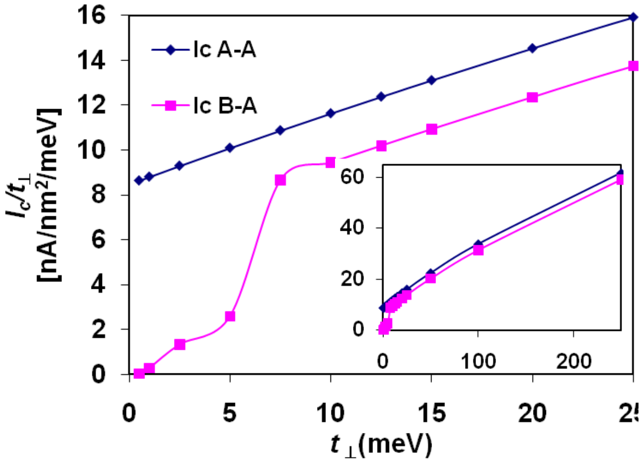

Figure 5.5. Critical current supported by the excitonic condensate scaled by the bare hopping potential strength $t_\perp$ as a function of $t_\perp$ for the hexagonal-like (A_T-A_B only) and bernal (B_T-A_B only) bare tunneling. For perturbative calculation, the critical current is directly proportional to $t_\perp$ for A_T-A_B tunneling, and is zero for B_T-A_B tunneling

The relationship of the bare tunneling pattern to that of the condensate, even for weak bare tunneling values, can also be observed in the temperature dependence of the condensate, as shown in Figs 5.6 and 5.7. Previously, independent of dielectric or layer separation, in the absence of bare coupling we found the collapse of the condensate band gap (E_g) with increasing temperature to be a universal function of temperature when both the band gap and the thermal energy (k_BT) were scaled by E_{g0}, where E_{g0} is the 0 K band gap, having the same form as the variation of the order parameter with temperature in any mean-field theory [78]. In these figures a significant and increasing stretch-out of the collapse of the condensate is seen for with A_T-A_B bare coupling and strong B_T-A_B coupling beyond the above described transition in the condensate. For weaker B_T-A_B coupling the collapse remains more abrupt, although even here it should be noted that there is a residual gap that exceeds that for the bare coupling alone (again approximately equal to the bare coupling potential itself).

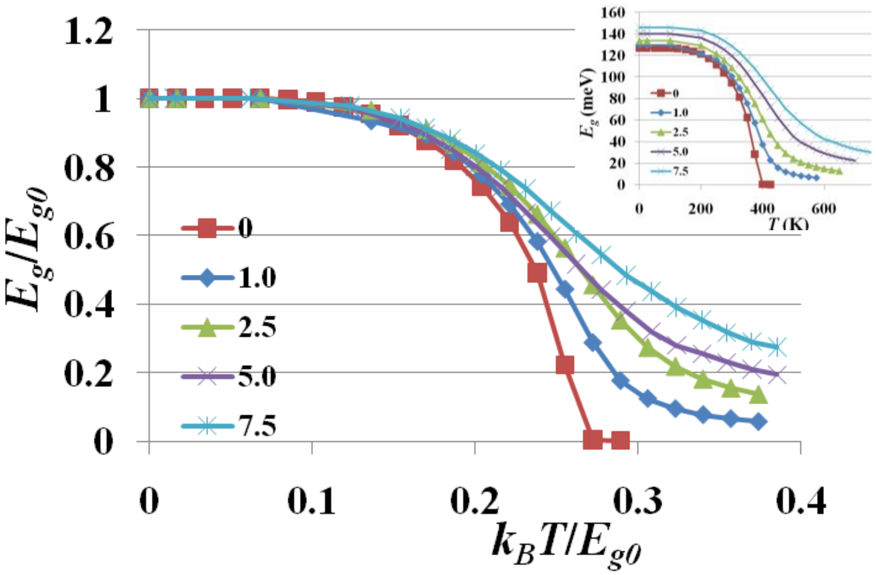

Figure 5.6. Temperature dependence of the band gap for three different bare tunneling values, zero, 1.0 meV and 2.5 meV, all having A_T-A_B tunneling only. ε_r = 3.0 with Δ = 0.5 eV, d = 1 nm and balanced charge distributions. Top right insert shows the same data scaled by 0 K band gap (E_{g0}).

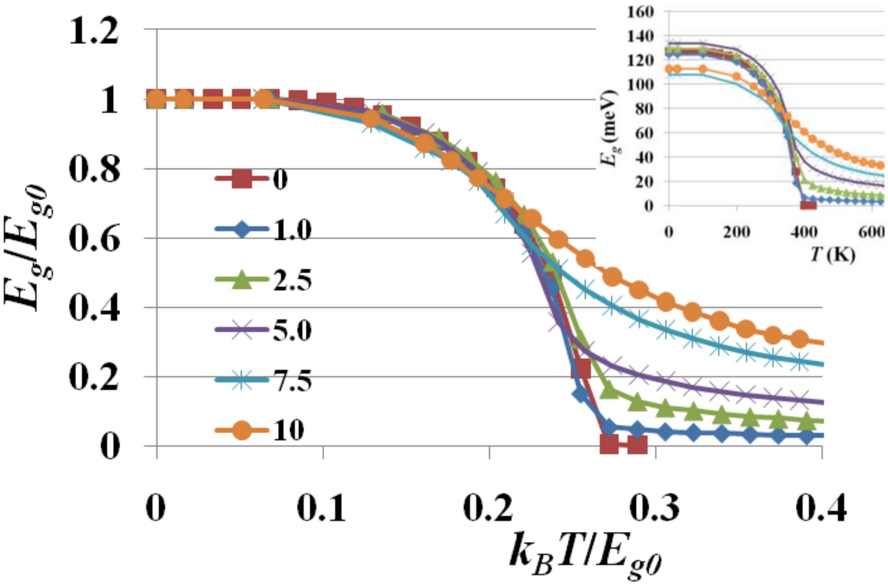

Figure 5.7. Temperature dependence of the band gap for three different bare tunneling values, zero, 1.0 meV and 2.5 meV, all having B_T-A_B tunneling only. ε_r = 3.0 with Δ = 0.5 eV, d = 1 nm and balanced charge distributions. Top right insert shows the same data scaled by 0 K band gap (E_{g0}).

5.2.3 Band gap, Critical current and Carrier Imbalance

We have noted before that the effects of carrier imbalance on the condensate strength and critical current in the presence of a bare coupling will no doubt be relevant to experimental attempts to observe the condensate, and would be necessary for the proposed BiSFET to function based on gate control of the condensate. For the spontaneous condensate at least, we found in the previous chapter that imbalance of the electrons and holes in the two layers reduces the exchange interaction leading to an eventual collapse of the condensate to the normal state.

As shown in Fig. 5.8, for better or worse A_T-A_B bare coupling makes the condensate more robust to charge imbalance, particularly large charge imbalance. Still as shown in Figs. 5.8 and 5.9, respectively, the calculated strength of the condensate as measured by the band gap and of the critical current, are monotonically and significantly decreasing functions of increasing charge imbalance at both the considered 25 K and 300 K temperatures for all of considered bare coupling strengths $t_\perp$ which ranged up to 15 meV (though we verified the trend up to $t_\perp$=25 meV).

In contrast, for B_T-A_B there can be more complicated behavior. For example, as shown in Fig. 5.10, at a temperature of 25 K the band gap actually becomes much more sensitive to charge imbalance for low bare coupling strengths, 0.5 and 1.0 meV in this case. At higher coupling strengths at 25 K and for all cases at 300 K, the condensate, however, again becomes more robust to large charge imbalances as for A_T-A_B. The critical current behavior shows it's own distinctive traits. For 5 meV or less of bare coupling, below the transition from spontaneous-condensate anti-hexagonal exchange coupling to the bare-coupling-induced Bernal-like exchange coupling for balanced charge distributions, the initial effect of charge imbalance is actually to increase the critical current. For 7.5 meV of bare coupling or more, above the transition, the critical current again decreases with charge imbalance, and monotonically at 300 K. This behavior for low B_T-A_B bare coupling can be associated with a shift in the pattern of the exchange potential of the spontaneous condensate with charge imbalance. As seen in Fig. 5.11, at T=25 K for 10% imbalance, the spontaneous condensate is no longer entirely orthogonal to the B_T-A_B bare coupling. Thus, charge imbalance gives the B_T-A_B bare coupling a moderate head start toward shifting the pattern of the condensate and the exchange interaction from anti-hexagonal to Bernal-like, with an attendant increase in the critical current and, e.g., earlier initial drop in the condensate band gap seen in Figs. 5.23 and 5.3.

5.3 CONCLUSION

In this work, we have extended the mean-field theory treatment of interlayer exchange interactions within our atomistic tight-binding model of two graphene monolayers. By considering representative limiting cases, we show how the relation of the pattern of bare coupling among the atomic sublattices to that of the "anti-hexagonal" pattern of the exchange interaction for the spontaneously formed condensate (A_T-A_B and B_T-B_B coupling of same strength and opposite phase, with other terms being small) determines the relation of the band gap and critical current to the bare coupling. For example, for patterns of bare coupling that couple well to the anti-hexagonal pattern of the spontaneous condensate, a substantial critical current is obtained—readily larger than the values required for the BiSFET—dependent on $\left|t_{\perp,\mathrm{A_T}\text{-}\mathrm{A_B}}-t_{\perp,\mathrm{B_T}\text{-}\mathrm{B_B}}\right|$. Bernal-like bare interlayer coupling (B_T-A_B or A_T-B_B), in contrast, is essentially orthogonal to the spontaneous exchange interaction and, thus, initially leads to very little critical current. However, by inducing a change in the condensate itself to a Bernal-like pattern, bare-coupling-dependent band gaps and critical currents as a function of bare interlayer coupling strength are then obtained that approach those for patterns of bare coupling that do couple well to the spontaneously formed condensate. In contrast, hexagonal bare coupling (A_T-A_B and B_T-B_B coupling of same strength and phase) does not couple well to either anti-hexagonal or Bernal-like forms of the condensate and exchange interaction. Nor is it possible to induce a shift in the condensate to a compatible hexagonal form, as such a hexagonal form is fundamentally incompatible with coupling between the conduction and valence bands of the respective graphene layers. Collectively, however, these results suggest that only patterns of bare coupling that can couple well to neither the anti-hexagonal pattern of the spontaneous condensate nor the inducible Bernal-like pattern will not be able to produce significant critical currents ultimately.

Regardless of the pattern of bare coupling, these results suggest that the critical current may eventual become a roughly universal function of the band gap produced by bare coupling alone, although this behavior may be delayed for more Bernal-like bare coupling and the band gap produced by bare coupling alone is strongly dependent on the detailed pattern of the bare interlayer coupling itself.

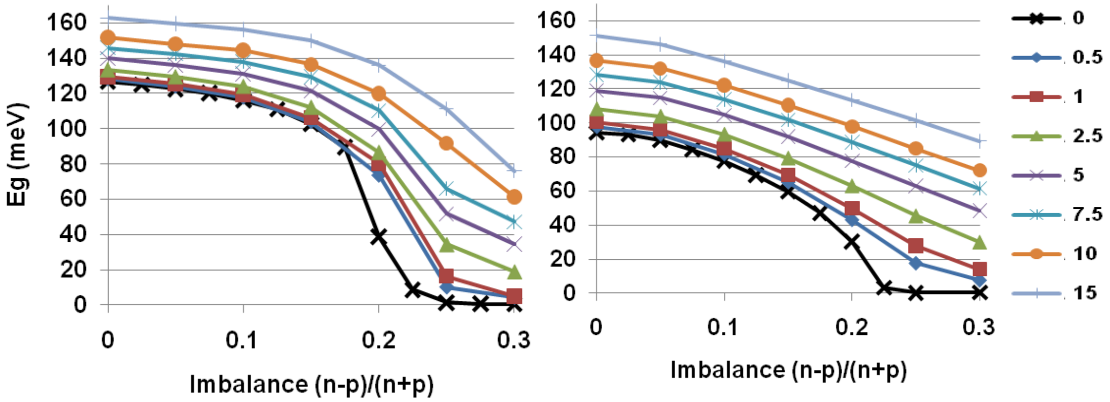

Figure 5.8. Self-consistent band gap as a function of imbalance for several different bare tunneling values for A_T-A_B coupling at T= 25 K (left) and 300 K (right). $\Delta = 0.5$ eV, $d = 1$ nm and $\varepsilon_r = 3.0$. The strength of the bare tunneling in meV is shown on the right. For comparison, the spontaneous condensate behavior ($t_\perp = 0$) is also shown.

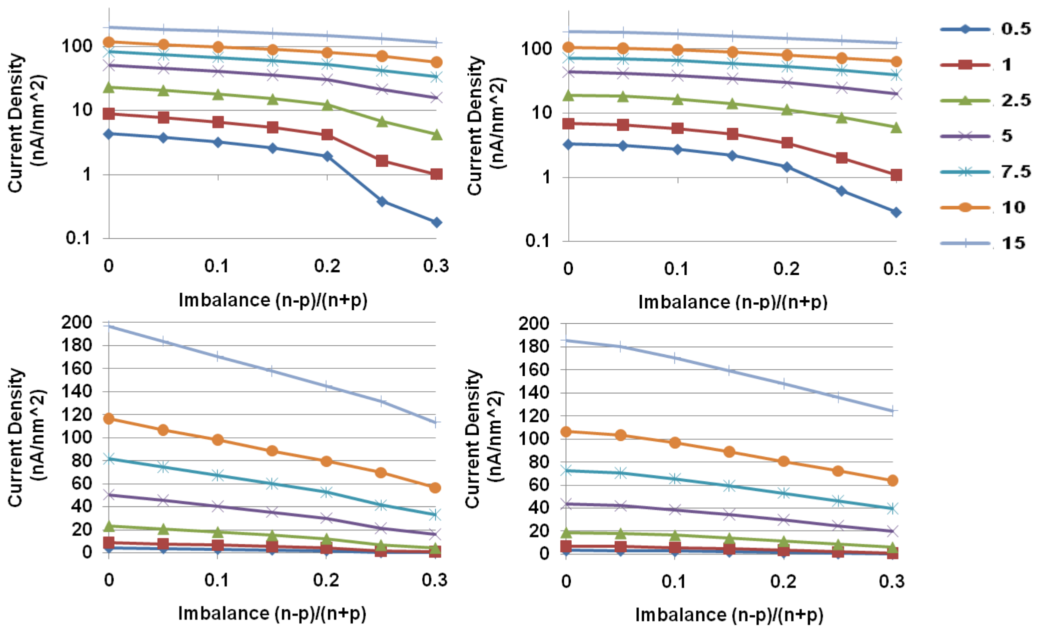

Figure 5.9. Self-consistently calculated critical current for graphene bilayers having an A_T-A_B bare coupling as a function of carrier imbalance between the layers for increasing values of bare tunneling, at T= 25 K (left) and 300 K (right). The current density is shown in linear scale in the bottom row and in logarithmic scale in the top row. $\Delta = 0.5$ eV, $d = 1$ nm, $\varepsilon_r = 3.0$.

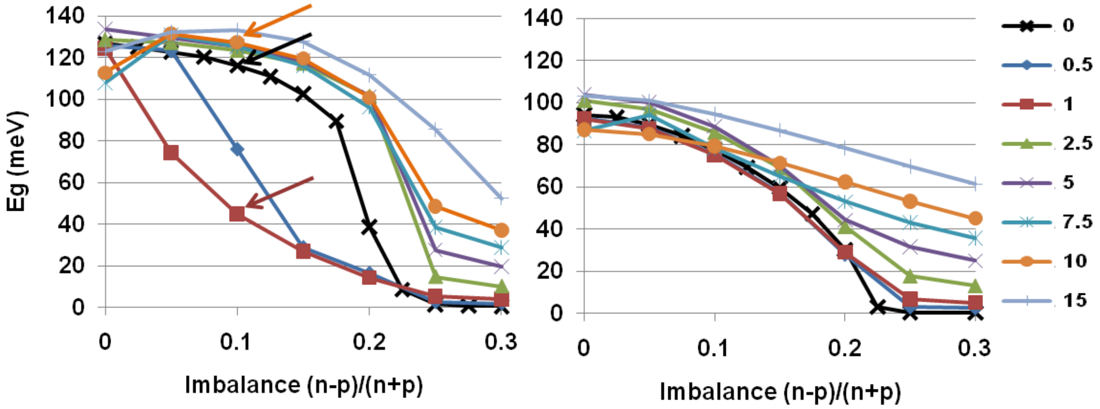

Figure 5.10. Self-consistent band gap as a function of imbalance for several different bare tunneling values for B_T-A_B coupling at T= 25 K (left) and 300 K (right). $\Delta = 0.5$ eV, $d = 1$ nm and $\varepsilon_r = 3.0$. The strength of the bare tunneling in meV is shown on the right. For comparison, the spontaneous condensate behavior ($t_\perp = 0$) is also shown. The arrows in the left figure (T=25 K) denote the cases, for which the exchange potentials have been drawn in Fig. 5.13 to explore the reason behind the variation obtained here.

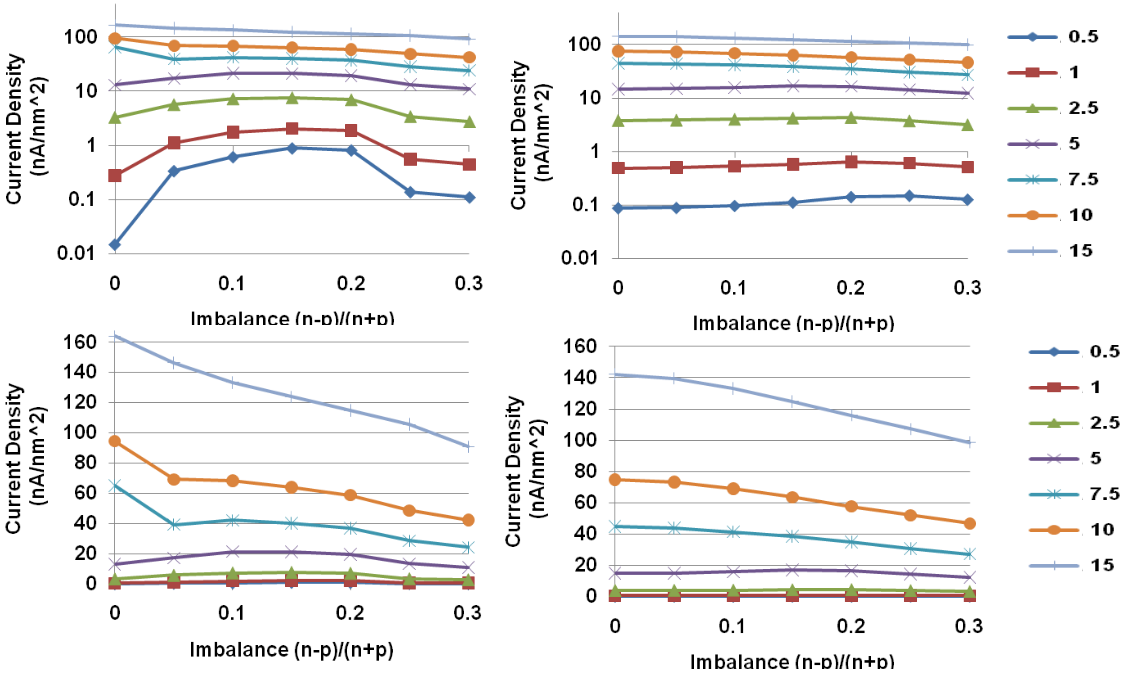

Figure 5.11. Self-consistently calculated critical current for graphene bilayers having a B_T-A_B bare coupling as a function of carrier imbalance between the layers for increasing values of bare tunneling, at T= 25 K (left) and 300 K (right). The current density is shown in logarithmic scale in the top row and in linear scale in the bottom row. $\Delta = 0.5$ eV, $d = 1$ nm, $\varepsilon_r = 3.0$.

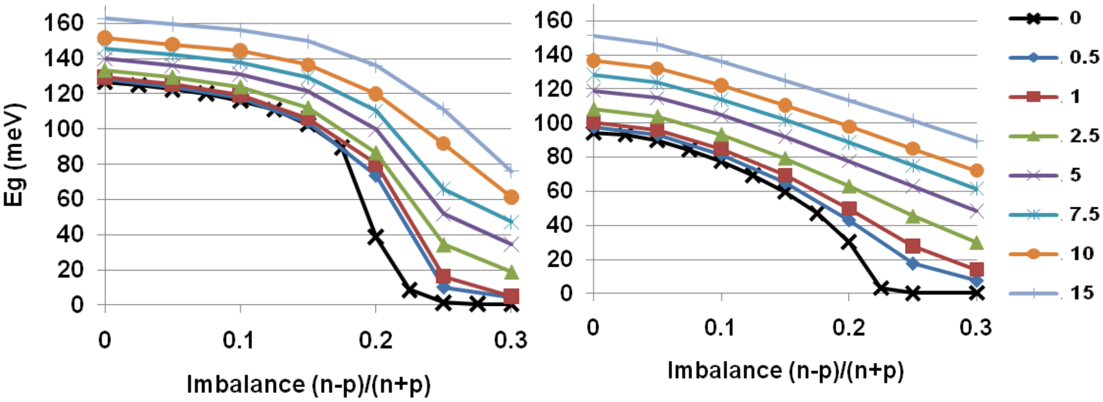

Figure 5.12. Self-consistent band gap as a function of imbalance for several different bare tunneling values for A_T-A_B coupling at T= 25 K (left) and 300 K (right). $\Delta = 0.5$ eV, $d = 1$ nm and $\varepsilon_r = 3.0$. The strength of the bare tunneling in meV is shown on the right. For comparison, the spontaneous condensate behavior ($t_\perp$=0) is also shown.

System Condition	$V'_{\mathrm{HF}}(\mathbf{R}_\mathrm{T},\mathbf{R}_\mathrm{B})$ for $\mathrm{A_T}$-$\mathrm{A_B}$ interaction	$V'_{\mathrm{HF}}(\mathbf{R}_\mathrm{T},\mathbf{R}_\mathrm{B})$ for $\mathrm{A_T}$-$\mathrm{B_B}$ interaction	$V'_{\mathrm{HF}}(\mathbf{R}_\mathrm{T},\mathbf{R}_\mathrm{B})$ for $\mathrm{B_T}$-$\mathrm{A_B}$ interaction
$t_\perp = 0.0$ meV, $\frac{n-p}{n+p} = 0.1$	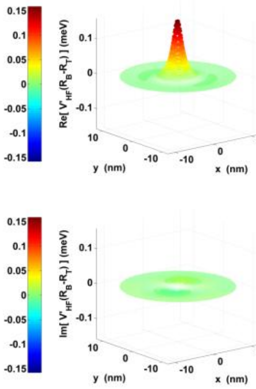	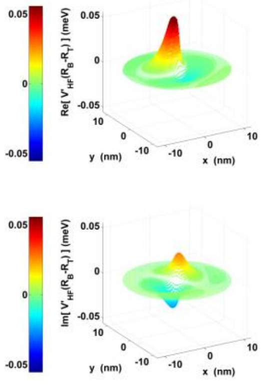	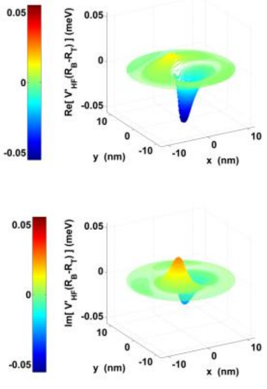
$t_\perp = 1.0$ meV between $\mathrm{B_T}$-$\mathrm{A_B}$ C atoms, $\frac{n-p}{n+p} = 0.1$	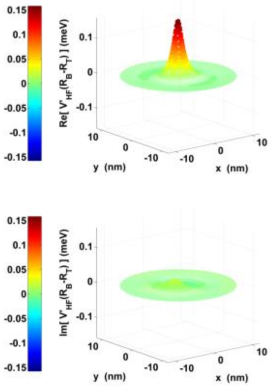	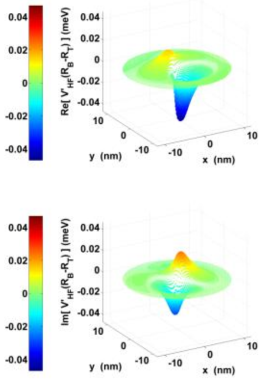	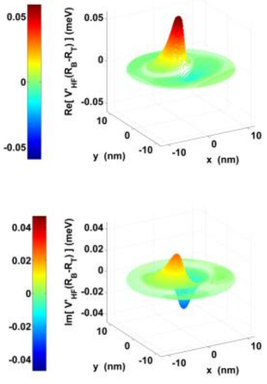
$t_\perp = 10.0$ meV between $\mathrm{B_T}$-$\mathrm{A_B}$ C atoms, $\frac{n-p}{n+p} = 0.1$	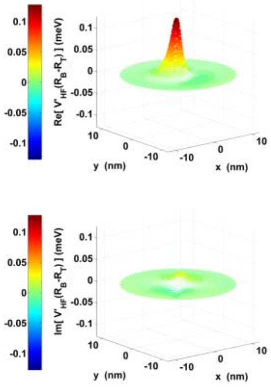	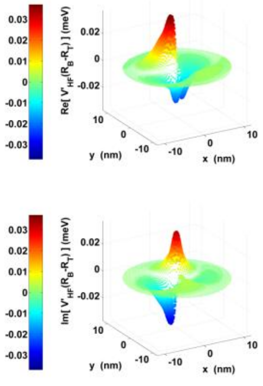	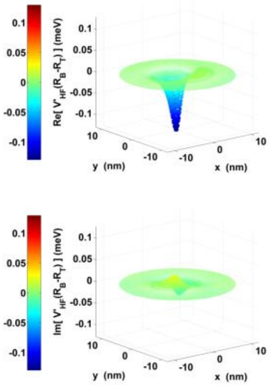

Figure 5.13. Self-consistent Fock exchange potentials $V'_{\mathrm{HF}}(\mathbf{R}_\mathrm{T},\mathbf{R}_\mathrm{B})$ for graphene bilayers showing the loss of symmetry due to carrier imbalance. $\Delta = 0.5$ eV, $d = 1$ nm, $\varepsilon_\mathrm{r} = 3.0$, and T= 25 K for these simulations.

Chapter 6: Conclusion

In this section, I provide a summary of work done in the course of the research program, and suggest avenues for future research.

6.1 SUMMARY

Back in 2005, when I started working on this program, silicon nanowire MOSFETs had already been demonstrated [79], and their advantages over planar MOS devices [80, 81], had caught the attention of the semiconductor industry [82]. I had just joined the modeling and simulation group here at UT and started looking at the effect of surface roughness on transport in tri-gate silicon-on-insulator (SOI) MOSFETs as part of getting familiar with non-equilibrium Green's function based transport. The importance of random dopant fluctuation (RDF) had started becoming important due to the small scale of such devices, and our surface roughness studies with random dopant distribution, gave us interesting results that were later published. (Note that based on this work on RDF in nanowire transistors, Micron Technologies, Inc. offered me an internship in summer 2008 at Boise, ID, where I looked at the dynamic random access memory (DRAM) process flow to identify the important process factors that cause extrinsic variations to electrical parameters of access transistors. Subsequently, I developed and demonstrated an efficient Response Surface Model to serve as a surrogate to the TCAD simulations for optimizing process conditions to reduce variation [83, 84].) However, the effective-mass framework which we were using for solving electron transport in these devices were clearly not sufficient for hole transport [85], because of the warped valence band structure. This prompted me to turn my attention towards the development of full-band quantum transport code.

Of the several different band structure calculation methods, I was keen to adapt the tight-binding method, as the discrete, atomistic nature of it appealed to me (having grown used to discretizing the effective mass Schrodinger equation to a pseudo-tight-binding form). The details of this development and the advantages of this method can be found in Chapter 2. The original intention was to use this tight binding full-band fully-3D quantum simulator to the study hole transport in silicon, Ge and III-V channel devices. However, the band structure that emerged from empirical tight binding method using five orbitals (sp^3s^*) only, as we were doing, while being reasonably accurate, and being optimum from the accuracy vs. computational load perspective [22], was inferior to models that employed more orbitals ($sp^3s^*d^5$) within the tight-binding framework to capture the richness and more detail of the band structure [86], or methods like k.p which are reported to reproduce the hole band structure to a greater accuracy [85]. However, since our five band model gave reasonably accurate results near the gamma point, we employed it to model conduction band-to-valence band tunneling in III-V materials like InSb nanowires. Details on this result as well as the method of calculation of the tight-binding transport are given in Chapter 2.

In the mean time, research in graphene had picked up significantly since the discovery of the mechanical exfoliation method in 2004 [12], and by early 2007, when I had nearly finished the development of my atomistic tight-binding transport code, the first field-effect device based on monolayer graphene had already been demonstrated [34]. I had already started work on graphene, and the fact that for graphene, a single π orbital per atom is sufficient to model the transport allowed me to continue to use my program to simulate large devices on personal workstations instead of employing supercomputers. As I comment in Chapter 3, initial simulation studies of ideal armchair-edge graphene-channel MOSFETs reported extremely good device performance. Later studies that employing a full-band model [37] (as compared to the effective mass treatment in [35]), also predicted excellent device characteristics, but as before considering ideal edge graphene nanoribbons. This prompted us to investigate the effects of non-ideal edges on the transport in graphene nanoribbons, as well as the effect of such roughness on device performance when these ribbons are used as the channel in MOSFETs. We used a simple correlation index to model the degree of roughness in the channel, and the 'atomistic' nature of the full-band model helped us to easily treat the effect of vacant sites along the armchair edges giving rise to irregular edges, which, as we found, have a profound deleterious effect on the transport. For the same degree of roughness, the effect was more severe as the channel width was reduced, and we concluded that smooth ideal nanoribbons were key to achieving a high ON/OFF current ratios and device-to-device reproducibility as required to employ these graphene devices for logic. Chapter 3 discusses these details.

Following the prediction of excitonic condensation of electrons and holes in graphene bilayers that could possibly survive at room temperatures and higher, my advisors working with Prof.s MacDonald and Tutuc had proposed to utilize the enhanced interlayer tunneling possible in such a condensate state to design a low-power, yet fast logic device, the BiSFET [14]. After coming back from my above mentioned 2008 summer internship, I initially did preliminary single-particle calculations for tunneling transport in a graphene bilayer, where we mimicked the enhanced coupling in the condensate state empirically by treating the interlayer hopping between the Bernal-stacked carbon atoms as a parameter that was varied to observe its effect on tunneling transmission [87]. Subsequently, I concentrated my efforts on simulating the equilibrium bulk graphene bilayer system with the exchange potentials calculated on the real-space tight-binding π-orbital basis, so that the self-consistent potentials obtained at the end can be put into use later to improve our effective single-particle picture. In the process, we explored the effect of various system parameters including carrier density, dielectric permittivity and thickness, and temperature on the strength of the condensate. The results of these are detailed in Chapter 4. We also studied the effect of charge distribution imbalance, which is the mechanism of condensate control in the BiSFET proposal, and in the limit of very weak to zero bare tunneling, we found that the condensate does weaken with increasing charge imbalance, and eventually collapses to the normal state.

The enhanced interlayer tunneling current, which the device proposals on the condensate attempt to exploit, require a finite, even if weak, bare tunneling to survive. Therefore in the limit of weak bare tunneling, I explored the critical current supported by the condensate state, and these results are given in the final sections of Chapter 4. I found that, in this perturbative limit, while the critical current is proportional to the bare tunneling in the case of A-A bare tunneling only, it goes to zero in both the Bernal (A-B) or hexagonal (A-A and equal B-B only) cases. However, the ranges of bare tunneling that were allowed in the perturbative treatment being extremely small (typically less than 1 meV, though the exact values depend on the system parameters chosen). We next attempted to self-consistently include the bare tunneling within the Hamiltonian, and calculate primarily the band gap, which measures the strength of the condensate, and the critical current, which is the key design parameter for device applications of the condensate. These calculations, reported in detail in Chapter 5, reveal the sensitivity of the condensate to the detailed nature as well as strength of the bare tunneling. I found that if the bare interlayer coupling couples well to the spontaneous condensate obtained in the absence of coupling, e.g., A-A coupling only, the condensate is strengthened by the presence of bare tunneling, and the critical currents are enhanced, as shown in Chapter 5. On the other hand, I found that bare interlayer coupling that does not couple well to spontaneous condensate, leads to extremely weak critical current that is also difficult to control by carrier imbalance, at least initially. However, for stronger coupling, the bare-coupling can cause nature of the condensate itself to change, and much of the behavior for couplings that do couple well to the condensate initially is regained. Since experimental efforts to observe this condensate state also may rely on enhanced interlayer current as a signature of the correlated state, the conclusions arrived at here may serve as important beacon to such efforts. The results I arrived at indicate the necessity to achieve a sufficient control over the interlayer single-particle processes in order to not only design devices based on the condensate control, but also experimentally observe this condensate state.

6.2 FUTURE WORK

Graphene remains a fascinating field of study with fresh discoveries and applications regularly [32], as well as significant technological progress to synthesize large-area graphene flakes on which these novel electronic devices can be built [88, 89]. As a continuation of the work presented here, the following areas of research seem interesting.

6.1.1 Rotated bilayer graphene

To date we have considered only aligned graphene bilayers. Rotated graphene is a rich field of study, particularly because such are observed frequently experimentally in grown graphene bilayers, for example, in epitaxial graphene on the C-terminated face of SiC [90]. A perturbative treatment of the bare interplanar tunneling within tight-binding theory [91] leads to a reduced velocity of the quasi-particles near the Dirac point of rotated graphene bilayer compared to conventional Bernal-stacked graphene bilayers. More recently, *ab initio* treatment of rotated graphene, as well as rigorous tight-binding treatment [92] also reaches the same conclusion, while also pointing out the possible localization of the electrons in bilayers with a small angle of rotation. Regarding formation of a condensate, if the two graphene monolayers are rotated, then the degree to which a condensate can form, the degree to which bare tunneling is able to couple to the condensate, and how it influences the long-range order that the exchange interaction tries to establish, remains to be found.

For modeling these rotated graphene bilayers within a tight-binding framework, we note that for rotation about the B_T-A_B carbon atom, which are stacked one on top of the other in a regular Bernal stacking, for a commensurate rotation, one gets periodic structures for the bilayer, of course, with bigger primitive cell, whose size increases with decreasing angle of rotation [91]. For such periodic structures, we can extend the treatment of exchange interaction as detailed here, at the cost of increasing computational complexity. This natural extension, even for relatively large angle commensurate rotation, such that the primitive cell is small, should indicate to possible fate of exchange interactions in a rotated graphene bilayer.

6.1.2 Spatially inhomogeneous bare tunneling

In a similar vein, instead of using a four-atom primitive cell for the regular graphene bilayer stacking (hexagonal or Bernal) considered here, using larger primitive cells, and different bare tunneling amplitudes between the vertically stacked carbon atoms, we can come up with a simple model of inhomogeneous bare tunneling across these graphene bilayers, which is very likely to occur when tunneling across an amorphous dielectric. While in this case the periodic treatment would imply an artificial repetition of the exact same spatial inhomogeneity in bare tunneling, one can possibly reduce this effect by increasing the size of the primitive cell under consideration.

6.1.3 Non-equilibrium transport

While we have investigated the maximum interlayer current that can flow between the two graphene layers in the condensate state, it remains a calculation based on equilibrium condensate properties. We can extend this to non-equilibrium calculation by using our variant of non-equilibrium Green's function detailed earlier. While our Green's function transport calculation employed a nearest-neighbor tight-binding Hamiltonian, the exchange potentials are non-local, and therefore, inclusion of such in the Hamiltonian necessitates re-formulation of the eigenfunction equation and the stabilization routines. In principle though, that remains possible. Alternatively, one may truncate the long-range interaction to a shorter range "effective" exchange interaction, and simulate a finite BiSFET device. We had earlier taken steps in this direction, by simulating single-particle transport for a device schematic shown in Fig. 4.1 assuming a delta function single-particle tunneling between the Bernal stacked carbon atoms in the two graphene layers within the coupled region, and uncoupled source-drain contacts from which we inject and extract carriers [87]. However, that was a first step to investigating the flow of current in the BiSFET geometry, and we can now improve the model by employing our knowledge of the self-consistent exchange potentials, to include a slightly longer range effective single particle hopping that mimics the Fock potentials.

References

[1] ITRS, "International Technology Roadmap for Semiconductors", 2009 Update.

[2] K. Natori, "Ballistic metal-oxide-semiconductor field effect transistor", *Journal of Applied Physics,* vol. 76, pp. 4879-4890, 1994.

[3] S. Datta *et al.*, "The silicon MOSFET from a transmission viewpoint", *Superlattices and Microstructures,* vol. 23, pp. 771-780, 1998.

[4] F. Assad *et al.*, "On the performance limits for Si MOSFETs: a theoretical study", *IEEE Transactions on Electron Devices, ,* vol. 47, pp. 232-240, 2000.

[5] R. Lake *et al.*, "Single and multiband modeling of quantum electron transport through layered semiconductor devices", *Journal of Applied Physics,* vol. 81, pp. 7845-7869, 1997.

[6] S. Datta, "Nanoscale device modeling: the Green's function method", *Superlattices and Microstructures,* vol. 28, pp. 253-278, 2000.

[7] A. Svizhenko *et al.*, "Two-dimensional quantum mechanical modeling of nanotransistors", *Journal of Applied Physics,* vol. 91, pp. 2343-2354, 2002.

[8] M. J. Gilbert and D. K. Ferry, "Efficient quantum three-dimensional modeling of fully depleted ballistic silicon-on-insulator metal-oxide-semiconductor field-effect-transistors", *Journal of Applied Physics* vol. 95, pp. 7954 - 7960, 2004

[9] L. F. Register, "Schrödinger Equation Monte Carlo: bridging the gap from quantum to classical transport", *International Journal of High Speed Electronics and Systems,* vol. 9, pp. 251-279, 1998.

[10] W. Chen, "Equation Monte Carlo simulation of nano-scaled semiconductor devices", Ph.D. dissertation, The University of Texas at Austin, 2004.

[11] K. M. Liu *et al.*, "Schrodinger equation Monte Carlo in three dimensions for simulation of carrier transport in three-dimensional nanoscale metal oxide semiconductor field-effect transistors", *Journal of Applied Physics,* vol. 104, 2008.

[12] K. S. Novoselov *et al.*, "Electric Field Effect in Atomically Thin Carbon Films", *Science,* vol. 306, pp. 666-669, 2004.

[13] A. K. Geim and K. S. Novoselov, "The rise of graphene", *Nat Mater,* vol. 6, pp. 183-191, 2007.

[14] S. K. Banerjee *et al.*, "Bilayer PseudoSpin Field-Effect Transistor (BiSFET): A Proposed New Logic Device", *Electron Device Letters, IEEE,* vol. 30, pp. 158-160, 2009.

[15] W. Chen *et al.*, "Simulation of quantum effects along the channel of ultrascaled Si-based MOSFETs", *IEEE Transactions on Electron Devices, ,* vol. 49, pp. 652-657, 2002.

[16] S. Datta, "III-V field-effect transistors for low power digital logic applications", *Microelectronic Engineering,* vol. 84, pp. 2133-2137, 2007.

[17] T. Ashley *et al.*, "Heterogeneous InSb quantum well transistors on silicon for ultra-high speed, low power logic applications", *Electronics Letters,* vol. 43, pp. 777-779, 2007.

[18] T. Ashley *et al.*, "Novel InSb-based quantum well transistors for ultra-high speed, low power logic applications", in *Proceedings of the 7th International Conference on Solid-State and Integrated Circuits Technology*, 2253-2256, 2004.

[19] S. Datta *et al.*, "85nm gate length enhancement and depletion mode InSb quantum well transistors for ultra high speed and very low power digital logic applications", *IEEE International Electron Devices Meeting 2005, Technical Digest,* pp. 783-786, 2005.

[20] T. Usuki *et al.*, "Numerical analysis of ballistic-electron transport in magnetic fields by using a quantum point contact and a quantum wire", *Physical Review B,* vol. 52, p. 8244, 1995.

[21] S. Datta, *Electronic Transport in Mesoscopic Systems*: Cambridge University Press, 1995.

[22] P. Vogl *et al.*, "A Semi-empirical tight-binding theory of the electronic structure of semiconductors+", *Journal of Physics and Chemistry of Solids,* vol. 44, pp. 365-378, 1983.

[23] G. Klimeck *et al.*, "sp^3s^* Tight-binding parameters for transport simulations in compound semiconductors", *Superlattices and Microstructures,* vol. 27, pp. 519-524, 2000.

[24] IMSL, Visual Numerics, Inc

[25] R. Akis *et al.*, "Self-consistent modeling of open quantum devices", in *Technical Proceedings of the International Conference on Computational Nanoscience and Nanotechnology*, 2002.

[26] T. Ando, "Quantum point contacts in magnetic fields", *Physical Review B,* vol. 44, pp. 8017-27, 1991.

[27] P. A. Khomyakov *et al.*, "Conductance calculations for quantum wires and interfaces: Mode matching and Green's functions", *Physical Review B,* vol. 72, 2005.

[28] C. Caroli *et al.*, "Direct calculation of the tunneling current", *Journal of Physics, C,* vol. 4, 1971.

[29] M. Luisier *et al.*, "Atomistic simulation of nanowires in the sp^3d s^* tight-binding formalism: From boundary conditions to strain calculations", *Physical Review B,* vol. 74, no. 205323, 2006.

[30] J. Robertson and B. Falabretti, "Band offsets of high K gate oxides on III-V semiconductors", *Journal of Applied Physics,* vol. 100, pp. 014111-8, 2006.

[31] F. Li *et al.*, "Physically based quantum-mechanical compact model of MOS devices substrate-injected tunneling current through ultrathin (EOT similar to 1 nm) SiO2 and high-k gate stacks", *IEEE Transactions on Electron Devices,* vol. 53, pp. 1096-1106, 2006.

[32] A. H. Castro Neto *et al.*, "The electronic properties of graphene", *Reviews of Modern Physics,* vol. 81, pp. 109-162, 2009.

[33] S. K. Banerjee *et al.*, "Graphene for CMOS and Beyond CMOS Applications", *Proceedings of the IEEE,* in press.

[34] M. C. Lemme *et al.*, "A Graphene Field-Effect Device", *Electron Device Letters, IEEE,* vol. 28, pp. 282-284, 2007.

[35] G. C. Liang *et al.*, "Performance projections for ballistic graphene nanoribbon field-effect transistors", *IEEE Transactions on Electron Devices,* vol. 54, pp. 677-682, 2007.

[36] G. Fiori and G. Iannaccone, "Simulation of graphene nanoribbon field-effect transistors", *IEEE Electron Device Letters,* vol. 28, pp. 760-762, 2007.

[37] G. Liang *et al.*, "Ballistic graphene nanoribbon metal-oxide-semiconductor field-effect transistors: A full real-space quantum transport simulation", *Journal of Applied Physics,* vol. 102, no. 054307, 2007.

[38] M. Han *et al.*, "Energy Band-Gap Engineering of Graphene Nanoribbons", *Physical Review Letters,* vol. 98, no. 206805, 2007.

[39] C. Berger *et al.*, "Electronic Confinement and Coherence in Patterned Epitaxial Graphene", *Science,* no. 1125925, 2006 .

[40] X. Li *et al.*, "Chemically Derived, Ultrasmooth Graphene Nanoribbon Semiconductors", *Science,* vol. 319, pp. 1229-1232, 2008.

[41] P. R. Wallace, "The Band Theory of Graphite", *Physical Review,* vol. 71, pp. 622-634, 1947.

[42] R. Saito *et al.*, *Physical Properties of Carbon Nanotubes*. London: Imperial College Press, 1998.

[43] K. Nakada *et al.*, "Edge state in graphene ribbons: Nanometer size effect and edge shape dependence", *Physical Review B,* vol. 54, pp. 17954-61, 1996.

[44] Y.-W. Son *et al.*, "Energy Gaps in Graphene Nanoribbons", *Physical Review Letters,* vol. 97, p. 216803, 2006.

[45] G. Lee and K. Cho, "Electronic structures of zigzag graphene nanoribbons with edge hydrogenation and oxidation", *Physical Review B,* vol. 79, 2009.

[46] I. L. Aleiner *et al.*, "Spontaneous symmetry breaking in graphene subjected to an in-plane magnetic field", *Physical Review B,* vol. 76, no. 195415, 2007.

[47] J. Kedzierski *et al.*, "Graphene-on-Insulator Transistors Made Using C on Ni Chemical-Vapor Deposition", *Electron Device Letters, IEEE,* vol. 30, pp. 745-747, 2009.

[48] M. I. Katsnelson *et al.*, "Chiral tunnelling and the Klein paradox in graphene", *Nature Physics,* vol. 2, pp. 620-625, 2006.

[49] D. Basu *et al.*, "Effect of edge roughness on electronic transport in graphene nanoribbon channel metal-oxide-semiconductor field-effect transistors", *Applied Physics Letters,* vol. 92, 2008.

[50] Y. Yoon and J. Guo, "Effect of edge roughness in graphene nanoribbon transistors", *Applied Physics Letters,* vol. 91, pp. 073103-3, 2007.

[51] E. McCann and V. I. Fal'ko, "Landau-Level Degeneracy and Quantum Hall Effect in a Graphite Bilayer", *Physical Review Letters,* vol. 96, no. 086805, 2006.

[52] T. Ohta *et al.*, "Controlling the Electronic Structure of Bilayer Graphene", *Science,* vol. 313, pp. 951-954, 2006.

[53] H. Min *et al.*, "Ab initio theory of gate induced gaps in graphene bilayers", *Physical Review B,* vol. 75, no. 155115, 2007.

[54] Y. Ouyang *et al.*, "Analysis of ballistic monolayer and bilayer graphene field-effect transistors", *Applied Physics Letters,* vol. 92, pp. 063120-3, 2008.

[55] C. H. Zhang and Y. N. Joglekar, "Excitonic condensation of massless fermions in graphene bilayers”, *Physical Review B,* vol. 77, no. 233405, 2008.

[56] H. Min *et al.*, "Room-temperature superfluidity in graphene bilayers”, *Physical Review B,* vol. 78, no. 121401, 2008.

[57] I. B. Spielman *et al.*, "Resonantly Enhanced Tunneling in a Double Layer Quantum Hall Ferromagnet”, *Physical Review Letters,* vol. 84, no. 5808, 2000.

[58] Graphene’s valley degeneracy is unfavorable for exciton condensation when interactions are weak, see for example M. Y. Kharitonov and K. B. Efetov, Phys. Rev. B 78, 241401, 2008; R. Bistritzer, H. Min, J. J. Su, and A. H. MacDonald, arXiv:0808.1310,unpublished; M. Y. Kharitonov and K. B. Efetov, arXiv:0903.4445,unpublished; This work does not attempt to achieve more definitive estimates of the phase diagram of strongly interaction electron-hole systems in graphene bilayers, and focuses instead on properties of the exciton condensate state.

[59] S. K. Banerjee *et al.*, "Bi-layer pseudo-Spin-Field-Effect Transistor”, Patent Application, 2009.

[60] D. Reddy *et al.,* "Bilayer Pseudospin Field-Effect Transistor: Applications to Boolean Logic”, *IEEE Transactions on Electron Devices, ,* vol. 57, pp. 755-764, 2010.

[61] E. E. Mendez *et al.,* "Quantum Hall Effect in a Two-Dimensional Electron-Hole Gas”, *Physical Review Letters,* vol. 55, pp. 2216-19, 1985.

[62] U. Sivan *et al.,* "Coupled electron-hole transport”, *Physical Review Letters,* vol. 68, pp. 1196-99, 1992.

[63] M. Pohlt *et al.,* "Closely spaced and separately contacted two-dimensional electron and hole gases by in situ focused-ion implantation”, *Applied Physics Letters,* vol. 80, pp. 2105-2107, 2002.

[64] J. A. Seamons *et al.,* "Undoped electron-hole bilayers in a AlGaAs double quantum well”, *Applied Physics Letters,* vol. 90, no. 052103, 2007.

[65] E. Tutuc *et al.,* "Counterflow Measurements in Strongly Correlated GaAs Hole Bilayers: Evidence for Electron-Hole Pairing”, *Physical Review Letters,* vol. 93, no. 036802, 2004.

[66] M. Kellogg *et al.,* "Vanishing Hall Resistance at High Magnetic Field in a Double-Layer Two-Dimensional Electron System”, *Physical Review Letters,* vol. 93, no. 036801, 2004.

[67] L. Tiemann *et al.,* "Critical tunneling currents in the regime of bilayer excitons”, *New Journal of Physics,* vol. 10, 2008.

[68] J. P. Eisenstein and A. H. MacDonald, "Bose-Einstein condensation of excitons in bilayer electron systems”, *Nature,* vol. 432, pp. 691-694, 2004.

[69] J.-J. Su and A. H. MacDonald, "How to make a bilayer exciton condensate flow”, *Nat Phys,* vol. 4, pp. 799-802, 2008.

[70] D. Reddy *et al.,* "Bilayer pseudoSpin field effect transistor (BiSFET): A proposed logic device and circuits”, in *Device Research Conference*, 2009, pp. 67-68.

[71] G. F. Giuliani and G. Vignale, *Quantum Theory of the Electron Liquid*: Cambridge University Press, 2005.

[72] E. H. Hwang *et al.,* "Many-body exchange-correlation effects in graphene", *Physica E: Low-dimensional Systems and Nanostructures,* vol. 40, pp. 1653-1655, 2008.

[73] T. Sugino *et al.,* "Synthesis of boron nitride film with low dielectric constant for its application to silicon ultralarge scale integrated semiconductors", *Diamond and Related Materials,* vol. 10, pp. 1375-1379, 2001.

[74] Several low-κ materials with ε_r lower than 3.9 are used in the semiconductor processing flow, e.g., Applied Materials uses C doping in SiO_2 to achieve εr in the range 2.5 to 3 in their CVD based Black Diamond® product.."

[75] J.-J. Su and A. H. MacDonald, "Critical tunneling currents in quantum Hall superfluids: Pseudospin-transfer torque theory", *Physical Review B,* vol. 81, no. 184523, 2010.

[76] C. R. Dean *et al.*, "Boron nitride substrates for high-quality graphene electronics", *arXiv:1005.4917v1,* vol. [cond-mat.mes-hall], 2010.

[77] D. Basu *et al.,* "Tight-binding study of electron-hole pair condensation in Graphene bilayers: gate control and system-parameter dependence", *Physical Review B,* in publication.

[78] J. F. Annett, *Superconductivity, Superfluids and Condensates*: Oxford University Press, 2004

[79] Y. Cui *et al.,* "High performance silicon nanowire field effect transistors", *Nano Letters,* vol. 3, pp. 149-152, 2003.

[80] J. Wang *et al.,* "A three-dimensional quantum simulation of silicon nanowire transistors with the effective-mass approximation", *Journal of Applied Physics,* vol. 96, pp. 2192-2203, 2004.

[81] J. Wang *et al.,* "Theoretical investigation of surface roughness scattering in silicon nanowire transistors", *Applied Physics Letters,* vol. 87, pp. 043101-3, 2005.

[82] R. Kotlyar *et al.,* "Assessment of room-temperature phonon-limited mobility in gated silicon nanowires", *Applied Physics Letters,* vol. 84, pp. 5270-5272, 2004.

[83] Sentaurus Process and Device, Synopsys, Inc, 2007.

[84] D. Basu *et al.,* "Using TCAD, Response Surface Model and Monte Carlo Methods to Model Processes and Reduce Device Variation", *2009 International Conference on Simulation of Semiconductor Processes and Devices,* pp. 253-256, 2009.

[85] E. X. Wang *et al.,* "Physics of hole transport in strained silicon MOSFET inversion layers", *IEEE Transactions on Electron Devices,* vol. 53, pp. 1840-1851, 2006.

[86] N. Neophytou *et al.,* "Bandstructure Effects in Silicon Nanowire Hole Transport", *IEEE Transactions on Nanotechnology,* vol. 7, pp. 710-719, 2008.

[87] D. Basu *et al.,* "Interlayer Tunneling Across Coupled Graphene Nanoribbons", in *TECHCON*, Austin, TX, 2009.

[88] G. Eda *et al.,* "Large-area ultrathin films of reduced graphene oxide as a transparent and flexible electronic material", *Nature Nanotechnology,* vol. 3, pp. 270-274, 2008.

[89] X. S. Li *et al.,* "Large-Area Synthesis of High-Quality and Uniform Graphene Films on Copper Foils", *Science,* vol. 324, pp. 1312-1314, 2009.

[90] J. Hass *et al.,* "Why multilayer graphene on 4H-SiC(000(1)over-bar) behaves like a single sheet of graphene", *Physical Review Letters,* vol. 100, pp. 1-3, 2008.

[91] J. M. B. Lopes dos Santos *et al.,* "Graphene Bilayer with a Twist: Electronic Structure", *Physical Review Letters,* vol. 99, p. 256802, 2007.

[92] *et al.,* "Localization of Dirac Electrons in Rotated Graphene Bilayers", *Nano Letters,* vol. 10, pp. 804-808, 2010.

Vita

Dipanjan Basu was born in Kolkata, India to Dolly and Manick Krishna Bose. After his initial schooling in Ramakrishna Mission Vidyalaya at Narendrapur, he entered Jadavpur University in Kolkata in 1997, wherefrom he earned Bachelor of Electronics and Telecommunication Engineering in 2001. Following a brief period of work as a technical consultant in IBM Global Services, India Pvt. Ltd., he joined Indian Institute of Technology, Kanpur in 2003 for his Master's in Electrical Engineering, with Microelectronics and VLSI as his major. Since 2005, he has been a graduate research assistant in the Microelectronics Research Center at the University of Texas at Austin, initially working with Dr. Sanjay K. Banerjee, and later more closely with Dr. Leonard F. Register. His interests are in modeling and simulation of semiconductor devices. Apart from his Ph.D. work on Green's function transport in semiconductor devices and electronic properties of bulk bilayer graphene, he has worked on compact MOSFET models for his Master's thesis, and modeled variations arising in process flow at Micron Technologies in Boise in summer of 2008. Following his Ph.D. degree, he wants to pursue device and process modeling at Intel Corporation at Hillsboro, Oregon.

Permanent address: 9A, Pranabananda Road, Garia, Kolkata 700084, India.
Email: dbasu.ut.2010@gmail.com
This dissertation was typed by the author.